Politecnico di Milano
Department of Physics
Doctoral Programme in Physics

# Integrated three dimensional photonic devices fabricated by femtosecond laser micromachining

Doctoral Dissertation of:
**Diogo Pereira Lopes**

Supervisor:
**Dr. Roberto Osellame**

Tutor:
**Prof. Roberta Ramponi**

The Chair of the Doctoral Programme:
**Prof. Paola Taroni**

2015 - 2018
XXXI Cycle

*Para a Lua e Vénus.*

# Contents

# Introduction

Light has played a major role in the shaping of life on earth, and on humankind itself. The first time we controlled fire, marked a change in our relationship to it as a tool, and a step in our path towards domination of nature and ourselves. Up to the last century its main use was dispersive, illuminating our nights and enabling us to outreach the suns hours and thus increasing productivity.

After the electronics explosion of the last century, light started as an output on all our screens that we still use today. But nowadays its creeping into being also an input. It all began with the invention of the laser, that enabled to have a light source with both high coherence, power and collimation. These three characteristics are all critical, and enabled the creation of whole new areas of investigation, such as spectroscopy and interferometry. Fiber technology was equally important since it enabled the "wiring" of these optical signals, in a perfect analogy with the electrical cables. Currently submarine optical cables bridge the communication over oceans to connect the different continents.

With the invention of ultra-short pulses, that compress all the energy into short bursts of high peak power, new phenomena were observed, such as higher harmonic generation and self-focusing, giving birth to non-linear optics, together with uncountable exploitations of these effects in other fields such as microscopy. When these beams are focused they can be used for modifying large band-gap materials that would normally be transparent, such as glasses and crystals. Multiphoton absorption can take place only at the focus and thus a new field was born: ultra-short-pulse direct writing. Now-a-days with this technique it is possible to write waveguides inside a wide range of materials in a truly 3D fashion, fact that is often exploited for realizing unique optical devices that would be hard to mimic in planar lightwave technology.

Out of all the materials, fused silica shows some unique properties. It is possible not only to directly write waveguides but also to create channels by selective etching of the laser modified region.

In this thesis work, you will find three different applications of the use of ultra-short pulses in fused silica:

Chapter 3 : In this chapter we will follow the trail towards the production of vertical waveguides by femtosecond direct writing and demonstrate their potential for being used in optical interconnection.

Chapter 4 : In this chapter we will focus on the use of the FLICE technique for the fabrication of Brewster angle polarisers embedded in glass, and explore the

possibility to take advantage of interferometric phenomena for improving the polarization ratio and reduce the overall size of the device.

Chapter 5 : In this chapter we will present a device for the distribution of gas for third harmonic generation of sub-femtosecond pulses in deep UV, that was realized by the FLICE technique.

In order to focus on the results and discussion only on the respective chapters, we added two more chapters. A background chapter (1) that starts with an introduction to the femtosecond direct writing field, and also has some basis on the physics necessary for the understanding of the main results of this thesis. Finally an experimental chapter (2) with a more detailed description of the setups and methods used for fabricating and characterizing the devices presented here.

# Chapter 1

# Background on femtosecond direct laser writing

This chapter aims both to provide the average reader with enough fundamental concepts necessary for the understanding of this thesis investigations, and also a contextual introduction to the field of fs-direct-laser-writing.

We will start by following the process of femtosecond direct writing from its generation, passing on the propagation, focusing, and the mechanisms that drive the modification at the focus.

Finally we have two more sections dedicated on the specific state of the art on the direct writing of waveguides (that will be useful for chapter 3) and etching of micro-channels (used in chapters 4 and 5).

## 1.1 Interaction of ultra-short laser pulses with Fused Silica

Ultra-short laser pulses with duration of ps and fs and with repetition rates from single pulse to tens of megahertz are now-a-days common, with many commercial solutions available. This opened up the possibility to explore their use in the microprocessing of materials. One particular interesting field is direct writing, in which these pulsed lasers are focused inside transparent materials in order to either create refractive index modifications or machine them. So lets delve a little into the physics of all the processes, from the generation and propagation of these ultra-short pulses up to their absorption and modification that they leave in the glass.

### 1.1.1 Basic glossary

In order to familiarize the reader with some terms that will be used throughout this thesis, let us make some quick definitions of important parameters for ultra-short pulses.

The pulse duration $\tau_p$ is generally defined at full-width-half-maximum (FWHM) of the intensity profile in time. It can though have different values depending on which fit you use. Most of the times the pulse shape can be well fit by a Gaussian or a square-secant.

These pulses in time can also be analysed in their wavelength spectra. For short pulses, there is a fundamental limit for the spectral width, that comes simply from the Fourier-transform. This limit is given by $\Delta\nu > \frac{a}{\tau_p}$, where $\nu$ is the bandwidth in frequency, and $a$ is a constant dependent on the shape of the pulse (0.315 for square-secant and 0.44 for Gaussian). Notice that if we convert this bandwidth to wavelength it will be wavelength dependent. If we suppose a 230 fs pulse duration at 1030 nm wavelength with Gaussian shape, we have a transform limit of 7 nm. In practice most lasers do not produce perfect pulse shape and thus may have higher band-width.

Another important attribute is the peak power, which is defined by $P_p = \frac{E_p}{\tau_p}$, where $E_p$ is the total energy of the pulse. In most applications we don't use only single pulses, but trains of these pulses that have a repetition rate $R = \frac{1}{\Delta t}$, with $\Delta t$ the temporal distance between pulses.

In order to compare results at different fabricating conditions in femtosecond laser micro-machining an important parameter we can use the Fluence, which is defined by:

$$F = \frac{E_p \cdot R}{\pi \cdot v \cdot \omega_0} \tag{1.1}$$

where $v$ is the scan velocity with which the beam is scanned and $\omega_0$ the beam spot size at the focus. This measure is particularly interesting since it gives the average energy that is deposited at each point in a scanned line, which in some cases is the defining variable that establishes the type of modification observed.

## 1.1.2 Generation

There are two main sources that are used for generating femtosecond laser pulses for micro-machining applications: Ti-sapphire stretched-cavity solid state lasers and Ytterbium amplified solid state and fibre lasers.

Ti-sapphire is typically based on passive mode-locking by Kerr lensing. A pulse duration of around 100 fs is normally achieved with tens of megahertz pulse rate and 1 W optical power. More recently there are commercial solutions that bring these pulses down to 10 fs with gigahertz frequencies by use of harmonic mode locking.

In the case of the Ytterbium fibre lasers, the gain medium is a doped fibre and the passive mode locking can be achieved by use of a saturable absorber at one of the ends of the cavity. Commercial solutions with 150 fs pulses and up to 200 $\mu J$ and repetition rates from single shot to tens of MHz are available.

Ti-sapphire lasers typically emit around 780 nm whereas Ytterbium sources work at 1030 nm. In some cases the second harmonic of Ytterbium based lasers is used at 515 nm to reduce the number of photons needed for the multi-photon absorption process.

Now-a-days most of these lasers are offered in commercial solutions with turn-key operation, and software control of many laser parameters, such as repetition rate or pulse duration. This evolution has increased the stability of the systems and allowed the same writing setup to explore different regimes of modification.

## 1.1.3 Propagation

After emission, in the most simplistic systems the beam is just steered by high reflectance mirrors into an objective lens that focuses the beam inside the sample to be modified. In most cases the beam needs also to pass through optical components, either for manipulating the beam width or externally control the power used. Let us do now some analysis on both linear and non-linear propagation of theses laser beams.

### Linear propagation

In most applications, the beam shape at the output of a laser follows closely a Gaussian beam. In order to achieve a high enough intensity to drive optical breakdown inside the glass, this beam needs to be focused. Typically a microscope objective is used to focus the beam inside the glass, so that chromatic and spherical aberrations are compensated for a given glass thickness. The beam waist at the focus depends only on the numerical aperture NA, vacuum wavelength $\lambda_0$ and the Gaussian coefficient M which is 1 for a purely Gaussian beam:

$$w_0 = \frac{M^2 \lambda_0}{\pi \text{NA}}, \tag{1.2}$$

Another important factor to take into account is the Rayleigh length, which indicates what is the length at which the beam diverges to $\omega = 2\dot{\omega}_0$:

$$z_R = \frac{n M^2 \lambda_0}{\pi \text{NA}^2}, \tag{1.3}$$

One first linear effect that a ultra-short pulse can suffer is dispersion. Since we have short temporal pulses they must have proportionally wider spectrum. This means that when propagating inside any material the relative phase acquired at each frequency will be different, which results in a chirping of the pulse, and consequently its broadening. In the case of Gaussian shaped pulses, and neglecting higher order effects, the pulse is broadened by [1]:

$$\Delta t_{out} = \sqrt{\Delta t_0^2 + \left( \frac{4 \cdot \phi'' \cdot l \cdot ln(2)}{\Delta t_0} \right)^2}, \tag{1.4}$$

in which $\Delta t_0$ is the pulse duration before propagating through $l$ length inside a material with $\phi''$ group delay dispersion (GDD). The GDD of fused silica is $19.0 fs^2/mm$ and of BK-7 (one of the most common glasses used in optics components) $25.1 fs^2/mm$ @ 1030 nm.

If we consider the propagation through 10 mm of glass of a pulse of 230 fs the pulse duration only changes by 0.03 fs. This effect gets critical though for sub 50 fs pulse durations (for which we have 1.9 fs broadening), arising the need to use curved mirror systems instead of lenses or to compensate by balancing positive and negative dispersive components on the beam path.

**Non-Linear propagation**

The fact that we have high peak powers, and particularly at the focal spot, means we need to take into account higher order effects on the refractive index to explain some of the phenomena observed. In order to take this into account we can make a power expansion of the relation between polarization and electrical field:

$$\mathbf{P} = \epsilon_0 \cdot (\chi^{(1)} \cdot \mathbf{E} + \chi^{(2)} \cdot \mathbf{EE} + \chi^{(3)} \cdot \mathbf{EEE} + \cdots), \tag{1.5}$$

Since fused silica is an amorphous glass, it presents inversion symmetry, which in our formulation translates to $\chi^{(2)} = 0$. Still we need to take into account the second order refractive index change:

$$n = n_0 + n_2 I = n_0 + \frac{3\chi^{(3)}}{4\epsilon_0 c n_0{}^2} I, \tag{1.6}$$

The coefficient $n_2$ is always very small in all materials, but the overall contribution increases with intensity $I = \mathbf{E}^2$, possibly dominating at extreme light intensities. In most materials this value is positive, and in the case of fused silica it is $n_2 = 3.5 \cdot 10^{-20} m^2/W$.

There are a few non-linear effects that arise with this addition. First, since we have a spatial Gaussian intensity distribution, and since this effect is intensity dependent, it means that the beam will suffer a different refractive index at each point, with a higher refractive index at the centre gradually decreasing to the periphery. In terms of optical path this is equivalent to propagating through a lens and so self-focusing of the beam takes place. Since diffraction still takes place, depending on the conditions one or the other will be prevalent. With some calculations it is possible to arrive at a critical power at which the beam shouldn't diverge that is given by [2]:

$$P_c = \frac{3.77\lambda^2}{8\pi n_0 n_2} \tag{1.7}$$

In the case of fused silica the critical power at 1030 nm is 3 MW. If we consider the peak power of a 230 fs pulse this corresponds to a limit of $0.7\mu J$ in pulse energy. At these kinds of powers we observe filamentation, and this has been exploited in the past for fast machining of transparent glass [3]. Its important to keep in mind that this does not take into account defocusing mechanisms that can happen at the focal spot such as plasma generation. Depending on the focusing conditions we can have different dynamics between these effects.

In the case of femtosecond laser micro-machining though we typically want to avoid self-focusing so we can have as small as possible modifications.

The other effect comes from the temporal shape of the pulse and is called self-phase modulation. Since we have a fast change in intensity due to the extremely short temporal pulse, we have a time dependent refractive index which results in the generation of new frequencies:

$$\omega(t) = \omega_0 - n_2 \frac{dI(t)}{dt} k_0 L \tag{1.8}$$

where $\omega_0$ and $k_0$ are the central angular frequency and wavenumber, respectively. The broadening of the spectrum does not by itself result in a change of the pulse duration, but due to material dispersion (as seen before) the pulse duration can be affected too. If the dispersion is normal/anomalous the pulse gets broadened/sharpened. This effect is actually exploited in the creation of ultra-short pulses, by first broadening the spectra, and then compressing it. In the case of extreme self-phase-modulation this can lead to a complete disruption of the pulse, generating multiple oscillations in the spectra with valleys between the peaks.

Let us consider 230 fs pulse duration with $1\mu J$ pulse energy, a beam width of 2.5 mm and propagation over 10 mm of fused silica glass. The accumulated wavelength shift is only 2 pm which is negligible in a 5 nm beam spectra (transform limit of the pulse). This means that these effects are negligible for the propagation through optics.

Now when the beam is focused, and particularly close to the focal point this effect gains importance. In figure 1.1 we have the accumulated wavelength shift when focusing inside fused silica. You can see that the wavelength shift is particularly critical closer to the focus when the beam width gets smaller than $10\mu m$.

**Spherical aberrations**

The objectives that are tailored for reducing both chromatic and spherical aberrations consider a specific glass thickness between the objective and the focal point. In fs laser micro-machining this thickness can vary significantly, as well as the material may not be exactly the glass that was considered for the aberration compensation. In all these cases, the index mismatch at the interface between

5
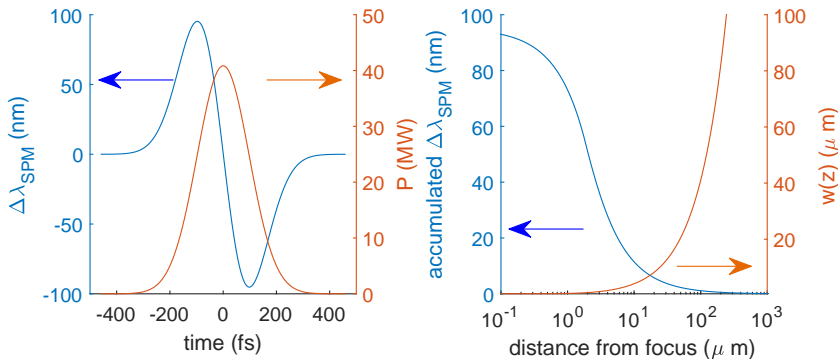
**Figure 1.1:** (left) Simulation of the accumulated Self-phase modulation of a beam that is focused inside fused silica with a 0.45 NA objective with 2.5 mm initial beam width, $1\mu J$ pulse energy and 230 fs pulse duration. It is possible to see the positive/negative chirp at the front/end of the pulse. (right) Accumulated wavelength shift and beam width as a function of the distance from the focus.

the objective working medium (air, water, oil) and the sample creates spherical aberration, consisting in the variation of the focus position with the incident angle.

Let us consider the scheme in figure 1.2. For lower angles the ray will converge to the paraxial focus $z_P$, whereas at higher angles the focus will shift up to the marginal $z_M$.
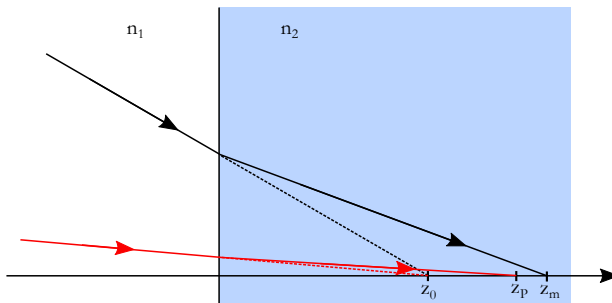


**Figure 1.2:** Scheme of the spherical aberrations that appear from the refraction at the sample surface.

The distance between these two points corresponds to the longitudinal spherical aberrations [4] :

$$\mathrm{SA}_l = z_m - z_p = z_0 \cdot \left( \sqrt{\frac{n_2{}^2 - \mathrm{NA}^2}{n_1{}^2 - \mathrm{NA}^2}} - \frac{n_2}{n_1} \right) \tag{1.9}$$

From this simple equation we can take a few interesting remarks:

- This aberration is depth dependent ($z_0$) , which means it is particularly important considering it in order to explore the 3D capabilities of the femtosecond laser direct writing technique. The elongation of the spot size due

6

to these aberrations leads to elliptically-shaped modifications, which can make it impossible for the modified region to hold a guided mode in the case of waveguides or quite simply reduce the precision at which structures are fabricated.

- Since $n_2 > n_1$ higher numerical apertures increase the aberrations. In the case of femtosecond direct writing we need to strike some balance between having a small enough spot size for triggering non-linear absorption (see equation 1.2) and reducing this effect. A good compromise that was found for a numerical aperture of around 0.5 in glasses shallower than $500\mu m$.

- Using a higher refractive index immersion medium such as water (1.33) or oil (1.4-1.5) can reduce these aberrations. In fact, if we compute for two depths of $500\mu m$ and $100\mu m$ these spherical aberrations using an objective with NA=0.5 in fused silica ($n_2 = 1.4500$ @1030 nm), we get with air immersion $12.2\mu m$ and $60.8\mu m$ whereas in water immersion we obtain $1.4\mu m$ and $6.9\mu m$, respectively. This means that both the aberration and its depth dependence are lower.

In order to tackle spherical aberrations there are many different approaches already tried.

The simplest (as discussed above) is to use a low numerical aperture [5], although this reduces the spatial resolution since the spot size gets larger.

Another approach is to use an objective lens with an adjustable ring that compensates for the required writing depth [6]. This compensation means however that only one depth will have an optimal focal spot, and so can't be used for writing 3D structures.

A more complex method is to use a spatial light modulator (SLM) [7][8][9], which can be used to manipulate the phase distribution and achieve a compensated modification. With this method it could be theoretically possible to do dynamic compensation while writing at different depths although the fast switching between phase masks on the SLM is not trivial.

### 1.1.4 Non-linear absorption

Since we are considering a large band-gap material, linear absorption at the working wavelengths (500-1100 nm) is quite low. In the case of fused silica as can be seen in figure 1.3 the absorption spectrum only starts increasing in deep infra-red ($> 2\mu m$) and UV ($< 300nm$) wavelengths. Fused silica band-gap is 9 eV [10].

Since we focus a temporally short pulse, also concentrating it spatially, we can achieve very high peak intensities of up to $10^{17}W/m^2$. At this concentration of photons, less probable quantum processes can occur with enough scale to dominate in the generation of free electrons in the material.

In figure 1.4 we can see the main non-linear processes that bridge these linearly prohibited energy gaps. For the beginning of the process there are two main mechanisms: multi-photon absorption and tunnelling absorption.

In the case of multi-photon absorption, multiple photons are absorbed at the same time so that their total energy $mh\nu > E_g$.
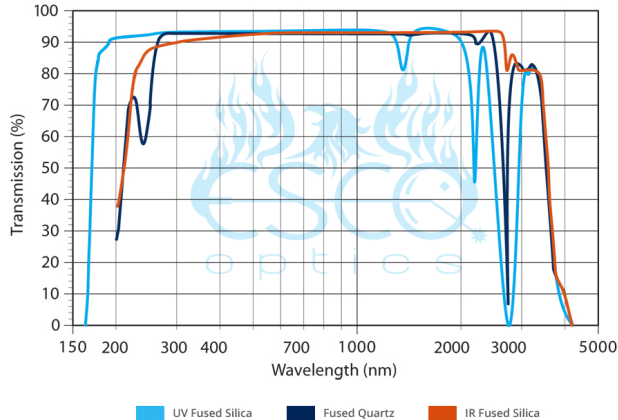
**Figure 1.3:** Fused silica absorption spectra. (from ESCO website)

In the case of tunnelling absorption the electron bands themselves are distorted, and with the reduction of the potential barrier band-to-band direct tunnelling is allowed.

Once a critical density of electrons are excited to the conduction band by one of these two mechanisms, avalanche ionization can take place. Here the electrons in the conduction band are first excited by absorbing multiple photons, until they reach enough energy such that impact ionization can occur, with the electron in the conduction band transferring its kinetic energy to excite another electron from the valence band, resulting in a pair of electrons in the conduction band. This process will then repeat again at double the rate. The exponential nature of avalanche ionization takes over after enough electrons are excited to the conduction band by either of the first two methods or are already existent due to defects and impurities.

A general theory for non-linear photo-ionization was proposed by Keldysh [11], which is used even today and shows good agreement with experimental data of multi-photon absorption coefficient. More recently [12] an improvement was made that also obeys the selection rules from perturbation theory, which further improves the agreement with experimental data. In both cases the Keldysh parameter can be used for knowing which of the two initial processes dominates:

$$\gamma = \frac{\omega}{e}\sqrt{\frac{m_e c n \epsilon_0 E_g}{I}} \tag{1.10}$$

where $\omega$ is the light frequency, $e, m_e$ the electron charge and mass, $E_g$ the band gap (which is 9 eV for fused silica) and $I$ the light intensity. If $\gamma >> 1.5$ then multi-photon ionization dominates, whereas at higher laser intensities $\gamma << 1.5$, and tunnelling ionization dominates. Considering a 1 $\mu J$ pulse energy focused with a 0.5 NA objective in fused silica we have a Keldysh parameter of 0.32, which means that the dominant mechanism is tunnelling absorption.

8
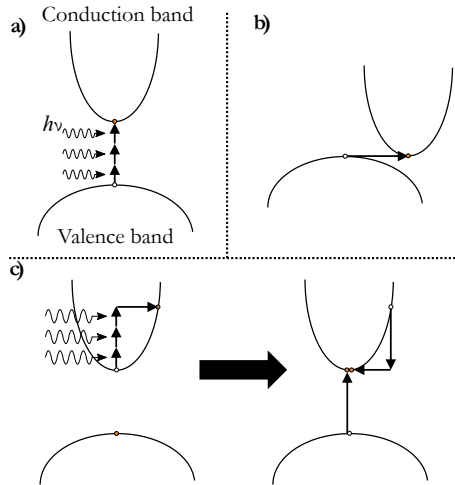
**Figure 1.4:** Scheme of the main energy absorption mechanisms that take place at high energy and that bridge the large-bandgap materials: a) multi-photon absorption, b) Tunnelling ionization, c) avalanche absorption

## 1.1.5 Relaxation and modification

With the increase of free carriers induced by the non-linear absorption process, the plasma frequency also increases, until it matches the laser light frequency $\nu$, when light absorption is almost complete. After this all the energy that was absorbed is passed to the substrate lattice in form of heat, during plasma relaxation, and this leads to the final structural modification.

There are three main types of modification that can be identified, that depend on several exposure parameters (pulse energy and duration, repetition rate, wavelength, beam polarization, numerical aperture and scan speed). In the particular case of fused silica we can achieve each of them by only changing the pulse energy and duration [13]

### Low fluence - Refractive index

At low pulse energies (ex: $0.1\mu J$ for 0.6 NA objective, 800 nm wavelength and 100 fs pulse duration), a smooth and isotropic refractive index change is induced. The main mechanism for Fused silica is material densification caused by rapid quenching of the melted glass in the laser focal volume [14]. Although it was also proved that colour centres have a role [15], it was shown that we still observe waveguiding even when annealing to temperatures high enough to erase them [16].

### Nano-grating formation

At an intermediary pulse energy (ex: 150–500 nJ for 0.6-NA focusing of 800-nm, 100-fs) the formation of nanogratings takes place. These are sub-wavelength

patterns that have been found to follow a periodicity of $\Lambda \simeq \frac{\lambda}{2n}$ where n is the refractive index of the material.

These gratings are oriented perpendicularly to the writing laser electric field polarization. The reason for their orientation is attributed to an interference effect of the incident lasers field with the induced electron plasma wave [17] [18].

It was also observed that the formation of this structures is a cumulative process related to the interaction of the modification left by previous pulses with the subsequent ones[19] [20]. In a first stage the modification creates irregular and randomly distributed hot spots that can arise from multi-photon ionization due to defects or colour centres. In a second stage each of these spots starts to grow and form isolated domains, forming a periodic localized structure. In a third stage all of the domains start to merge together leaving an extended nano-grating with an uniform periodicity. In figure 1.5 you can see both the orientation and build-up phenomenons clearly.
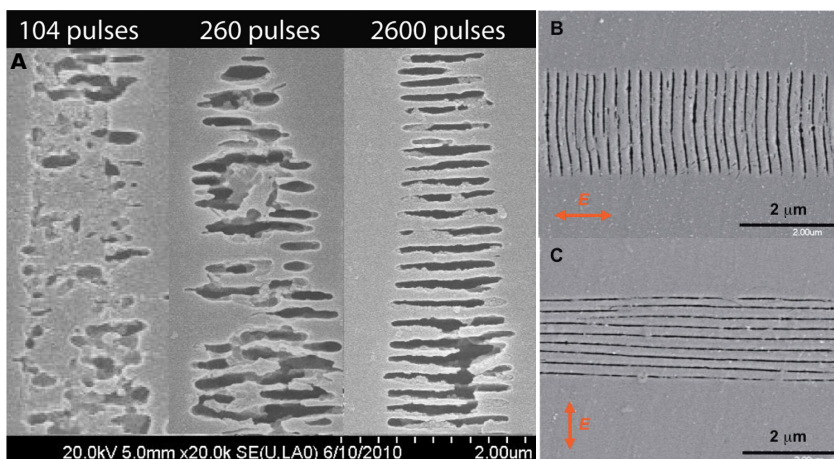


**Figure 1.5:** Panel A: With an increasing number of contributing laser pulses the modifications undergo three distinct stages: Initially randomly distributed structures (I) evolve into ordered domains (II), and finally merge to extended gratings with uniform periodicity (III) [19]. Panel B/C: SEM images of self-organized periodic nanoplanes where E is parallel with the scanning direction (B) and perpendicular (C). Nominal separation of the grating planes is 250nm.[20]

**Voids**

With the increase of pulse energy, the size of the generated plasma also increases. At sufficiently high peak intensities ($> 10^{14} W/cm^2$) the electron density can increase dramatically, and when the energy is transferred to the lattice it results in a shock wave that creates voids as small as 200 nm [21]. The use of short pulses here is crucial: with longer pulse duration (200 ps) cracking damage appeared at the threshold pulse energy and the voids were also wider [24].

These voids were proved in several different transparent materials, such as fused silica, and sapphire [22].

It was also observed that these voids have some flexibility for manipulation.

It was shown that they can be moved and even merged together [23]. Using a higher numerical aperture (NA=0.9) it was possible also to create with a single pulse a line void, due to self-focusing effects. The subsequent exposure to more pulses leads to the appearance of void arrays that can be tens of microns long [25] [26].

More recently a similar bubble formation was observed also at 10 MHz repetition rate in silica and borosilicate glasses. Here the nature of the interaction is different: due to the high repetition rate heat accumulation takes place with the accumulation of energy with the train of pulses. After reaching a critical temperature, bubble nucleation takes place. This bubble ends up distorting the beam focus, switching off the build up of modification. By scanning at fast speeds (10-30 mm/s) it was possible to create a chain of these bubbles with fixed periodicity [27].

## 1.2  fs-direct-writing of waveguides

In this section we will focus on the fs direct writing of waveguides. We will start by analysing the physics of waveguiding, passing to different methods to fabricate waveguides, and focusing afterwards on fs direct writing by analysing the fabrication configurations and optimal writing conditions.

### 1.2.1  Fundamentals of waveguiding
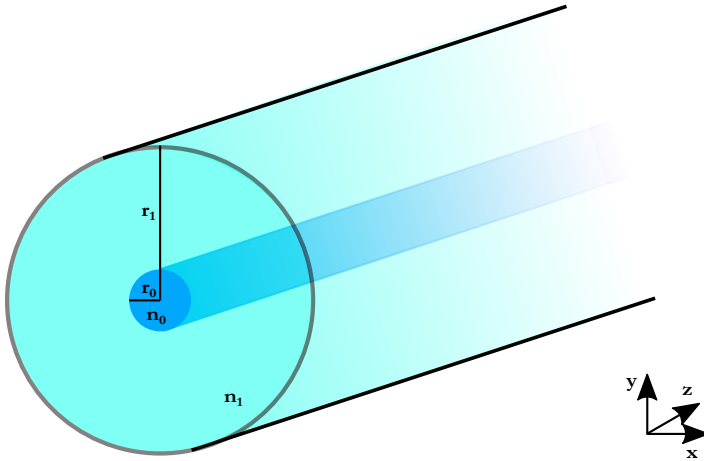


**Figure 1.6:** Scheme of a step index fiber.

Some basic concepts taken from waveguiding theory are useful for this thesis. In its most fundamental form, a waveguide is any structure that is able to confine the propagation of light in it. In the scope of this thesis we deal with dielectric waveguides (see figure 1.6) with $n_0 > n_1$, more particularly in the weakly guiding regime:

$$\frac{n_0 - n_1}{n_0} \ll 1 \tag{1.11}$$

Let us consider a cylindrical waveguide with a step index profile. In reality most waveguides do not have pure step index profile, but this analysis is useful to highlight some basic concepts in waveguiding theory.

Normally we have $r_1 \gg r_0$ and we can assume an infinite cladding. In this case we can reduce the Maxwell equations to the Helmholtz equation in cylindrical coordinates $(\rho, \theta, \phi)$:

$$\frac{\partial^2 U}{\partial \rho^2} + \frac{\partial U}{\rho \partial \rho} + \frac{\partial^2 U}{\rho^2 \partial \phi^2} + \frac{\partial^2 U}{\partial z^2} + n\left(\rho\right)^2 k_0{}^2 U = 0 \tag{1.12}$$

where $U\left(\rho, \phi, z\right)$ is either the electric field magnitude. We want to find guided wave solutions that propagate in the z direction:

$$U\left(\rho, \phi, z\right) = \Omega\left(\rho, \phi\right) e^{-jk_z z} \tag{1.13}$$

in which $k_z$ is the propagation constant. Now if we consider only realistic solutions in which the field doesn't diverge when $\rho \to \infty$ or $\rho \to 0$, we find that the solutions for $\Omega(\rho, \phi)$ are simply the Bessel functions of the first kind $J_l(u)$ at the core ($\rho < r_0$) and of the second kind $K_l(u)$ in the cladding ($\rho > r_0$). $u = k_{t0}\rho = \rho\sqrt{n_0^2 k_0^2 - k_z^2}$ and $w = k_{t1}\rho = \rho\sqrt{k_z^2 - n_1^2 k_0^2}$ are dimensionless parameters.

The mode propagated will have $n_1 < \frac{k_z}{k_0} < n_0$, and we call $n_{eff} = \frac{k_z}{k_0}$ the effective refractive index. The guided mode behaves as if it is propagating in a medium with the effective refractive index, which will be closer to the core index as the percentage of the power propagating inside the core increases.

Finally there are two important constants: the normalized propagation constant $b = \frac{n_{eff}^2 - n_0^2}{n_1^2 - n_0^2}$ and the normalized frequency $\nu = r_0 k_0 \sqrt{n_0^2 - n_1^2}$.

If we apply the boundary condition of the continuity of the tangential components of the $\vec{E}, \vec{H}$ fields, which translates in $u(\rho)$ and its derivative having continuity at $\rho = r_0$, arriving at the following relationship:

$$\frac{u J_{l+1}(u)}{J_l(u)} = \frac{w K_{l+1}(w)}{K_l(w)} \tag{1.14}$$

for $l = 1, 2, \ldots$, where l is the circumferential order. Since the Jacobian function is oscillatory, for each l we can have multiple solutions, which we number $p = 1, 2, \ldots$. These two numbers define the linear polarized mode $LP_{m,l}$ that corresponds to each solution.

Using equation 1.14 we can find the possible $u, w$ values and consequently compute the dispersion relation shown in figure 1.7. From this graph we find for a given normalized frequency $\nu$ only a finite number of modes can propagate inside this waveguide. This parameter is mostly fixed by the waveguide structure (radius, refractive indexes), with the only free variable being the wavelength. Each of the b values corresponds to a different effective refractive index. So each of the modes will propagate with different velocity and bending losses. We call cut-off wavelength of a mode the maximum wavelength that can be propagated in a waveguide, corresponding to the $\nu_c$ at which $b = 0$. Although its seems so in the graph there is no theoretical cut-off wavelength for the fundamental mode $LP_{01}$ (in more complex fibre designs (e.g. photonic crystal fibres) its possible to have a cut-off wavelength also for the fundamental mode). We have single mode operation at wavelengths above the $LP_{11}$ cut-off wavelength which corresponds to $\nu < 2.405$.

The normalized frequency encompasses many important dependencies. For example, if a waveguide shows single mode behaviour at a given wavelength, its expected it will start being multi-mode at some shorter wavelength. The same can happen if we increase either the core radius, or the refractive index change $n_0 - n_1$.

On the other hand, as we approach the cut-off wavelength and the propagation constant $b$ decreases, the mode is less and less confined, with its energy increasingly propagating on the cladding. This means that the mode will be more sensible both to bending losses and other non-uniformities that translate into higher propagation losses. So the same mode propagating in a waveguide
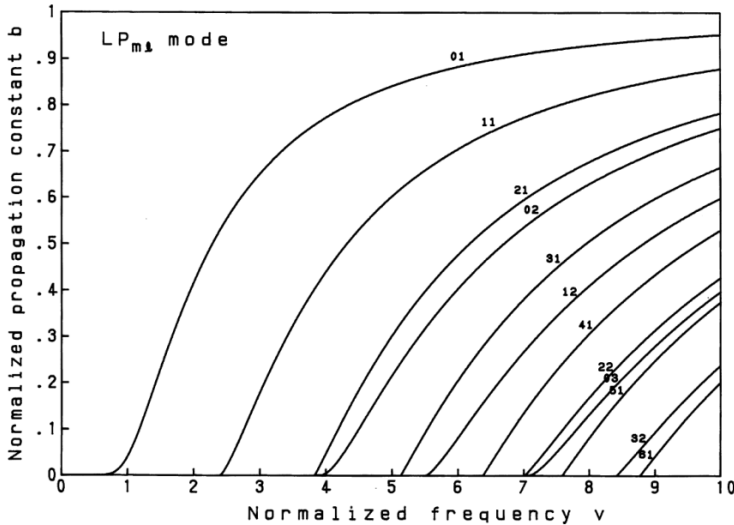
**Figure 1.7:** Graph of the linear polarized (LP) modes of a step index fiber in terms of their normalized propagation (b) and frequency ($\nu$) constants

will tend to have more losses at higher wavelengths (not taking into account other wavelength dependent sources of loss such as material impurities/absorption).

One last comment is that the mode $LP_{ml}$ actually corresponds to two linearly polarized modes in the two orthogonal directions. They share the same propagation constant and thus same $n_{eff}$, due to the symmetry of the problem. If we change the geometry or refractive index distribution to an asymmetric one, the two modes would split from those curves and we would get birefringence $B = n_{eff,1} - n_{eff,2}$.

### 1.2.2 Fabrication techniques

There are many techniques to fabricate waveguiding circuits, that depend on the substrate and specific application in which they are used. The dominating method follows standard lithographic techniques.

**Planar light-wave circuit technology**

PLC waveguide fabrication can be summarized as follows. First we create a bi-dimensional layer of high index material on top of a substrate of lower index, and then either by applying UV or electron beam lithography we can create gaps in the plane and thus define the waveguides.

In the case of glasses or amorphous polymers the layer creation can be done by depositing a thin layer either by sputtering or evaporation [28] [29] [30] [31]. For crystalline substrates we can use either annealing in a controlled atmosphere or solution, or use a static electric field [32] in order to change the material by ion diffusion, exchange or migration [33] [34] [35]. Alternatively, we can also

implant the ions directly by using an ion beam [36]. In the case of semiconductors the common method involves epitaxial growth methods such as molecular beam epitaxy [37] or chemical vapour deposition [38] [39].

These kind of techniques allow the fabrication of very low propagation loss waveguides (1-5 dB/m). Out of all the different types of waveguides lately silicon nitride ($Si_3N_4$) and silica ($SiO_2$) fabricated on top of silicon wafer are proving particularly promising [40] [41]. Apart from the high-level performance, they also have the natural advantage of easier industrial adaptation from importing technology from the semiconductor industry, and are set to be the future in terms of optical communications.

Overall this approach proves particularly useful in high-throughput applications, since the fabrication can be easily parallelized by producing a huge number of devices while using the same mask. On the other hand the main limitation rises in the planar nature of this technique, which means that devices are limited to work in the same plane. Also fabrication of a small number of devices is often too costly due to the fixed costs of the mask, and the facilities themselves, which are clean rooms with high running and equipment costs. Finally the last limitation is the lack of flexibility in the choice materials used, since in clean rooms there are risks of cross-contamination that can ruin the devices.

**fs-waveguide-direct-writing**

Femtosecond laser direct writing works as a somewhat complementary method to PLC technology. It is a much cheaper alternative (the costlier elements are the fs laser and precision translational stages) that does not require special facilities: only temperature and humidity control that can be achieved by commercial air-conditioning solutions. The fabrication is done in a single step without the need of any mask, and so the time between trials can be as fast as preparing the new fabrication code, which proves very useful for rapid prototyping.

The fact that it provides solutions in the 3D volume means that it can differentiate and thus find its niche applications for which no other technique can mimic.

Finally, the number of materials that can be fabricated with the same writing setup can be quite varied. In theory any transparent material can be used with this technique. For now it has proven its efficacy with glasses such as fused silica [42], borosilicate [43], phosphate [44] and chalcogenide [45]; crystals such as lithium niobate [46] and silicon [47], but also polymers such as PMMA and hydrogel [48].

## 1.2.3 Fabrication configuration

There are two main configurations possible for the fabrication of fs direct written waveguides:

**Transversal**

In the transversal configuration the laser focus is scanned perpendicularly to the beam propagation direction. This is the most commonly used configuration,

since if all the waveguides written are at similar depth, aberration effects will not change and thus we have a uniform profile across the waveguide.

The effective writing focal spot-size is typically elliptically shaped, and in some cases non-linear effects such as self-focusing can lead to further increase of the elongation. This leads to intrinsic birefringence (analogous to what is discussed in section 1.2.1), and possibly to an elliptical mode which is undesirable for output coupling into a fibre. In order to get a symmetric modification, beam shaping techniques can be used to get a round focal spot [49] [50]. Another possibility is using multiple scans laterally shifted so they together form a more symmetric shape of index modification [51] [52]. The birefringence can although be exploited and even enhanced through written stress tracks for polarization manipulation devices [53].

**Longitudinal**

In the longitudinal scheme, the writing direction is the same as the writing beam propagation direction. This means that the waveguide length is limited by the working distance of the writing objective.

Furthermore there is tapering of the waveguide due to changing spherical aberrations with depth. As seen in section 1.1.3 there are many methods for tackling spherical aberrations. But most of them cannot be easily adapted in real time for the changing spherical aberrations in depth when writing longitudinal waveguides.

A single-mode vertical waveguide at red wavelength was achieved in borosilicate glass by using an SLM and a self-correcting feedback algorithm to find the appropriate phase mask at each depth, and change it throughout the writing process [54]. Again using an SLM, X. Long et al [55] fabricated type II waveguides in phosphate glass by creating a hollow beam that would write in a single scan a tubular region of depressed cladding. The resulting waveguide could hold a single mode at 780 nm, although no loss characterization was provided.

To the best of my knowledge no low-loss vertical waveguides able to guide a single mode at 1550 nm wavelength were reported in literature at the moment of writing this thesis.

## 1.2.4 Optimal writing conditions

The different writing conditions, both regarding the laser parameters (repetition rate, wavelength, pulse duration) and the focusing optics, need to be tuned in order to provide the wanted refractive index change profile. Here we analyse the main results found from the previous investigations on all these influences:

**Repetition rate**

Across all the writing parameters that can be changed in direct laser writing, the repetition rate plays a crucial role in the dynamics of absorption. When working in the low repetition rate regime (<100 kHz), the modification is defined by the interaction of a single pulse, which typically results in a very asymmetric modification cross section. The thermal shock of a quick change in local temperatures

can lead to higher propagation losses due to non-uniformities and increased birefringent stress. Finally lower repetition rates require also lower scanning speeds, in the order of tens of $\mu m/s$, leading to longer fabrication times.

If the time separation between pulses is shorter than the heat diffusion time out of the focal volume (typically around $1\mu s$), the local temperature rises and if we get enough accumulation this can lead to further modification of the material. In borosilicate glass repetition rates above 200 kHz were enough to trigger these effects [56]. This is the ideal regime for boro/alumino silicate glasses. In fused silica this effect is less dominant than with other glasses, but still there is evidence of heat accumulation in the refractive index change, particularly in the 1-10 MHz range [57].

When working with very high repetition rates, the pulse energy needs to be low (tens of nJ) and so tight focusing is required. This limits the depth at which structures can be written. On the other hand speed can be increased up to cm/s range, and the modification is more isotropic.

A good compromise is found at the 0.5-2 MHz range [58], with the possibility to process a wide range of materials, and with an average numerical aperture of the focusing objective in the range 0.25-0.5, that allows processing up to millimetres in depth.

**Other Parameters**

All the other writing parameters end up having a big effect on the waveguide quality. The numerical aperture can change the modification pattern since it changes the size of the focal volume. If we divide equations 1.2 by 1.3 we get the following relation:

$$\frac{\omega_0}{z_R} = \frac{NA}{n} \tag{1.15}$$

Ideally in order to have a round modification we would need an NA=n; which would be 1.444 in the case of fused silica. This kind of numerical aperture is not easily achieved without oil immersion, and would only allow working at very shallow depths. Furthermore spherical aberrations increase with NA so this would also be another issue with higher numerical aperture.

The non-linear refractive index $n_2$ of the material also limits the processing window in terms of pulse energy and fabrication depth due to self-focusing, which can lead to filamentation, particularly in materials such as chalcogenide, polymers and metal oxides.

The wavelength of the writing laser is also important, since it defines how many photons are necessary for the non-linear absorption process. Particularly in the case of fused silica the exploration of the second harmonic (522 nm) of Ytterbium lasers proved useful in reducing waveguide non-uniformity and consequently achieving low insertion losses. [59] [60].

Some studies also looked into pulse duration effects on the quality of waveguides. Depending on the writing system this is not always a trivial parameter

to control during fabrication. The general trend is that shorter pulse durations also provide lower losses [61] down to 150 fs. We should not forget that, as seen before, first and second order dispersion effects get critical at pulse durations below 50 fs, and so the need of dispersion compensation schemes arises at such pulse durations[62], rendering the writing systems more complex. Even with these compensations the self-phase modulation effects inside the glass for such short pulses cannot be disregarded, and could disrupt the pulse before it reaches the critical size for modification.

**Applications**

The lowest propagation losses found in direct written waveguides in fused silica are 0.1 dB/cm [61], which is comparable with the best results achieved with PLC technology waveguides. The mode in this case is quite elliptical, which increases coupling losses from standard single mode fibres.

It is though possible to have a mode size compatible with commercial fibres at 1550 nm wavelength ($\approx 10.4\mu m$) while keeping a reasonable (0.8 dB/cm) propagation loss [59]. You can see such mode in figure 1.8.

A somewhat hybrid solution is offered in [63] where fabrication conditions are changed in three phases: the first one has a rounder mode for accommodating the fibre one and reduce coupling losses, and then a second transition region that progressively reshapes the mode for the third phase where they have low propagation loss fabrication conditions.
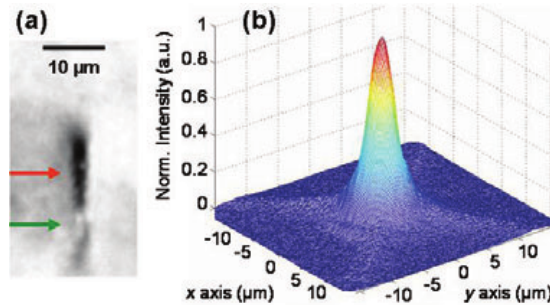


**Figure 1.8:** Panel A: Cross-section picture of the modification observed in fused silica. Two regions are highlighted: the red arrow points to the darker region that has a negative refractive index modification, whereas the green arrow points to the small white region where we have a positive refractive index change and can support waveguiding. b) The output single mode observed at the end of the waveguide [59].

With femtosecond direct written waveguides, many unique devices have been created: 1xN beam splitters [64], Mach-Zehnder interferometers [65], directional couplers for beam splitting [66] and demultiplexers [67]. Many of them take great advantage of the unique capabilities of this writing technique.

## 1.3 Microchannel etching

After irradiation by femtosecond laser in fused silica, it was discovered that the modified area is selectively etched when exposed to a strong acid such as HF [68]. This discovery led to the establishment of a technique called FLICE (Femtosecond Laser Irradiation followed by Chemical Etching), which permits in a simple two-step process to etch 3D channels inside glass substrates. A similar method, only with an additional step of thermal treatment has been also explored in Foturan glass [69].

The increase in etching rate was found to be linearly dependent with the induced refractive index change [70]. One of the reasons pointed for this phenomenological change is related to the densification mechanism, that traduces itself in a reordering of the silica ring structures, and a decrease in the bridging bond angle, which can lead to an increase of the reactivity with the attacking acid.

As seen before at higher fluence we have the formation of nano-gratings. These nano-gratings work as access channels for the etchant to flow, dramatically increasing the etching rate. As can be seen in the example provided in figure 1.9 when the polarization is perpendicular to the laser direction (and thus the nano-gratings are oriented in the channel direction) the etching rate is two orders of magnitude faster.

Another interesting dynamic is the big jump from pulse energies below 100 nJ to above 200 nJ, which corresponds to the formation of nano-gratings. It is also reported that after a certain threshold of pulse energy a drop in the etching rate can be observed, which is where we also start observing a disruption of the nano-grating pattern out of optimum conditions [71].

This difference in etching rate depending on polarization can be used for controlling the velocity at which each section is etched. This enables the exploration of interesting strategies for etching more complex and asymmetric structures [72]. If the desired structure needs a constant etching rate in both directions, we can use circular polarization, that does not show a preferential etching direction, but etches with lower rate [71].

Something that needs to be taken into account is that the etching does not only attack the irradiated material, but also the unmodified glass. This leads, in the case of etching of a single irradiated line, to a conical shape, since the beginning of the channel continues to be etched while the etchant is still propagating until the end of the line, enlarging it. The angle of this cone will correspond to the ratio of the two etching ratios $\alpha = atan\left(\frac{v_{unmod}}{v_{mod}}\right) = atan(\frac{1}{R})$, where R is the aspect ratio defined as the length of the micro-channel divided by the radius of its entrance cross section.

The etching reaction with HF acid is the following: $SiO_2 + 4HF = SiF_4 + 2H_2O$. The reaction is not regenerative and thus after a limited amount of time the solution is degraded. Particularly inside the channel the solution reaches a local equilibrium, and thus in order to continue the etching it needs to be renovated. A common approach for helping this is using an ultrasonic bath. Still there is a limited length that can be achieved with this technique for a single channel, and a common solution is to create auxiliary access holes separated at
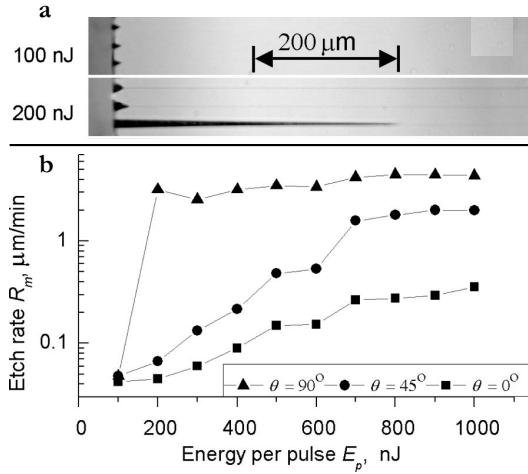
**Figure 1.9:** Analysis of lines direct written with different polarizations (top:parallel; middle: $45°$ and bottom: perpendicular with respect to the written line direction) and also different pulse energies. a) Microscope images of the waveguides written with 100 and 200 nJ after 2h etching. b) graph with the etching rate observed for all the waveguides. [14]

constant distance so the acid can flow inside the channel, and also reduce the total device etching time.

In order to tune the etching process, both the temperature and concentration of the etchant can be changed. High concentrations in the acid solution allow longer micro-channels but worse aspect ratio (higher $\alpha$) [73]. The current limit is around 1.8 mm with $90\mu m$ base width. Considering that this length can be etched in only 3 hours inside a 20% HF solution [74], and that if we etch from both sides we can double this value, this proves quite an useful solution for microfluidic applications.

If the desired channel is large enough, a typical approach to compensate the conical shape of the etched channels is to irradiate a reverse cone, ending with the wanted final width, so we get a straight channel [75].

An alternative to HF is to use a highly concentrated solution of KOH [76]. This solution allows much longer channels (up to 1 cm) with 200 aspect ratio. The main limitation is the overall etching rate, which is 5 times smaller when compared with the previous example.

An important property depending on the application is the roughness of the etched surfaces. An overall roughness of hundreds of nanometres was found on the surface of etched channels [77]. One method of reducing this roughness is through thermal treatments, either by annealing in an oven [78] or using an OH flame [79]. With these methods the roughness can be reduced of one order of magnitude or more. The main drawback of these methods is that they can damage the external glass surface, which can render the device unusable for some applications. In the case of devices that combine channels with direct written waveguides the later are affected by the treatment and therefore cannot be written before the surface smoothing process.

Ho et al. made an interesting study in which they wrote multiple vertical scans, separating them by a fixed distance to create a layer of parallel scans. Then they optimized the separation between lines, pulse energy and polarization [80]. The lowest roughness was observed for the pulse energy closest to the threshold for nano-grating formation. This hints that one of the sources of the surface roughness is defects in the parallel nano-gratings or stress accumulation that is expected to increase with the pulse energy. The lowest roughness also corresponds to the perpendicular polarization, going together with the faster etching. For the best conditions an overall roughness of 10 nm was observed at the side-walls, whereas at the bottom we have again the hundreds of nanometres roughness.

**Applications**

Currently, the FLICE technique is a well established solution, with many unique applications found in different areas from optics to microbiology. Some examples are the fabrication of micro-lenses [81] [79] and microchips able to do capillary electrophoresis of DNA fragments for cancer detection [59].

The unique possibility to fabricate together directly written waveguides and micro-channels also found many applications [74], with some examples being a Mach-Zehnder interferometer for refractive index measurement [65] and cell sorting with the use of waveguides for laser trapping inside the channel [82].

# Chapter 2

# Experimental setup and methods

In this chapter we will give the details aspects of the experimental setups used in this thesis. Both the fabrication setups and the diverse characterization setups will be described and analysed so that the results obtained in the other chapters can be fully understood.

| Lasers | | Amplitude Satsuma HP | High Q FemtoREGEN | Amplitude Satsuma $HP^2$ |
|---|---|---|---|---|
| Emission wavelength | $\lambda_0\,(nm)$ | 1030 | 1040 | 1030/515 |
| pulse duration | $\tau_0\,(fs)$ | 230 | 420 | 275 |
| Repetition Rate | $R\,(MHz)$ | 40/2 | 1 | 40/2 |
| Maximum pulse energy | $E_{p\,max}\,(\mu J)$ | 10 | 8 | 10 |
| Gaussian parameter | $M^2$ | 1.18 | 1.1 | 1.15 |

**Table 2.1:** Summary of the characteristics of the lasers used.

## 2.1 Fabrication setup

All fs fabrication setups used in this thesis share mostly the same scheme. The fs pulse generation is done by a commercial laser, which emits around 1030 nm, and the beam is directed through high power mirrors, with the possibility to have some fine control of the exposure power by rotating a $\frac{\lambda}{2}$ wave-plate followed by a polarizing beam splitting cube. There is also the possibility to generate second harmonic (515 nm) for exposure with higher energy photons. A microscope objective is used to focus the beam inside the sample. In order to finely control the sample translation, air-bearing xyz stages are used.

**Femtosecond laser sources**

All the lasers used in this thesis are Ytterbium based and thus emit around 1030 nm. These lasers provide turn-key operation and software based control of certain parameters. In table 2.1 we report the laser characteristics of the three micro-fabrication lines that were used. The default repetition rate of these laser can be pulse picked so that any divisor of that repetition rate (up to single pulse) can be used, only at the cost of lowering the average power.

### 2.1.1 Fabrication lines

We will explain in more detail the Satsuma HP line and briefly comment on the differences for the other two:

**Satsuma micro-fabrication line**

This was the main setup used for the fabrication of the vertical waveguides devices presented in chapter 3. A scheme of it is presented in figure 2.1.

The laser output comes with $\omega_0 = 1.9mm$ beam waist, which is first enlarged by a 2x beam expander consisting on two lenses with focal lengths $F_1 = 75mm$

and $F_2 = 150mm$. The power is finely tuned by a rotating half-waveplate (HWP) that is mounted on a motorized rotation stage, and a polarizing beam splitter (PBS) that transmits only the fraction of light with the polarization aligned to the PBS axis.

If we want to use the second harmonic ($\lambda = 515nm$) wavelength we can turn the flip mirrors $FM_b$ up and $FM_a$ down. This steers the beam to another path through lens $L_3$, that focuses it inside the LBO crystal (which is kept at optimum temperature for second harmonic generation (SHG) by an external controller), triggering SHG. The green wavelength beam is collimated by $L_4$ and directed back to the beam line. The two mirrors after $L_4$ are designed for selective reflection of the green wavelength in order to filter out any remaining IR light after the SHG.

In the case of IR fabrication, a second expansion system $BE$, can be activated by flipping up $FM_a$ mirrors. This can be used in order to fully fill larger clear aperture objectives (1 cm).

The sample is mounted on a XY air-bearing stage (Aerotech Ant series), and in the case of water immersion a Petri-dish was used to hold the sample immersed under water. The microscope objective is held on a Z stage. All the stages are fixed together against a granite stand for higher stability. This setup permits sub-micron precision in our fabrications. All the 3 axis plus the rotational stage can be controlled by a commercial computer software that runs on G-code, allowing us to program the fabrication of any shape in 3 dimensions. The sample is mounted on top of a gimbal manual tilting stage that permits to align its surface orthogonal to the incoming beam.
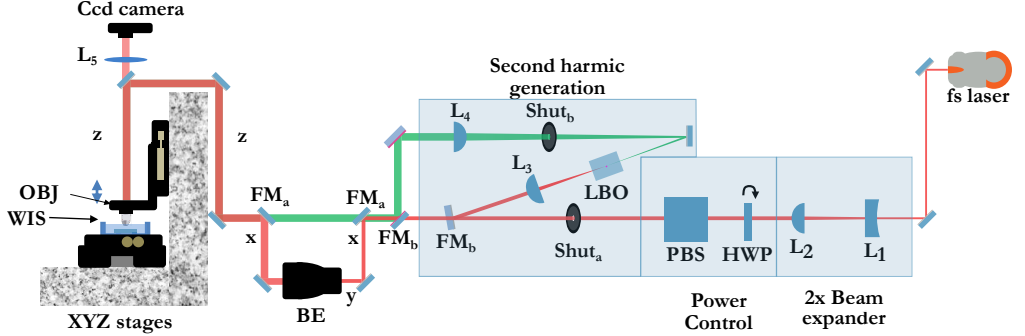


**Figure 2.1:** Scheme of the Satsuma laser fabrication line. L- lenses. FM - Flipping mirrors. LBO - lithium triborate crystal. Shut-shutters. BE - Beam expansion. OBJ - microscope objective. WIS - water immersion support. PBS - Glann-Thomson polariser cube.

**femtoREGEN micro-fabrication line**

This line was the main one used for the fabrication of the devices described in chapter 5. The only difference from the previously discussed micro-fabrication line is the existence of a single expansion system, since the beam spot size that comes from the laser is larger and the microscope objectives used here had smaller clear aperture (5 mm).

## Satsuma $HP^2$ micro-fabrication line

This is the laser line that was used at the university of Toronto (Prof. P. Herman's group) for fabricating air chambers with the FLICE technique (see chapter 4). The laser used is the same brand as the first one, although with already integrated second harmonic generation, and thus no external crystal is used. Both shutter and pulse energy are controlled directly by the laser software. By using a fire-wire cable we can send commands to control these settings within the fabrication program, automating the writing process.

## Alignment

The alignment procedure in any configuration is quite straightforward. We fix posts at key positions of the laser path that can fit alignment disks (thorlabs VRC2D05), and all the mirrors are set on mounts that can be tilted in both directions with two knobs.

After the laser is warmed up we progressively align using two mirrors each time and two alignment posts that are after those two mirrors. With the first mirror we align the beam to the first pin-hole, and then we do the same with the second mirror and pin-hole. Each of these pin-hole alignments slightly misaligns the beam from the other, so we need to go a few times back and forth. Eventually we will reach a point at which this misalignment is negligible, and then we move to the next section of the beam path.

In the last vertical path section of the laser beam we need high accuracy so the axis of the motion stages are orthogonal to it. We place a metallic mirror on top of the xy stages and watch the retro reflection on another pin-hole behind the last mirror. This method allows very precise and reproducible alignment and needs to be done before every fabrication, since thermal drift of the optical components can misalign the beam position at the objective lens by a millimetre a day.

Lastly the objective is screwed in the vertical stage, and we place the sample on the xy stages (adding the special sample holder and filling it with deionized water in case of water immersion objective). To fix the sample we typically use nail polish, since it is a very versatile solution that let us use samples with many different shapes and sizes on the same sample holder, and it can be quickly removed by applying acetone.

In order to have the sample surface orthogonal to the incoming beam, we use the lens ($L_5$) and a ccd camera placed behind the last mirror. We scan the microscope objective up and down until we find the diffraction pattern converging to a point. At that position we consider that the beam is at the surface of the sample. If the lens working distance is larger than the sample thickness we can also move deeper and see a second spot appearing, corresponding to the bottom surface.

Back at the top surface, if we scan laterally in x or y directions, we find the spot fading if the sample is not well levelled. Using a gimbal-based adjuster (GM100, Thorlabs) we tilt the sample. Since here we are using the stages to move both in z and xy this misalignment can be actually measured and the corresponding necessary adjustment on the gimbal can be estimated. With this

system we can have micrometer levelling over a 20 mm range, which is close to the limits of the actual flatness of the sample itself.

## 2.1.2 Depth calibration

One technical note that is often overlooked when explaining femtosecond laser writing systems, is the depth positioning. Since we are not focusing on the objective media but instead inside glass in order to find the depth where we write we need to correct for this refractive index mismatch, which leads to $z_{real} = z_{stages} \cdot \frac{n_{imm}}{n_{sub}}$, where $n_{imm}$ is the refractive index of the immersion medium (air/water/oil) and and $n_{sub}$ the substrate one.

If you abstract away and think only of the path from the sample to the ccd camera, you see that we have basically a two lens system (writing objective+$L_5$ in the setup of fig 2.1). Now when we have the focus of the laser beam at the surface of the sample, and since it comes collimated (and thus as if it comes from an object from infinity) it will focus at the focal distance of the objective lens. So now what will happen to the image at the ccd camera side? Let us consider now the focus at the surface of the sample as an object, it will come back and be collimated by the objective, and thus when it hits the second lens it will be focused again at the focal distance. Now this position is not necessarily the ccd camera, and thus we may have a shift to the real focus with respect to what we measure. But how sensitive is this misalignment? A scheme of an equivalent system can be found in fig 2.2.
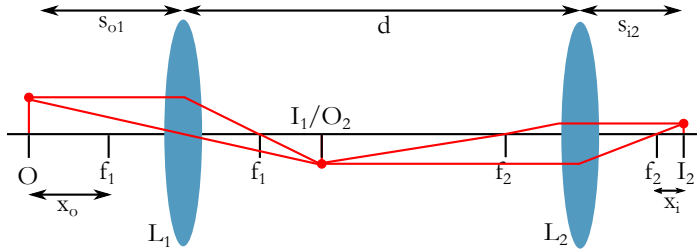


**Figure 2.2:** Scheme of the equivalent two lens system formed by the imaging setup.

Scraping out the system like this helps its analysis. The first object here will be on the sample surface. With simple ray tracing, and using Newton formalism $x_o = s_{o1} - f_1$ and $x_i = s_{i2} - f_2$ (in which $s_{o1}$ is the distance from the object to lens $L_1$, and $s_{i2}$ is the distance from the second image to the lens $L_2$), the following relationship can be found:

$$x_o = x_i \frac{f_1^2}{x_i (d - f_1 - f_2) - f_2^2} \qquad (2.1)$$

The error that we have in the estimation of the real focus is given by $x_o$. Notice that in this case it is the object that is fixed by the image, since we have the ccd camera fixed always at the same spot. If the camera is calibrated perfectly (i.e. lies at the focal spot of the second lens) $x_i = 0 = x_o$.

Using estimated values for our setup of d=350 mm, $f_1 = 20mm$ and $f_2 = 75mm$, if we consider a misalignment of 1 mm on the positioning of the ccd camera we have an error in the estimation of depth of $75\mu m$.

Another subtlety is that in most femtosecond direct writing systems (as in our case) we actually move the lens instead of the sample vertically. This means that depending on the sample height we will have different d values. Fortunately this change is typically low when compared with d. Still it has a small effect. If we consider a change of 1 cm of d in the conditions above we get a change an extra $1.4\mu m$ error. This means that for the range of fabrication this change is negligible, but if for some reason we need to fix the sample higher/lower then the depth calibration can be affected.

Finally, we can also consider this equation for the stability of the system over time. If we have mechanical drifts of up to $10\mu m$ we still have sub-micron error ($0.71\mu m$), which is enough in terms of reproducibility between fabrications.

## 2.2 Etching method

For the fabrication of some devices, after the irradiation using one of the previously described direct writing setups, we do a chemical etching step, using hydrofluoric acid (HF). Being a very dangerous acid, we need a dedicated fumehood to handle it. In particular to filter out the toxic fumes that are released when exposed to the air, but also to provide a protective window. The etching system used in our setup is shown in figure 2.3.

We use a bottle-top dispenser in order to safely deliver a precise amount of HF acid at 20% concentration, that we dilute later by adding the proper amount of deionized water. Since HF reacts with glass, we use beakers made with a proper polymeric material. The sample handling tweezers also have a special coating in order not to react and possibly contaminate the solution.After preparing the solution the sample is immersed in an ultrasonic bath for both temperature control and remixing the acid throughout the etching process.

Typically the etching process is done in multiple steps, with microscope inspection of the sample to check if there are any issues and also record the progress which can be useful for optimization. After each of these etching steps the sample is immersed in a 50/50 (Vol) mixture of isopropyl alcohol and deionized water in order to fully clean the sample from any HF residue.

In two of the chapters we use the FLICE technique in order to fabricate air chambers and channels. In both cases we use HF acid as the etchant material, although with slightly different methods.
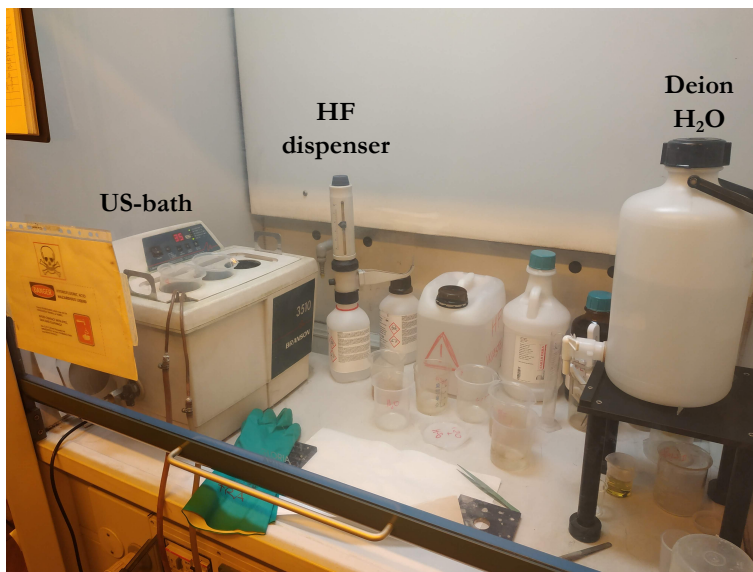
**Figure 2.3:** Etching setup.

## 2.3 Characterization setups and methods

In order to characterize the devices created in this thesis, several steps of characterization are needed to benchmark their quality and understand their. The device characterization also provides a valuable feedback to choose the right modifications for their improvement in subsequent fabrications.

### 2.3.1 Optical microscope imaging

Before any characterization, the samples are always observed under an optical microscope. This allows us, not only to check for ablation at any of the surfaces, but also to observe the uniformity of the waveguide, or control the etching process uniformity and roughness of the surfaces. Here we use a microscope (Nikon ME600), that can add polarisers to the optical path and be used for enhancing contrast and see stress patterns on the waveguide. A high resolution CCD camera (PixeLINK B871) attached to the microscope is used for direct image acquisition.

### 2.3.2 Waveguide Characterization
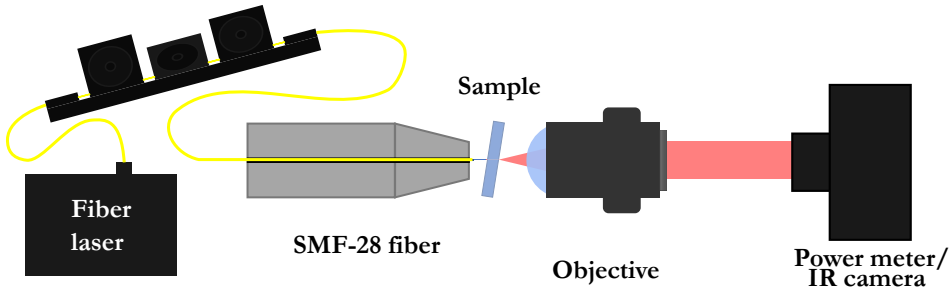


**Figure 2.4:** Characterization setup used for measuring losses and imaging the mode propagated inside the waveguide. The sample is tilted for the general case of a tilted waveguide.

Most waveguide characterization can be done with the setup configuration presented in figure 2.4. We used a tunable laser, that outputs directly to a commercial single mode fibre (SMF-28) at 1550 nm.

We couple directly to the sample from the fibre tip (which is called butcoupling). This method of coupling is quite straightforward since we can actually look through a microscope at the physical distance between the fibre tip and the waveguide, and make a first rough alignment by eye (under the right illumination conditions the waveguides can also be seen). Although it is only advisable if working with waveguides with similar numerical aperture as the fibre. Otherwise coupling is typically done in free space, and the objective used to couple light needs to be properly chosen to match the expected numerical aperture of the waveguide.

The first alignment is done with visible (red) wavelength. The sample is mounted on a manual stage that allows for micrometer manipulation in axis, and

angle tilting.

In order to align the tilting of the sample two methods can be used. In the short waveguides used in this thesis (<1 mm), and coupling with the red wavelength, we can project the image on a white paper and see the output mode of the waveguide.

The other method is sending light through the sample out of the waveguide, and fixing the white paper with a marker where the spot is. When moving back to the waveguide, if it is collinear with the fibre we should see the spot around the same position, otherwise we correct accordingly.

These methods don't work for curving waveguides though. In this case we always fabricate a straight waveguide close to the curving one with the same input angle of the curved one, and align the angle with it before coupling the curved waveguide.

To control the input polarization we use a manual fibre polarisation controller (FPC560), and place a polariser at the space between the collecting objective and power meter. In order to have linear polarization in H or V we rotate the polariser orthogonal to it and twist the three different knobs until we minimize the signal at the power meter.

**Mode profile**

The mode profiles are most often the first data we collect after the microscope characterization. During this measurement we can check if the waveguide is multi-mode, the quality of the coupling and if it is symmetric.

Since we work with 1550 nm we need a camera tailored to work in that regime, since most ccd camera sensors are blind at that wavelength. In our case we use a Spiricon (SP620U-1550) which has a thin layer of phosphorous coating to convert 1550 nm light to visible. The phosphorescent response is inherently non-linear but the camera output comes already calibrated with a calibration curve, such that it is proportional to the input intensity, and so we have:

$$A(x,y) = CI(x,y) = CE^2(x,y) \tag{2.2}$$

where A is the recorded bitmap, and C is the proportionality factor.

The camera should be placed at a distance such that we fill it as much as possible with the measured mode so we maximize spatial resolution. The input power needs to be kept just below saturation so we use the full intensity dynamics, without losing information in saturation or damaging the camera.

To convert the pixel map to the real mode size we need to do some kind of calibration. Our approach is to use the SMF-28 fibre itself, and image it on the beam profiler, keeping the same distance between the imaging lens and the profiler. This way the magnification of the system is kept the same as before.

The modes obtained are analysed by a Matlab program and the spacial field distributions can be calculated using equation 2.2. The proportional factor C is eliminated by normalizing the electric field profile. In most cases the modes acquired on the camera follow closely a Gaussian profile, and we can either do a numerical fit or doing a knife edge estimation of the mode size by measuring the positions at which the field is at $E(x,y) = \frac{E_0}{e}$. By comparing the measured

fibre mode size in pixels to the know dimensions from data-sheets we calibrate the pixel size and get the waveguide mode profile and size in its right dimensions.

**Refractive index change reconstruction**

From the mode profile, an algorithm was created in order to estimate the refractive index change in the waveguides (based on previous results [83]). Starting with the electromagnetic wave equation:

$$\frac{\partial^2 E}{\partial x^2} + \frac{\partial^2 E}{\partial y^2} + \frac{\partial^2 E}{\partial z^2} - \mu \epsilon \frac{\partial^2 E}{\partial t^2} = 0 \tag{2.3}$$

and supposing solution based on plane waves propagating in z $E(x, y, z, t) = E(x, y) e^{-i(\beta z - \omega t)}$ on equation 2.3 we arrive at the following relationship:

$$\frac{\partial^2 E(x, y)}{\partial x^2} + \frac{\partial^2 E(x, y)}{\partial y^2} + E(x, y) \left[\mu \epsilon \omega^2 - \beta^2\right] = 0 \tag{2.4}$$

supposing now the conditions of $\mu_e \approx \mu_0$ and considering the refractive index of the material $n^2 = \mu \epsilon c^2$ and the propagation constant of the wave $\beta = n_{eff} \sqrt{\frac{2\pi}{\lambda}}$ we get the following relationship:

$$\left(n^2 - n_{eff}^2\right) = -\frac{\nabla^2 E(x, y)}{k^2 E(x, y)} \tag{2.5}$$

We do not know exactly the effective index but we can approximate it to the substrate one $n_{eff} \approx n_s$. Notice that the left side of the equation gives us the refractive index change $\delta n(x, y) = n(x, y) - n_s$ at each point $(x, y)$. The right side of the equation can be calculated from the mode profile obtained $A(x, y)$. If you substitute equation 2.2 on equation 2.5 you see that the proportionality factor is cancelled. The last unknown variable is the size of finite differential, which corresponds to the pixel size of the camera, and is obtained from recording the fibre mode profile, as seen before.

One of the main limitations of this approach lies on the Laplacian of the electric field. Calculating a second derivative means amplifying the noise twice. In figure 2.5 you can find an example of the refractive index change profile obtained with and without proper noise filtering. It is evident that the high frequency noise, present in the original signal, is quickly amplified when we use finite differentiation. With proper filtering we can get a reasonably smooth signal.

### 2.3.3   Losses characterization

One important benchmark of the quality of a waveguide is its loss. We call the overall loss from the waveguide, as if it was a black box, insertion losses. It is typically expressed in decibel notation

$$IL_{dB} = -10 \cdot \log_{10}(T_W) \tag{2.6}$$

where $T_W = \frac{P_{out}(W)}{P_{in}(W)}$. Experimentally $P_{In}$ is measured by removing the waveguide sample from the fibre and collecting all the power directly to the power

31
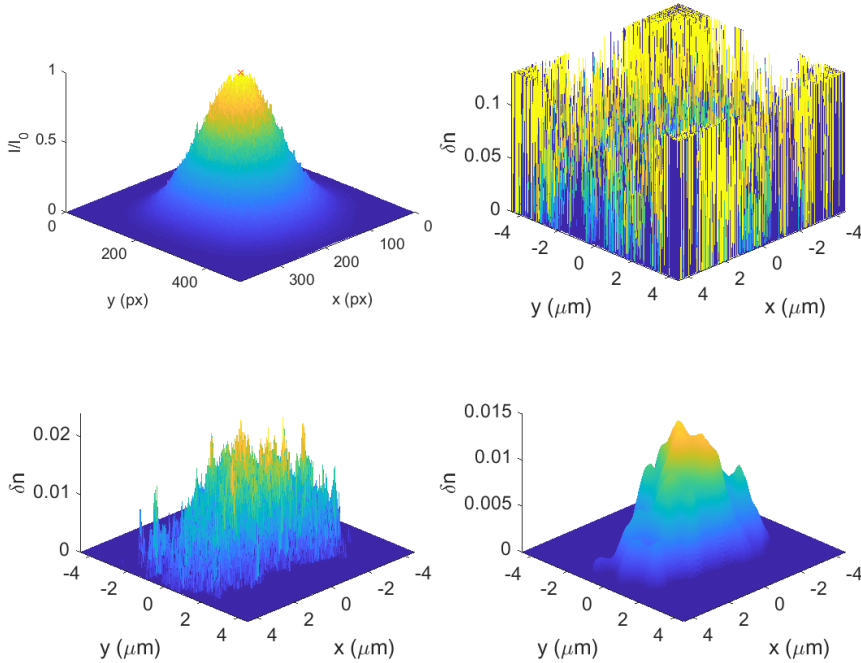
**Figure 2.5:** a) signal obtained in the ccd camera. b) c) d) Refractive index change map calculated with different levels of smoothing of the original signal (2/4/5 filters)

meter. This way we can take into account also Fresnel losses. $P_{out}$ is the maximum output power that we can get out of the waveguide when aligning the fibre with the waveguide. Insertion loss measurement is thus always dependent on the skill and method in the aligning procedure. Insertion losses can be then decomposed in four main sources of loss: propagation losses (PL), bending loss (BL), Fresnel loss (FL) and coupling loss (CL). Using the decibel notation we can simply express them as a sum: $IL_{dB} = FL + CL + BL + PL$.

Propagation losses arise from two main mechanisms. The first is overall roughness on the waveguide walls. These small imperfections mean that locally the mode structure varies and there is the possibility of coupling with radiative modes that cause light to scatter away. The other source are defects, or absorption centres that are either already present in glass or created by the modification. A more in depth analysis of waveguide propagation losses can be found in [28]. Propagation losses are estimated indirectly by measuring all the other contributions and subtracting from the insertion loss:

$$PL_{dB} = IL_{dB} - CL - 2 \cdot FL \tag{2.7}$$

Fresnel losses are caused simply by reflection at interfaces of different refractive indexes. Since the waveguides studied are written in fused silica, when we couple light into the sample there is typically a refractive index mismatch

air-glass. This loss is given by the Fresnel equation:

$$T_{S/P}^{FL} = \left[1 - \left(\frac{n_{2/1}\sin\theta_1 - n_{1/2}\sin\theta_2}{n_{1/2}\sin\theta_1 + n_{1/2}\sin\theta_2}\right)^2\right],\tag{2.8}$$

In the case of fused silica @1550 nm and normal incidence we have $n = 1.444$ and $FL = 0.15dB$. Note that this is loss per interface, so we should double this value in the contributions for insertion losses. In the case of a tilted surface the Fresnel reflection also increases, and more importantly it starts depending on polarization. This effect is however negligible in the conditions explored in this thesis: at 9° we have 0.15 dB for $s$ and 0.14 dB for $p$ polarizations.

Coupling losses come from the mismatch between the electric field at the input $E_{in}(x, y)$ and the waveguide mode $E_{wg}(x, y)$. These losses can be expressed by the superposition integral:

$$CL_{\mathrm{dB}} = -10 \cdot \log_{10}\left(\frac{|\iint E_{wg}E_f dxdy|^2}{\iint |E_{wg}|^2 dxdy \cdot \iint |E_f|^2 dxdy}\right).\tag{2.9}$$

this calculation can be simplified in the case of two Gaussian modes to a simple equation dependent on the mode widths of the fibre $\omega_{fb}$ and waveguide $\omega_{wg}$, with the possibility of the later having ellipticity between x and y direction which is common on femtosecond direct written waveguides:

$$CL_{\mathrm{dB/cm}} = -10\log_{10}\left(\frac{4\omega_{fb}^2\omega_{wg,x}\omega_{wg,y}}{(\omega_{wg,x}^2 + \omega_{fb}^2)(\omega_{wg,y}^2 + \omega_{fb}^2)}\right)\tag{2.10}$$

with the recorded mode profiles of the input fibre and the waveguide we can estimate the coupling losses by either of these two methods.

Finally the bending losses originate from the fact that the curved shape of the waveguide causes a distortion in the guided field distribution, which again leads to partial coupling to radiative modes on the external side of the curve. These losses increase exponentially with the radius of curvature and can be typically modelled with the following formula [84]:

$$BL_{\mathrm{dB/cm}} = C_1 e^{C_2}.\tag{2.11}$$

where $C_1$ and $C_2$ are numerical constants that depend on the waveguide mode profile. In a broad view these losses depend on the mode confinement, i.e. how well confined is the guided mode inside the core. Therefore, these losses are higher for low index contrast waveguides. A detailed derivation of this equation can be found in chapter 5 of [85].

### 2.3.4  Birefringence measurements

The polarization state of a beam can be completely characterized by the adimensional Stokes vector:

$$\vec{S} = \begin{bmatrix} S_0 \\ S_1 \\ S_2 \\ S_3 \end{bmatrix} = \begin{bmatrix} I_0 \\ (I_H - I_V) \\ (I_D - I_A) \\ (I_R - I_L) \end{bmatrix} \cdot \frac{1}{I_0}\tag{2.12}$$

Where $I_0$ is the total intensity, and $I_H, I_V, I_D, I_A, I_R, I_L$ are the transmitted intensities when projected to horizontal, vertical, diagonal ($45°$), anti-diagonal($-45°$), right rotational and left rotational, respectively. The effect of any device on the polarization can be described by its Müller matrix $\boldsymbol{M}$:

$$\boldsymbol{S_{out}} = \boldsymbol{M} \cdot \boldsymbol{S_{in}} \tag{2.13}$$

For the specific characterization of the waveguide birefringence, we used the dedicated setup shown in figure 2.6.
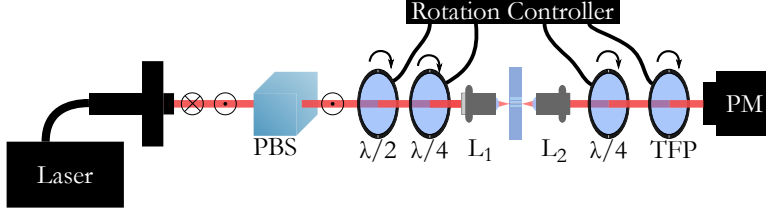


**Figure 2.6:** Birefringence analysis setup. Legend: PBS- Polarizing Beam splitter; L- Lenses; $\lambda/2, \lambda/4$ - half,quarter waveplate; TFP -Thin film polariser; PM- Power meter

The laser beam emitted is in a mixed state of polarization. The PBS leaves polarization purely horizontal. The first $\lambda/4$ and $\lambda/2$ can create any desired polarization at the input of the sample. Light is coupled and recolimated using aespheric lenses. at the output we have another $\lambda/4$ and a polarizer that can be independently rotated, and that allow us to select only one of the six base polarizations. The four rotating elements are actuated by the same controller, that is connected to a computer.

The alignment is done by first aligning the laser with a couple of pin holes put at the same height and without any components. Then we align each component, maintaining the height and position of the spot at the second pin hole. first the PBS, and then the TFP. Here we also rotate the TFP until we see a minimum at the output power. Then goes the other waveplates, and with each we minimize the output power. This position is saved on the motor controlling software. Then we had each of the objectives, and finally the sample. We align it in the same way as we align for the losses measurement, the only difference is the coupling objective position, that is found by placing a beam splitter behind the lens and move the lens axially until it focuses a spot in the retro reflection.

Once the alignment is done, a program was created to automate the movements of the four rotational stages, and we record the output power observed at each combination of input/output of the six projections mentioned before. This amounts to a total of 36 measurements. Some of these values are redundant but this allows for some verification on the validity of the measurement and a better fit.

All these measurements are sent to a Matlab code that calculates the output Stokes vectors for each of the six inputs, which leads to 6 equations. Depending on our expectations we can try different Müller matrices models. A common first trial is a mono-axial birefringence that has the following Müller matrix:

$$\mathbf{M_{wg}} = \begin{bmatrix} 1 & 0 & 0 & 0 \\ 0 & \cos^2 2\delta + \sin^2 2\delta \cos\phi & \sin 2\delta \cos 2\phi(1 - \cos\phi) & \sin 2\delta \sin\phi \\ 0 & \sin 2\delta \cos 2\phi(1 - \cos\phi) & \sin^2 2\delta + \cos^2 2\delta \cos\phi & \cos 2\delta \sin\phi \\ 0 & \sin 2\delta \sin\phi & -\cos 2\delta \sin\phi & \cos\phi \end{bmatrix},$$

$$(2.14)$$

with the fast axis at $\delta$ angle from the horizontal and $\phi$ phase difference between the fast and slow axis. With the fit we can find what is the total phase difference that the device adds. Knowing its length we can retrieve the birefringence $l \cdot B = \phi$. The last comment is that the angle solution is actually $\phi + n \cdot 2\pi$, with $n$ being any integer. In order to calculate $n$ we need to do at least a second measurement of the same waveguide with a different length.

## 2.4 Brewster windows characterization

Two methods were used for characterizing the windows described in chapter 4 after fabrication. The respective schemes can be seen in figure 2.7. For measuring the polarization ratio, we shine light from an optical fibre through the window , and collect with a lens onto a photo-detector (Newport 818-IR). As a light source we use an amplified spontaneous emission source (Thorlabs ASE FL-002) that emits at 1530-1610 nm. This source provides a random polarization at the input, and showed no noise from Fabry-Pérot effects when transmitting through the thin windows used (1 mm thickness).
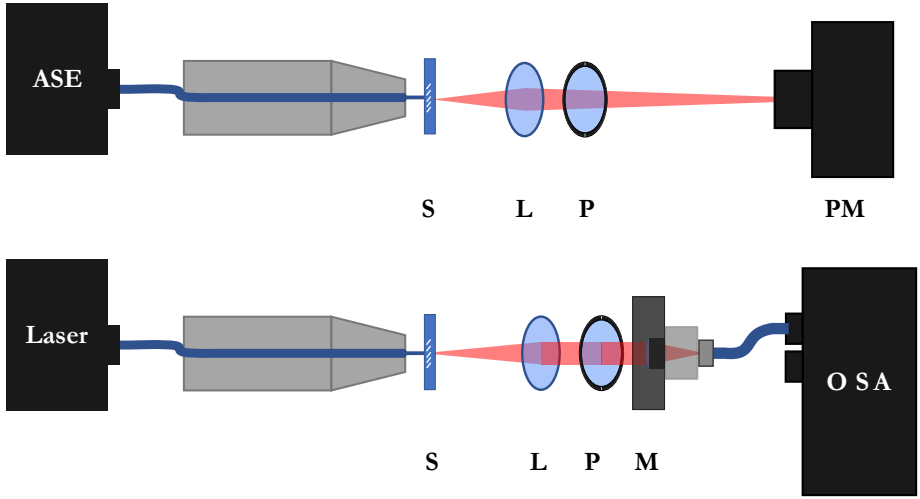


**Figure 2.7:** Schemes of both characterization setups used for a)Polarization ratio measurement b) Spectrum characterization. Legend: P-Polariser; L- Lens; S-Sample; PM- Power meter; OSA: Optical spectrum analyser; ASE: Amplified spontaneous emission

Angle calibration is achieved by looking at the back-reflection from the fibre. In the optical path we insert a polariser (Thorlabs LPNIR050-MP), that we can rotate to vertical (V) and horizontal (H) orientation. Alignment is achieved by sliding the sample, and monitoring the power read at the power meter with the polariser in H position (high transmission), we can observe the value going down when we are shinning through the edge of the window and up again when in the centre. At this position we record the values for the two configurations $(P_H, P_V)$, and calculate the polarization ratio:

$$PR = \frac{P_V}{P_H} \tag{2.15}$$

For measuring insertion losses we just need to slide the sample to a region without any windows and register a reference power $P_0$. We fix the polariser in

H position since that corresponds to $p$ polarization in the window scheme:

$$IL_{dB} = 1 - \frac{P_H}{P_0} \tag{2.16}$$

In order to characterize the spectral response of the polarization ratio, we used a similar setup (figure 2.7b), only adding a fibre mount after the first lens, that couples the light onto a fibre and to an optical spectrum analyser (OSA). The input laser is a broadband laser source ($1.27$-$1.71\mu m$). It is linearly polarized, so in order to be able to measure both polarizations we manipulate the output polarization by twisting the fibre until we have a reasonable distribution of power on H and V polarizations.

The alignment is done by first aligning the fibre with the two lens, maximizing the input power at the OSA. After this we introduce the sample, and in order to check the window alignment we introduce a power meter between P and M and align the centre of the windows the same way as for polarization ratio measurement. The beam path is affected by the new device, and thus the alignment with the fibre mount is no longer perfect, but since the values that we want are relative (vertical polarization power vs horizontal) it should not be a problem. Even so at this point we can finely tune both lenses in order to achieve maximum power at the OSA. After recording the spectra transmitted through each window we also do the same with the beam going through the window, for both polarizations. Since we are working in logarithmic units (dB) we can just subtract each of the signals $P_H$ and $P_V$ by the respective backgrounds $P_{H0}$ and $P_{V0}$. With these normalized values we can get the polarization ratio spectra:

$$PR_{dB}(\lambda) = (P_H(\lambda) - P_{H0}(\lambda)) - (P_V(\lambda) - P_{V0}(\lambda)) \tag{2.17}$$

# Chapter 3

# Femtosecond direct writing of vertical waveguides for optical interconnection

In this chapter we will approach the main work done during my PhD. We will start by giving a short background on optical interconnection and where vertical waveguides can become to be a part of it. Then we will discuss the process with all the main results of all the approaches we tried from the beginning until the final solution that we found to write vertical waveguides in fused silica. Finally we will show the preliminary results we have on their integration with the channel waveguides, and the stacking of vertical waveguides.

## 3.1 Motivation

It is a well known trend that communication has been following a continuous exponential increase for the past century. Since the beginning of the availability of internet to the consumer, every year there is the expectation for larger available bandwidth and cheaper prices. In the past decade smart-phones brought another boom in mobile data communications, and now people use the internet in every waking hour in some cases. The availability itself generates further new applications and demand for more data every second. The last trend was the various streaming industries. Now-a-days most people listen to music by streaming instead of storing them in their personal devices. And the same is happening for videos. New trends are already being seeded such as intelligent equipment for houses. In the future it is expected that most of the house appliances will be connected on-line.

The backbone of all this constant revolution lies on a massive infrastructure of data centres, routers, internet exchange points, etc. that manage all the information and distribute it across the world. Whenever you send data from let us say Peru to Italy, it needs to bounce through many routers before it reaches the other computer. Now all this infrastructure translates in many cables and rooms of computers dedicated for receiving, sorting, and sending messages. All these connections used to be electrical in the beginning. Now-a-days huge fibre cables lie on the ocean floors that allow fast connection between the different continents. Internet service is also slowly changing into optical fibre technology, but still some of the infrastructure relies on electrical interconnection. Let us analyse now the fundamental differences between these two main technologies.

**Electrical vs optical interconnection**

An interesting analysis is done by David Miller [86] comparing the physics of optical and electrical interconnections. One important remark is that actually electrical and optical signals share the same nature since they are both electromagnetic waves. A common misconception in popular arguments is that electric cabling is slower than optical communication. Actually in some cases its the opposite, depending on the dielectric material used. In fact electrical signals are not carried by electrons, but by photons. The real difference that makes optical interconnection advantageous comes from its wavelength, frequency and photon energy, compared to electrical counterpart. These values are summarized in table 3.1.

|  | Electrical | Optical |
|---|---|---|
| **Wavelength** | 3 cm-30 m | 0.5-2 $\mu m$ |
| **Frequency** | 10 MHz-10 GHz | 100-500 THz |
| **Photon energy** | 40 neV-40 $\mu eV$ | 0.5-2 eV |

**Table 3.1:** Comparisson of the eletromagnetic wave characteristics corresponding to optical and electrical interconnection.

These three aspects are all related through $c = \lambda f$ and $E = hf$, and they

39

explain most of the optical interconnection advantages.

The high frequency of light enables higher speed modulation. When compared with electrical interconnections dispersive effects in fibres are negligible and the propagation loss is largely independent on frequency. This allows for the exploration of wavelength multiplexing as a method for increasing transmission rates and reducing density [87][88][89][90]. A general formula has been reached for electrical connections that relates the physical dimensions (length l and cross-section area A) to the maximum bit rate: $B_{max} \approx B_0 A/l^2$ with $B_0 \approx 10^{15-17}$ depending on the specific line. This simple factor explains why particularly long distance connection (e.g.intercontinental) was the first application where optical fibres took over. Now-a-days that we are approaching the Tb/s bit rate this hard limit is getting closer and the need for new technology inevitable. This limit can be circumvented by methods such as multilevel modulation but these always come at a cost of complexity and circuit size. Optical cables don't suffer nearly as much dispersion and wavelength dependent loss, and for the same interconnect size and length can carry 9 orders of magnitude the bit-rate [91]. Temperature induced phase delay is another issue, that can induce errors in the read of the clock signal, with 40% change over 100° compared to 0.07% for a 10 m optical fibre. Electrical wires also act as antennas at high frequencies which creates big issues with cross-talk, which is largely negligible in optical connections. Another advantage of optical interconnection is the possibility of using short pulses, particularly as clock (which can be used as an external auxiliary for electronic connections). This can also be exploited for time-multiplexing [92][93].

On the other hand the short wavelength of light means that it is easily confined in dielectric materials(a fibre core is $10\mu m$ which is 10 times the wavelength). In electrical connections instead conducting materials are necessary, which are typically lossy. Even superconductors show losses at high frequency. Another consequence of the short wavelength is the possibility to explore propagation in free space, which is unthinkable for electromagnetic waves of cm wavelength (diffraction limit divergence is proportional to $\lambda$). Some global interconnect topologies that require beams to cross between each other such as perfect shuffles are easy to make with simple optical imaging systems. Making true arbitrary geometries is not as straightforward though, and this can be done easily with electrical interconnections.

Finally the main consequence of large photon energy of light is that its generation and detection is in the general case quantum mechanical, whereas electrical signals are classical since they result from averages, and that is why describing them as photons has so little use practically. One advantage that comes from this is voltage isolation. The detection of photons in a photo detector has no feedback from its source. In fact optical isolators consisting of a simple light emitting diode and a photo diode side by side connected to different circuits are already used to connect two electrical circuits without feedback effects.

For a current state of the art on the latest advances on each of the components for optical interconnection we recommend two recent reviews [94][95]. The results of our research apply more particularly on the interconnection between different photonic chips. We will review now the latest advancements in this particular application.

## Current solutions

Several proposals have been put forward in the recent times for connecting between photonic chips, in particular between silicon photonic chips which are now widely implemented in integrated photonic systems.

An interesting solution to connect between two silicon chips was found by using total internal reflection mirrors both for directing light out upwards and into another chip [96], using a flipped chip on top (with the PLC waveguides at the bottom). This provided a broadband solution with 2.5 dB coupling loss. The mirrors were fabricated by anisotropic KOH etching that happens on the edge between oxidized and exposed silicon.

An example on the use of femtosecond direct writing for optical interconnects comes from [97]. Here they use fs direct writing in eagle2000 glass for fabricating an interposer that allows flexible connections between multiple silicon photonics chips. The waveguides are written transversally. The coupling from the silicon chip is done with a grating to send light vertically and then a total internal reflection mirror for coupling inside the fs waveguide. Low insertion losses of about 1.5 dB/cm were achieved on the fs waveguide but the gap between the bottom grating and the top mirror adds extra losses that are not negligible.

Another possibility is photonic wire bonding [98]. Polymer waveguides were fabricated that allowed very flexible connection to connect two chips in close proximity, with an insertion loss of 1.6 dB. This method is although limited to very short distances.

There is also some results on plasmon-polariton waveguides for interconnecting chips [99][100] but their high propagation loss limits their practical use.

## Teraboard project

A European project started in December 2015 in a collaboration between three main industrial partners (Alcatel, ST Microelectronics, Ericsson) and research groups (CNIT, IMEC, iMinds, CNR, EPIC and UPV) from across Europe. The main objective in this collaboration is to provide advanced intra-board and edge interfaces with ultra-high density and scalability in bandwidth, low insertion loss and energy consumption. Intra-board communication will be done without wave division multiplexing (WDM) in order to reduce the footprint from fibre connectors. One of the innovative features for allowing this to happen lies in the use of 3D stacking of layers of glass in order to increase the density of connections. You can see in figure 3.1 a scheme of the proposed solution for connecting two silicon on insulator chips (SOI).

In this geometry we join together the PLC technology, with waveguides that have the lowest propagation losses on the market ($<0.03$ dB/cm), for the long distance propagation, and the fs-laser-written waveguides to do vertical guiding in order to explore the extra dimension that otherwise would be difficult to exploit. The samples are made of fused Silica and have 675 $\mu m$ thickness. Fused Silica was the chosen substrate since it is already well known for fs direct writing of waveguides, and is quite compatible in terms of thermal expansion with silicon photonics technology. The coupling is done by a grating at the bottom and a micro-mirror at the top. Both these components were done by our partners.
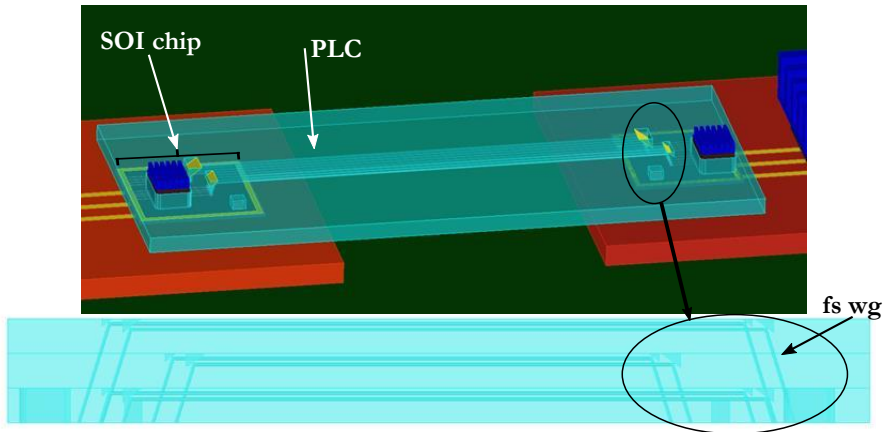
**Figure 3.1:** Scheme of the interconnection between two silicon on insulator (SOI) chips, with a close-up of the Star-board (bottom image) with the vertical vias on each side and the long channel waveguides on top of each layer made by lithographic PLC technology.

## 3.2 Vertical vias

In the quest for achieving vertical waveguides we tried many different approaches until we found the optimal recipe for our application. We will explain with reasonable detail all these steps as the failed attempts can be as informative for anyone wanting to do further research on this application. We had some basic requirements for these waveguides due to the specifications of our project. They had to have low insertion losses (<1 dB), no birefringence for TE mode input and a small tilt (up to 6 degrees) in order to optimize coupling both from the grating and into the mirrors.

### 3.2.1 Type I waveguides

The simplest way to fabricate waveguides as seen in the background chapter is to do a single scan with enough pulse energy for achieving a positive refractive index change.

**Single scan**

From literature we expected in advance that using green wavelength could provide better results as this is the best wavelength to write good transversally written waveguides in large band-gap materials such as Fused Silica.

We made a series of tests changing both repetition rate (1kHz to 1MHz), pulse energy and scan speed. The first tests were done with the High-Q line setup (check section 2.1.1 for more details). We also tested out three different microscope objectives. The lateral profiles of these waveguides can be seen in figure 3.2.

First we used the 50x microscope objective that is commonly used in our group for transversal fs waveguide fabrications. From the profile it was quite

obvious that spherical aberrations were too high on the bottom part. Next we tried using a 63x objective that has a ring for correcting aberrations. We fixed this ring at middle depth of the sample thickness in order to minimize the overall aberrations. As seen in the profile actually the aberrations are even worse than in the 50x case, since although the optics are optimized for a given depth in glass, aberrations increase faster towards the extremities. Indeed we see that we only have a clear modification at the centre of the glass while it completely fades in both directions, due to the increasing aberrations that disperse the energy, so that we no longer have effective non-linear absorption.

Finally we tried another dry objective, that had in particular a much lower NA (0.3). Our reasoning was that since it has such a low focusing angle, the spherical aberrations would have a smaller role. Indeed we see some improvement on the uniformity of the modification over the whole length of the waveguide.

For all these waveguides though we found single mode waveguiding at red wavelength, and completely no waveguiding at 1550 nm. The logic conclusion is that the induced refractive index change is not big enough in order to have a low loss mode at 1550 nm with this modification size.

In fact if we pick the step index model from section 1.2.1 in order to have a normalized frequency of 1.5 needed for a well guided mode, and considering a core radius of $1\mu m$, which was on average the size of the modification that we observed in our single scans (check figure 3.3), we would need $5 \times 10^{-2}$ refractive index change which is far more than what has been observed in femtosecond refractive index modification of fused silica.
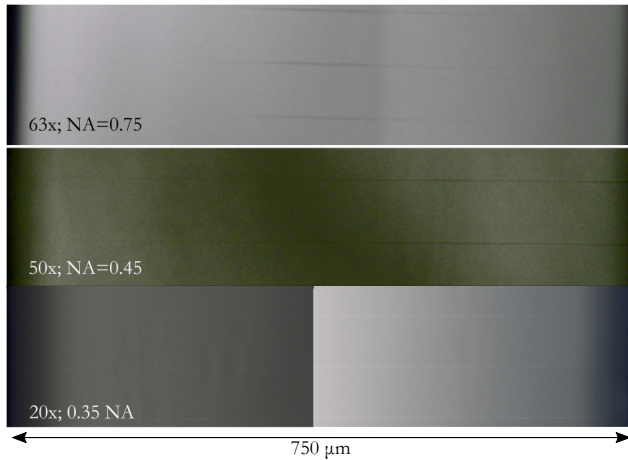


**Figure 3.2:** Lateral images of vertical waveguides written with three different microscope objectives. The writing beam entered through the right side of the images (top of the glass).

**Multiscan**

Since the single scan waveguides were able to guide in red wavelength, it means we were able to induce some positive refractive index change, and thus if we manage to either increase the area or the amplitude of index modulation we should be

able to guide at 1550 nm. So the next set of experiments was focused in testing if multi-scanning could be a solution. We tested writing the same waveguide multiple times. We continued using the 20x objective from before since it was the one that provided the most uniform modification. In figure 3.3 we see the profile of a waveguide that had a single scan, and another with exactly the same writing conditions but that we scanned 10 times. As can be seen in figure 3.3, there is no visible difference, and when coupling them with 1550 nm light there was still no measurable output.
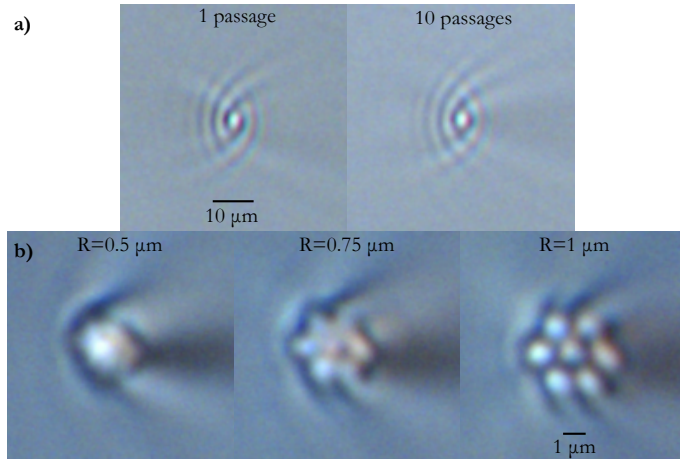


**Figure 3.3:** Top microscope of two different approaches for multi-scan writing. a) Single and 10 passages on the same position. b) Multi-scan filling waveguides. All have only an extra layer of 6 lines written surrounding a central one, with different distances between them.

We also tried filling an area by making multiple scans. In this case we start with the first central scan and then add layers that had an hexagonal shape. This shape gives equal distance from the central waveguide to the outer layer as between these neighbouring waveguides, which should provide an uniform modification. These waveguides were written with 6.9°, since that was the projected angle that we needed for our waveguides at the time. In figure 3.3 you can see three of these waveguides, with only one extra layer made by six waveguides with different radial distances. It is possible to observe that the overall modification merges together when we write the second layer at the an optimal distance $(0.5\mu m)$.

After making this proof of concept we tested different repetition rates (10/100/1000 kHz), scan speeds (10/50/100 $\mu m/s$) and pulse energies (0.1-0.15 $\mu J$). We tested making two and three layers of these waveguides. For the extra two layers we calculated the number of lines such that we have equal distance between the waveguides on the same layer, and with the other layers. With some simple calculations we can see that this number is $N_l \approx 2\pi l$, in which l is the layer number. This way we keep constant density on all the written area. The distance between layers was kept the optimal one found in the first experiment $(0.5\mu m)$.

The best results were obtained for the three layer waveguides, and a selection of these can be seen in figure 3.4. For the first time we saw waveguiding at 1550

nm, and as you can see in the microscope pictures we managed to create a uniform modification composed of many single written lines. Still these waveguides showed very high insertion loss (>7 dB), and by looking at the mode profile it seems to be leaking from the tilted side. This could be due to a non-uniform fabrication of the area since each line is written through already modified material, and particularly when reaching the final lines the modification that was built up can affect the beam path and thus disrupt the focus. Also its possible that the modification is so weak that even at a small angle is enough for coupling with radiative modes, and what we are seeing are the propagation losses.



| R= 10 kHz | R= 100 kHz | R= 1 MHz |
| Ep = 0.2 μJ | Ep = 0.15 μJ | Ep = 0.15 μJ |
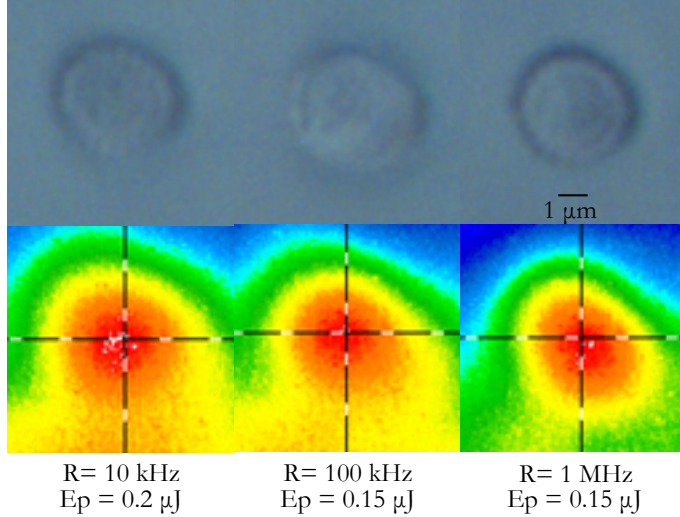
**Figure 3.4:** Profile picture of the surface (top) and imaged mode at 1550 nm for the three best waveguides obtained in the last multi-scan filling experiment. All of them were composed of three layers of waveguides separated by $0.5\mu m$.

We ended up abandoning this approach at this point since another solution was proving more feasible.

### 3.2.2 Type II

Instead of directly writing the waveguide's core, we irradiated an helix-shaped path that produced a modified cylindrical surface inside the glass. Due to the stresses induced in the surrounding material we have an increase in refractive index inside the cylinder and thus we can have waveguiding. A scheme of this method can be found in figure 3.5.

Using 1 MHz for repetition rate and keeping green wavelength we tested different pulse energies (0.1-0.2 $\mu J$), scan speed, radius ($6 - 10\mu m$) and pitch of the helix (1-5 $\mu m$). The writing laser polarization was linear, corresponding to the V polarization in the recorded modes. The lowest insertion losses we found in this regime were 1.7 dB. This was achieved for a $8\mu m$ radius of the helix. The respective waveguide mode is shown in figure 3.6. We also see some difference between the output mode when coupling from the two sides, which indicates
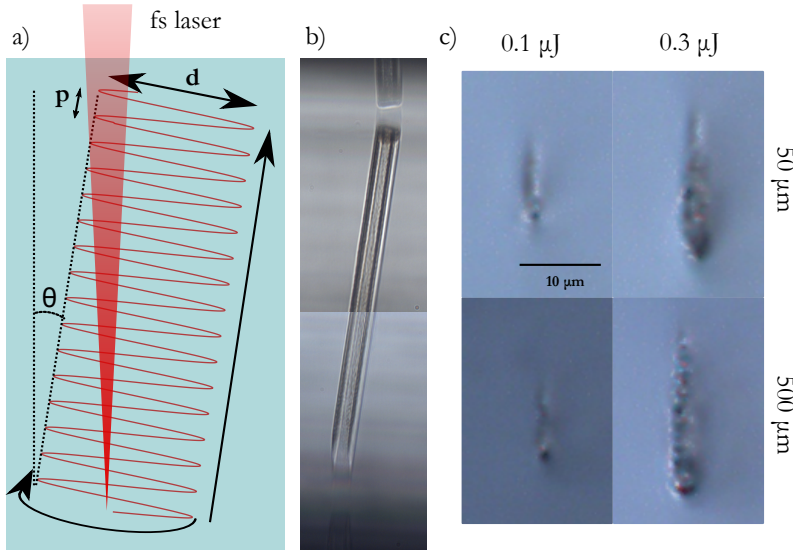
**Figure 3.5:** a) Scheme of the type II waveguides fabrication method. The laser scans in a helix pattern starting from the bottom to the top, with pitch p and diameter d. b) Example of a tilted waveguide after fabrication. c) Microscope side-view of transversal written scan at different depths and pulse energies for 1 MHz repetition rate and green wavelength.

tapering of the waveguide. This tapering is due to the spherical aberrations that disperse the energy and reduce the index modulation.

We observed that if we decreased the radius of the helices the mode size would decrease as expected, and would also increase the insertion losses. But when increasing the radius past $11\mu m$ we started observing moving mode behaviour, which is something we generally observed in these type II of waveguides. This phenomena was seen while coupling in the central region of the waveguide, and when moving the input fibre we would see the output mode move along with the input, instead of keeping the same position at the camera and just fading as the coupling efficiency is reduced by the misalignment. On the other hand, increasing the mode size will eventually increase the coupling losses enough that it would affect insertion losses too.

After exploring different pitch sizes we ended up fixing it at $1\mu m$. We observed a 5% insertion loss reduction from $2\mu m$ to $1\mu m$ pitch. This corresponds to a doubling in fabrication duration, which took at the moment around 1 h per waveguide with a scanning speed of $10\mu m/s$.

As can be seen in the mode profile figure the mode size resembles quite well the fiber one. In fact coupling losses are around 0.2 dB for these waveguides, which means that most loss (>1 dB) comes only from propagation losses.

**Change of fabrication line**

After the purchase of the Satsuma laser a new fabrication line was built for this project (check section 2.1.1). The new laser has a shorter pulse duration than the
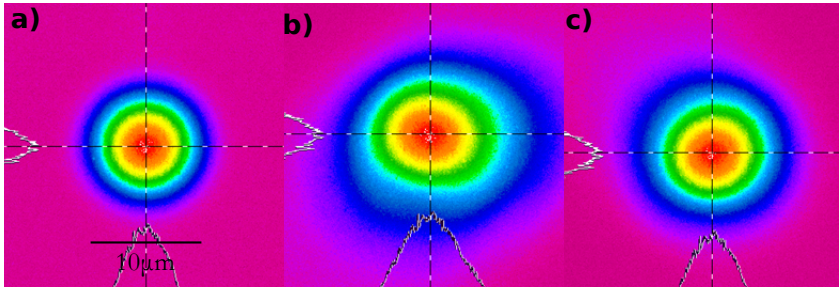
**Figure 3.6:** Fig: Mode profiles of a select waveguide, written with $0.16\mu J$ pulse energy, 8 $\mu m$ helix radius, green wavelength and 1 MHz repetition rate. a) Fibre, b) waveguide mode when collecting from the bottom and c) collecting from the top

previous one which is associated with lower losses in type I waveguides written transversally. Together with a new line a water immersion microscope objective was also purchased in order to reduce the spherical aberrations effects that were still observed in the previous waveguides. No improvement was observed though when writing in these new conditions type I waveguides, so after a few test runs we continued with the type II approach.

**Suspended waveguides**

One interesting result we came across when changing to the new fabrication line was the possibility of fabricating suspended waveguides. In figure 3.7 you can find the profile images that show the three possibilities. By starting before the bottom surface and finish at the top one it was possible to drive ablation all the way through. The pulse energy used here was reasonable for writing waveguides $(0.2\mu J)$.

When observing with the optical microscope it was not obvious that these structures were open. Only when coupling with index-matching oil we observed that the oil flowed inside the structure. When inspecting on the scanning electron microscope (SEM) it became evident that they were opened. Furthermore it was observed they are also not fixed and can move (If you look in the bottom SEM image the waveguide is leaning to the top right corner). We tested polishing down to $15\mu m$ inside the sample they still looked open.

We observed single mode waveguiding at 1550 nm and in some cases these waveguides showed insertion losses as low as 0.2 dB, which was close to the expected coupling loss, meaning the propagation losses were negligible. This is not so surprising since we have an almost complete air gap around the waveguides and the index contrast is on the order of $10^{-1}$ and so the mode would be completely confined inside the glass core.

With the right development this may be an interesting result to explore. If some way is found to anchor the waveguides to the substrate in place by leaving unmodified bits of glass that don't add too much to the insertion losses, it may be possible to achieve almost loss-less vertical waveguides with this technique.
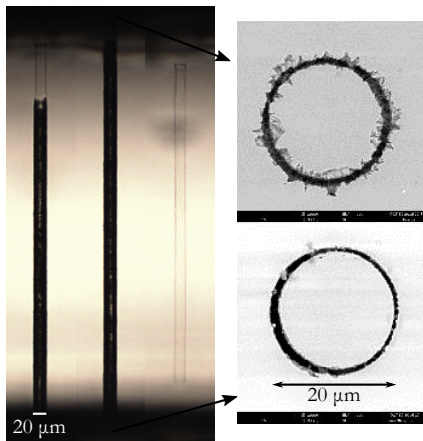
**Figure 3.7:** (left) side-view microscope pictures of the resulting modification of three waveguides with different starting and stopping depth conditions. The first the writing beam started before the bottom surface and finished close to the top. The second one was written all the way through, and the third one is completely embedded in the glass. The black modification corresponds to ablated glass, while the faint line is the laser glass modification. (right) top and bottom profile pictures taken on a scanning electron microscope. Its visible that there is a opening on both ends all around the waveguide.

### Type II waveguides - revisited

After observing the interesting but unreliable results of the suspended waveguides we decided that the best approach would be to try to continue embedding the modification inside the glass but try to drive the nano-void regime instead. A quick review on the literature showed that most results on nano-voids used IR wavelength and a lower repetition rate (1 kHz). So in the subsequent tests we explored this regime, while also increasing the pulse energy ten fold from $\approx 0.1 - 0.2\mu J$ to $\approx 3 - 9\mu J$.

One advantage of writing with 1 kHz is that we could use much higher pulse energy. For the same pulse energy we are using 1000 times less power. In fact a study on mirror damages made by femtosecond lasers found that at 1 kHz repetition rate the energy threshold for damage when compared to 4.3 MHz repetition rate is 3-5 times higher [101]. We also increased slightly the scan speed from $10\mu m/s$ to $25\mu m/s$, which did not provide measurable additional losses and allowed us to decrease the fabrication time per waveguide to about 30 minutes.

We tested increasing pulse energies at 1 kHz repetition rate, and tested different helix radii between $8 - 12\mu m$ and pulse energies from $1 - 9\mu J$. The overall trend on the insertion losses was a small decrease with the increase in pulse energy. With radius we observed again an overall decrease in insertion losses with radius, but from $11\mu m$ we would start seeing a moving mode again, like in the previous experiment.

The best waveguides were found for the highest pulse energy ($9\mu J$) and a helix radius of $10\mu m$. The characterization of the corresponding waveguide can

be seen in figure 3.8.

By taking a close inspection at the microscope side view it is possible to see that at the top there is a darker region. This is evidence that during the helix fabrication there is densification of the surrounding material that is pushed upwards as the helix progresses. We tested just doing shorter helices in the middle of the glass and the same dark accumulation region appears. At the bottom instead we can see the central modification fading in the last tens of microns. This is caused by the length that the laser leaves at each spot (see figure 3.5c). This is particularly visible in the tilted waveguides where you see the vertical modification lines at the end.

By polishing the waveguides and inspecting on the scanning electron microscope we discovered that there is not a real void inside. Some further studies are necessary to help understand what is the nature of the modification that is produced.

The mode sizes are quite smaller than the fibre, particularly in H direction. In fact the estimated coupling losses for these waveguides is around 0.4 dB. So almost half of the insertion losses are due to this effect. The higher insertion losses when collecting from the top can be attributed to the higher distance from the end of our waveguide to the bottom surface, that increases coupling losses away from our estimation. Although we can reach with the end of our waveguide to negligible distances from the surface (see figure 3.15), the guiding region clearly does not start at the tip due to the single spot modification size (see c) in figure 3.5).
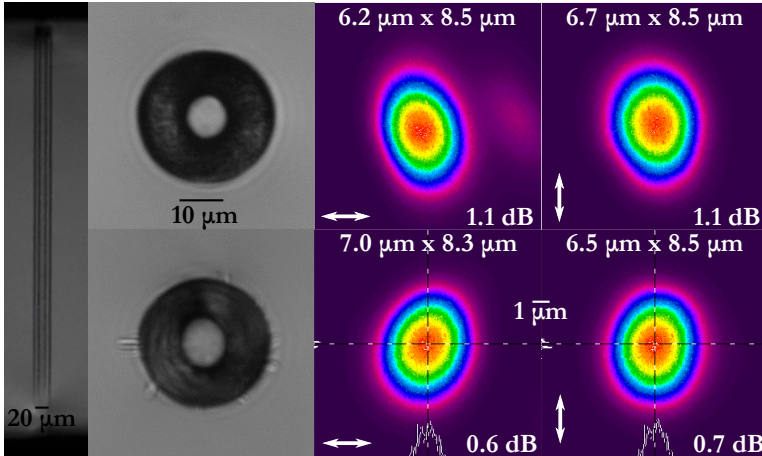


**Figure 3.8:** fs vertical waveguide written with 1 kHz repetition rate, $9\mu J$ pulse energy and IR wavelength. (left) side-view microscope image. The writing laser beam came through the top. (centre) top and bottom microscope pictures of the waveguides profile. (right) Modes recorded at 1550 nm when collecting through the corresponding microscope picture side. The arrows correspond to the direction of the input light polarization during characterization. The numbers on top correspond to the fitted elliptical gaussian mode size. The bottom ones to the insertion loss measured.

When collecting from both ends of the waveguide we observe elliptical modes. Overall the ellipticity for these waveguides was of $0.5 \pm 0.1$. When checking

the fibre mode an ellipticity of 0.21 (which should be 0) was found so this is higher than experimental error. B. McMillen recently made a study of similar cylindrical structures, also fabricated by femtosecond laser just with conditions tailored to the nano-grating regime [102]. They found anisotropic stress pattern in the written ring that followed the nano-grating direction, which is dependent on the writing polarization. In our case the grating orientation would be horizontal and thus the region of higher pressure would be the lateral sides, which can explain the ellipticity. Even though we are using much higher pulse energy it is also true that we are not making pure voids. It is possible that the same mechanism responsible for the creation of nano-gratings still leaves anisotropic stress in our writing conditions.

**Characterization of the modification**

In order to know more about the type of modification that we have in our waveguides, we polished one sample with a waveguide written with $7\mu J$ pulse energy, and polished it until the modified region was exposed. Then we did spatially resolved Raman characterization, collecting spectra both at the outer ring region, and the centre. In figure 3.9 you can see a typical Raman spectra from fused silica [103]. Each of the four $\omega_i$ peaks is associated with vibrational modes of the five-atom tetrahedron that is the basic unit of the network of $SiO_2$. This network is formed of rings that can have different number of elements, and consequentially different angles and molecular vibration frequencies. To the molecular vibration of the four and fivefold ring structures other two sub-peaks are associated, $D_1$ and $D_2$ respectively.

Now back to the experimental results, we observe a movement of the $D_1$ peak to the right, and a general compression of the $\omega_1$ peak. We fitted the position of the $D_1$ peaks and got $487.7 \pm 0.1$ for the pristine glass, and for the modified glass $492.6 \pm 0.5$ in the cladding and $489.6 \pm 0.3$ at the core. These two effects are associated with densification of the fused silica [104]. We also see two more peaks being created around the $D_2$ one. This could be associated with higher order ring formation since it is associated with a broadening of the $D_2$ peak [105].

The main surprise in this results is that in all the difference in the spectra seems to be gradual from the core to the cladding. These are still preliminary results and further analysis needs to be done.

After this analysis we etched the sample in HF acid for a short time and took the image in the scanning electron microscope (SEM) seen in figure 3.9. It is possible to see on the edges of the cylinder ripples that are perpendicular to the writing laser polarization, pointing to nano-grating formation. There is still a ring of glass visible, but it is clearly being attacked by the acid. Another interesting remark is the ellipticity of the central glass, which is further proof that the modification that is left on the glass is asymmetric and might explain their birefringence.

**Birefringence measurements**

We observed that there was some birefringence in our waveguides. In order to do a proper characterization we used the system described in section 2.3.4 to fully
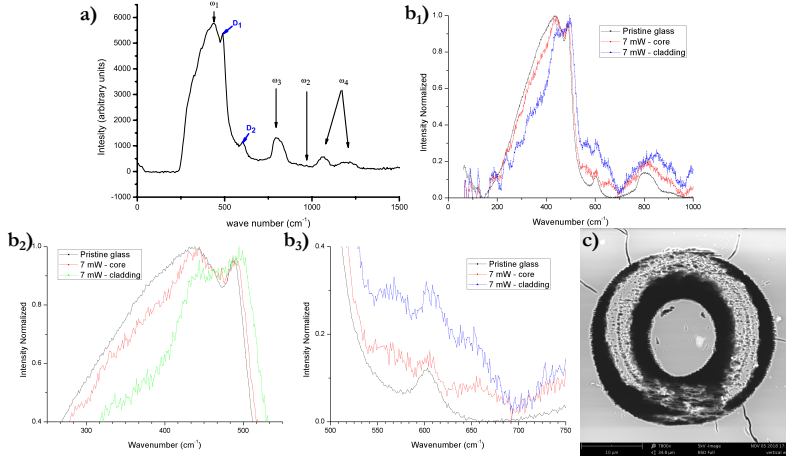
**Figure 3.9:** a) Typical Raman spectra of fused silica, with the main peaks marked (from [103]). $b_1$) Obtained Raman spectra for a waveguide written with $7\mu J$ pulse energy. $b_2$) Zoom-in on the $D_1$ peak zone. $b_3$ Zoom-in on the $D_2$ peak zone. c) SEM waveguide profile image after etching.

measure the Müller matrix of our waveguides. The results can be found in figure 3.10.

We found that the degree of polarization at the output was around 0.67 for all input polarizations except the horizontal and vertical. Apart from the degree of polarization we got a good fit to an uni-axial birefringence matrix, with the fast axis corresponding to the V polarization direction.

All these results point to the existence of some background signal that is collected without coupling inside the waveguide. This would explain why the degree of polarization is close to 1 for H and V input, since the signal that passes through the waveguide will remain unchanged as would the uncoupled light. For all the other cases we have a mix of signals. Since our sample is thin we expect to have some background signal.

We calculated again the model but this time subtracting from the matrix of results the response of a background of 300 $\mu W$ (no rotation of the polarization). For comparison the input power was 3.5 mW. Its possible to see that this correction practically erases the degree of polarization issue, and now the experimental and theoretically modelled points coincide not only in angle but also radially.

Using the recorded modes for H and V polarization and the index estimation method we measured a change in refractive index on the order of $10^{-4}$. The estimated birefringence was $6.9x10^{-4}$ and $6.1 \times 10^{-4}$ depending if we take the background 300 $\mu W$ subtraction or not. We are supposing here a zero order rotation. Our sample is just 675 $\mu m$ thick which means reducing its size is not a easy solution in order to measure the birefringence univocally. In case of a first order rotation the birefringence would be $2.6x10^{-3}$ which would be on the order of magnitude of the refractive index change we estimated for our waveguides. Since we expect that the main mechanism for refractive index change in our waveguides is stress induced, it should have contributions in both axis directions. In any case since the main axis of rotation are coincident with H and V laser polarization

this should not be a problem for the final application, since the device is designed to work with linear polarization.
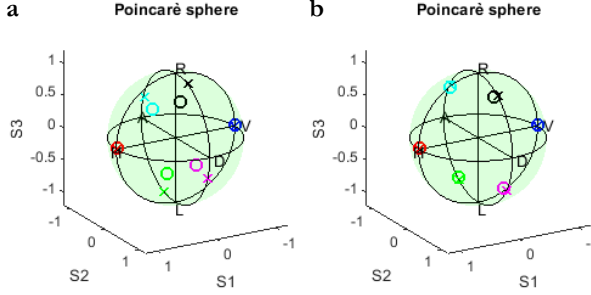


**Figure 3.10:** Resulting Poincaré sphere of the vertical waveguide without (a) and with (b) the background correction. The circles correspond to the measured polarization. The crosses the modelled expected value according to a uni-axial birefringence rotation. Each colour corresponds to a different input polarization: red: H, blue : V, pink: right-handed circular (R),cyan: left-handed circular (L),black- anti-diagonal (A),green- Diagonal (D).

**Annealing**

In order to reduce the propagation losses a common solution is to test a thermal treatment. Particularly, since we are using such high pulse energies the damage induced can create irregularities that act as scattering centres, which could be smoothed out by annealing. There are several studies of annealing in fused silica. A temperature of $600°C$ to $800°C$ was found to fade direct written type I waveguides [106]. With $900°C$ they observed complete erase of the waveguides, but retaining the damaged regions. Another study managed to reduce roughness by annealing at $1300°C$ for just one hour, with better results than chemical treatments[107].

The first two tests were done with two plateaus, stopping at $300°C$ for 1 hour, and then heated up again until it reached either $600°C$ or $900°C$, staying there for 10 h. The heating rate was always $300°C/h$ which is standard for avoiding thermal shocks. In these two experiments no visible change both in the profile of the waveguide and in the insertion losses was observed. The last test done was at $1200°C$ for 5 hours, which is past the annealing ($1150°C$) and strain ($1120°C$) points of the glass. This sample showed a big increase in insertion losses to 3 dB.

It is possible that at some intermediate temperature between $900 - 1200°C$ we can find some improvement on the insertion losses, but we did not pursue this question further yet. Also, since these waveguides are going to be integrated with other components and this kind of treatment may damage them, and thus either being forbidden or simply forcing a longer fabrication procedure.

On a more positive note these tests can be seen as evidence of the strong thermal resistance of waveguides written with this method. Type I waveguides typically show changes even when annealing at $400°C$ [108].

**Tilting waveguides**

After successfully writing low-loss vertical waveguides, the next step was to characterize how do they work if we tilt them. So we fabricated a sample with waveguides written at different angles from 0° to 9°. Two other waveguides tested the curving, by changing continuously from 3° to 6° and from 3° to 9°. We also tested fabricating with linear and circular polarization. For having circular polarization we simply added a quarter wave-plate before the microscope objective at 45° with respect to the laser polarization. The writing conditions for all waveguides were the same as before.

After fabrication the sample was again characterized in terms of losses and mode size using the setup described in section 2.3.3. In figure 3.11 you can find a summary of the results. It is possible to see that for linear polarization the losses increase less than 0.5 dB for up to 6° tilt. For the waveguides written with circular polarization, even though the mode sizes were closer to the fibre (small coupling losses overall) the sensitivity of the insertion losses to angle change was much higher, with the last waveguide having more than 4 dB loss for both polarizations. This effect might be explained from
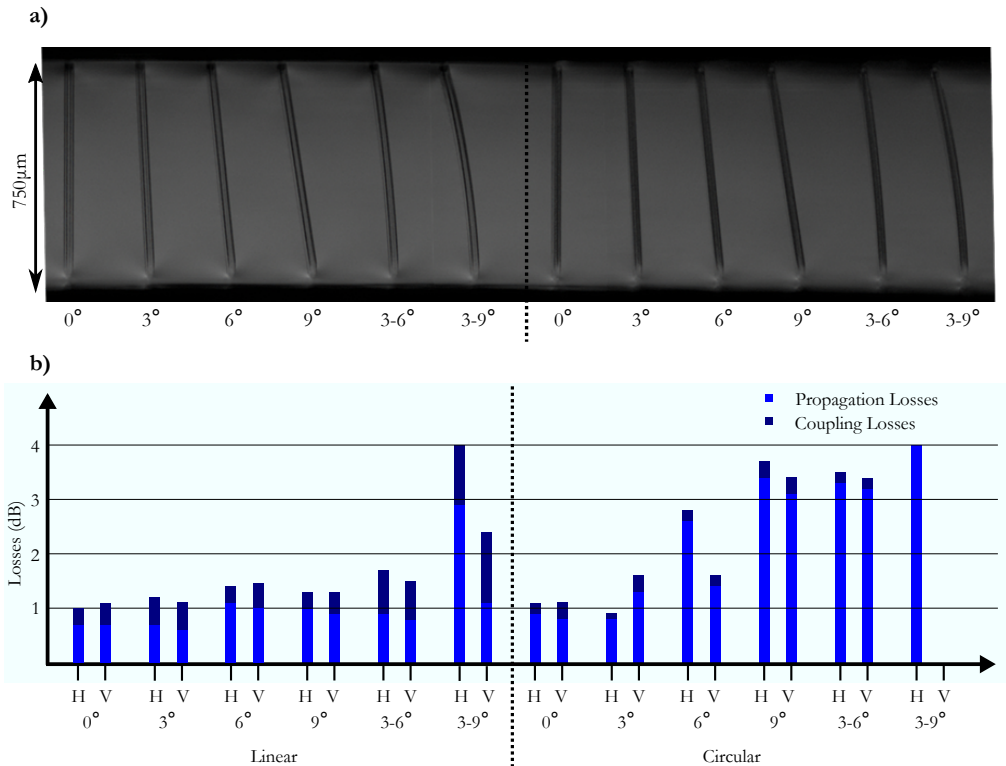


**Figure 3.11:** a) Profile picture of the direct written waveguides, with different tilting angles from left to right. The last two in each set start at the bottom with 3° tilt and gradually curve to 6° and 9°, respectively. The polarization of the writing laser in the linear case was perpendicular to the page. b) Insertion losses of the waveguides, divided in propagation and coupling losses.

Going back to the B. McMillen paper [102], something else they found is that also for circular polarization we have this anisotropy in the stress pattern. The only way they managed to create a uniform stress pattern was when fabricating either with radial or azimuthal polarization, that are exotic polarisation states that change within the spacial distribution of the beam. Knowing about this we bought a special waveplate (s-waveplate Altechna) that can convert from linear polarization into radial or azimuthal. The main limitation of using such polarization is the losses of the component which limited the maximum pulse energy that we could use. In practice this meant that the waveguides written with this method all had more than 2 dB loss.

## 3.3 Waveguide integration in chips for interconnection

After proving the capabilities of these waveguides we moved into integrating them with the channel waveguides for the final interposer.

**Planar channel waveguides**

The planar channel waveguides are fabricated on top of the silica substrate, as can be seen in figure 3.12. They are made of $Ge : SiO_2$, and the core is created by plasma enhanced chemical vapour deposition followed by a standard photo-lithographic process. The core thickness is $4.7\mu m$. These waveguides provide very low propagation loss of 0.03 dB/cm and the propagated mode was tailored to be the same as the SMF-28 fibre @1550 nm ($10.4\mu m$). This part of the fabrication process is done by our colleagues at CNIT institute.
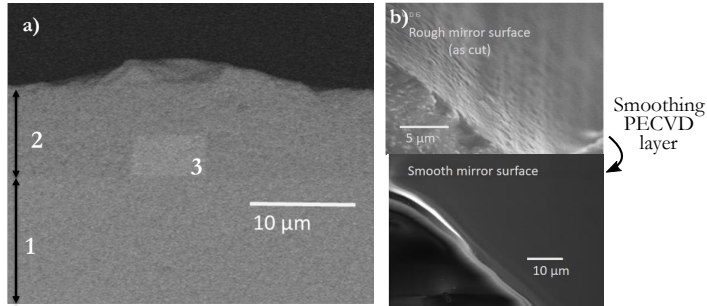


**Figure 3.12:** a) SEM image of the channel waveguide profile. legend: 1-fused silica sample 2-bpTEOS cladding layer 3-$Ge : SiO_2$ core b) mirror SEM images just after cutting, and after the PECVD treatment. (from [109])

**Steering mirror**

The mirror is currently fabricated by using the dicing blade that is used to cut chips into pieces, and making a small incision instead. The roughness is smoothed out by plasma enhanced chemical vapour deposition (PECVD) treatment. You can see in figure 3.12 a lateral view that shows this surface smoothness difference. A colleague from our group is doing some exploratory experiments, and having some good preliminary results, on fabricating the mirrors by two photon polymerisation guided by direct fs laser writing. This method would have the big advantage of being able to fabricate mirrors in any place on the sample, and with even more control on the geometry since we can make arbitrary angle. Currently using the dicing method means a whole line in the chip needs to be carved, instead of local mirrors.

## Further optimization of the fs waveguides

In the new samples with the bp-TEOS layer at the bottom we tested a fine tune of both the pulse energy between 5-9 $\mu J$ and helix radius from $10 - 11\mu m$. The optimal parameters were found to be $10.5\mu m$ radius and $7\mu J$ pulse duration. The insertion losses of the waveguides can vary between fabrications and characterization, but with this late improvement we consistently achieved lower than 1 dB insertion losses coupling from both sides. The new modes can be seen in figure 3.13. Using the method described in section 2.3 we estimated the refractive index profile. The noise smoothing was done until the multiple noise peaks were smoothed out. The peak refractive index change for the mode collected at the bottom and top were $\Delta n = 8.8 \times 10^{-3}$ and $\Delta n = 1.3 \times 10^{-2}$ respectively. The varying mode size and refractive index change points to the existence of some spherical aberration effect still. It is also possible that this change in mode diameter is associated with the new layer for the planar waveguides that the sample has at the bottom, since we did not see it before. This is acceptable though since at these mode sizes the increase in coupling losses is not drastic.
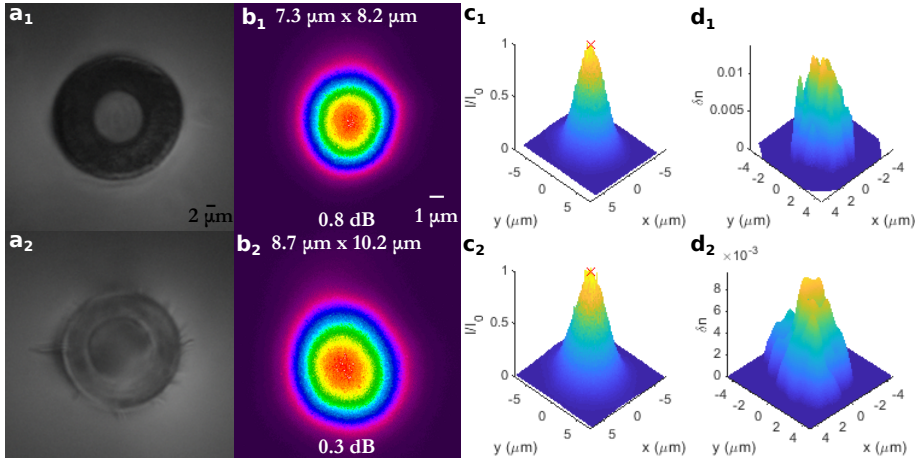


**Figure 3.13:** Results from a fs vertical waveguide written with 1 kHz repetition rate. a) Top and bottom microscope pictures of the waveguides profile. b) Mode recorded at 1550 nm when collecting through the corresponding microscope picture. The numbers on top correspond to the fitted elliptical gaussian mode size. The bottom ones to the insertion losses measured. d) Estimated refractive index profile from the mode profile c). We used a uniform filter of 8 pixels range for 10 times for $d_1$ and 7 pixels applied 7 times for $d_2$.

To test for the reproducibility of the losses of these waveguides we fabricated 9 waveguides with exactly the same fabrication conditions. The pulse energy was the optimal at $7\mu J$ but they were tilted by 6.2°. We coupled with both H and V polarization and found a standard deviation of 0.2 dB for both polarizations with an average of 1.2 and 1.4 for H and V respectively. Again a small polarization dependent loss was observed.

**Alignment method**

The alignment of the fs waveguides with the channel ones is achieved using markers that are created during the planar channel waveguide fabrication. Such markers can be seen in figure 3.14. Regardless if the markers are metallized or not, we can still detect them using the writing laser itself. After making all the alignment procedure to align the tilt of the sample, we bring the focus to the respective surface. Here the machine vision system helps find a coarse alignment and get the laser focus close to the markers positions. Since the imaging system is not perfectly aligned we have about $10\mu m$ shift from the image to the real spot position, so here we turn off the machine vision and move in small steps the focused laser until we see the back-reflected spot at the ccd camera starting to fade (or shine brighter in case of a metallized marker). This fading position has some uncertainty so in order to reduce the error we take multiple measurements.

For the square markers we take four measurements, one at each of the sides. We try to be as close as possible to the middle of each side of the square, and this can be easily seen by just making a quick scan before doing the measurement: just two square markers are enough for knowing the position of all the waveguides, and also calculate the angle that they form compared to the xy stages axis.

Alternatively we also tested using the markers on top of the sample. In this case we measure two markers that are aligned with the mirror at the bottom, and then two more for each waveguide. Here we just take two measurements for each marker, with each two markers forming a line: the first two form a line perpendicular to the channel waveguides and the next two cross it finding the right position for the end of our waveguide. This method has the advantage of removing some systematic error of using the squares that mean all waveguides share the same error. We estimate the error of both types of alignment to be within $1\mu m$.

Having now fixed a xy position either at the bottom or at the top of the sample, we need to compute the actual path of the waveguide. Here some subtleties need to be taken into account. Apart from correcting for the refractive index effects analysed in section 2.1.2, there are some more complications in this case. First, we need to have different waveguide angles at the bottom and top. So the waveguide needs to be curved. Then we also need the waveguide to both start and finish at some specific point. This means we have four constrains that need to be verified in our curve. Now if we want to draw a simple circle, these are too many constrains, since it is defined by only three. Our solution in the end was to use a polynomial fit. This is not the best solution since the overall curvature is not uniform but for most cases it resulted in a smooth curve. Finally, there is the detail that we actually don't finish the waveguide exactly at the bottom of the sample or top. So we need to actually project with the right angle the measured point from the surface to the estimated depth at which our waveguide starts or finishes. This is typically a smaller error, within $1-2\mu m$ but in this kind of alignment can be crucial. A scheme of this whole alignment method can be found in figure 3.14
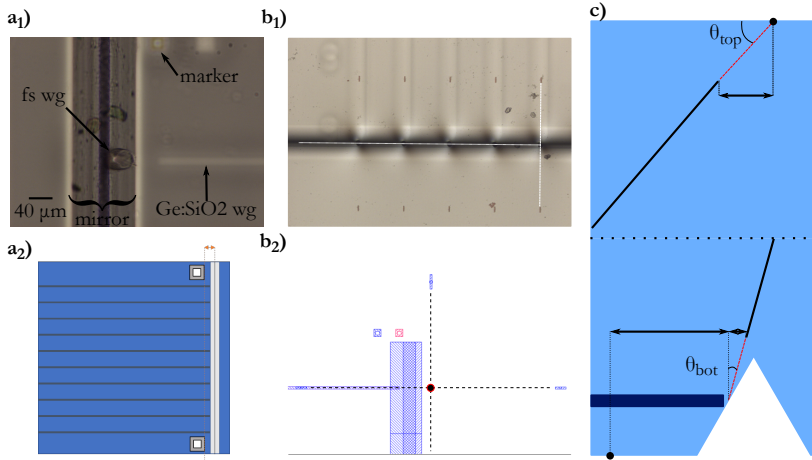
**Figure 3.14:** Scheme of the fabrication alignment.a) Bottom square markers alignment. b) Top markers alignment: microscope image $b_1$) and schematic $b_2$) c) position alignment corrections due to real ending position of the waveguide.

### Depth calibration

Throughout our fabrications we continuously tried to master the correct depth positioning in order to finish our waveguides as close as possible to the surface. In figure 3.15 you can find some of the best results on the proximity of the tip of the waveguide to the surfaces and mirror edge. We manage to write consistently within less than $5\mu m$ from each surface. During long fabrications we see a shift of this positioning on the order of $1\mu m$ every 2 hours. This could be attributed not necessarily only to thermal shifts but also some drift on the z stage. Since it works under constant air pressure to counter the weight it shows less accuracy than the xy ones. So whenever we fabricate during longer times we recalibrate the depth every hour. In this way when fabricating a set of waveguides in sequence we can retain $1\mu m$ reproducibility.

### Integration with PLC waveguides

After fabricating the fs waveguides aligned with the channel waveguides and mirror, we characterized the sample by using a similar setup as for characterizing waveguides (see 2.3.2) only this time we coupled laterally through the channel waveguides, collecting at 90° at the fs waveguide output. In figure 3.16 you can see a summary of the results obtained. It is possible to see the spot at the top of the sample when we have our waveguide. The dark region that surrounds the waveguide written position at the bottom was made due to ablation of the metallic coating of the mirror. It did not affect the glass underneath in any way however. This was probably due to the shock-wave that is created during high pulse energy absorption, and since the metallic layer was just deposited by evaporation it does not have a a strong bond with the glass. Even without the metallic layer the mirror worked since it had higher than critical angle (which
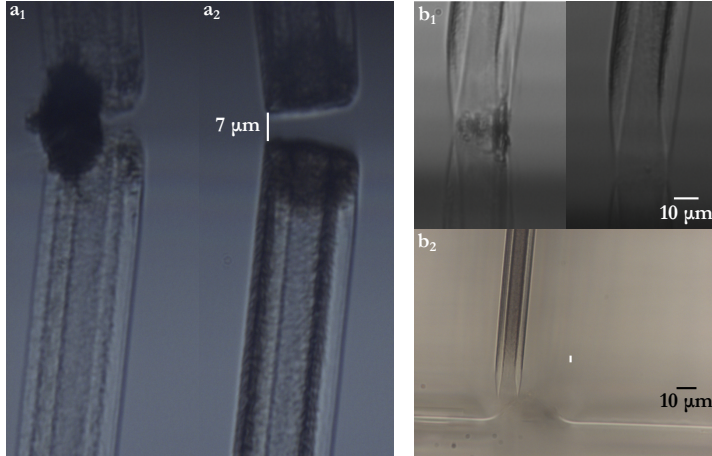
**Figure 3.15:** side-view images on tests of both top (a) and bottom (b) limits of the waveguide fabrication. The smaller images are a reflection that is formed on the microscope. From $a_1$ to $a_2$ there was a $1\mu m$ shift of the final point on the z stage. On $b$ we have the bottom limits found both for the normal facet $b_1$ and in the case of alignment with the mirror ($b_2$).

is $43.8°$). The lowest total insertion losses found for the whole system: channel
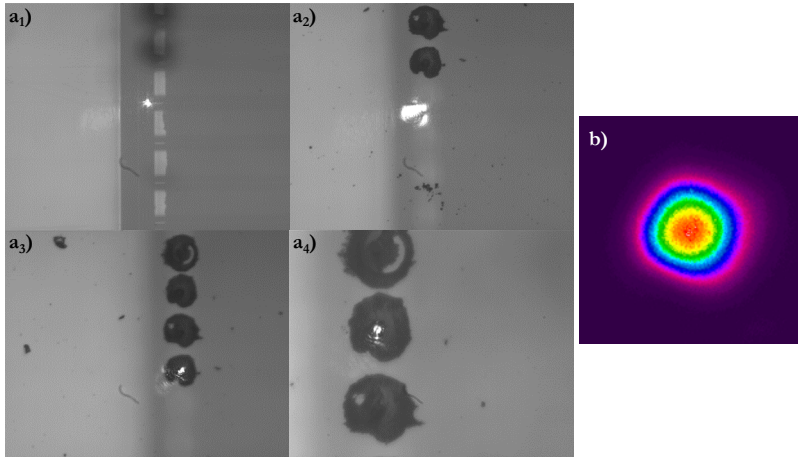


**Figure 3.16:** Collection of the output signal on the mirror side after coupling through the channel waveguides. a) red wavelength coupling images. Coupling through a region without ($a_1$) and $a_2$)) and with ($a_3$) and $a_4$)) a vertical waveguide, and focusing the imaging objective at the mirror position ($a_1$) and $a_3$)) and at the top of the sample ($a_2$ and $a_4$)).

waveguide, mirror and fs waveguide were 1.8 dB. This is a great result given that the losses just from our waveguide were around 1 dB depending on the tilt applied. The rest 0.8 dB are distributed from the channel waveguide, coupling losses from the fibre to the channel waveguide and between the channel waveguide and the fs waveguide. This last one can vary greatly with the total distance that light needs

to propagate from the end of the waveguide until the start of our waveguide. If we make some quick calculations on the divergence after the waveguide we can see that in just $20\mu m$ the mode size can increase by $4\mu m$ in diameter which corresponds to about 0.5 dB increased coupling losses. Due to the geometry of our waveguide we have at least $10\mu m$ distance from the centre of the waveguide to the edge of the mirror.

**Piling of waveguides**

The next proof of principle we needed to make was the ability to pile more than one sample and send the signal from a fs waveguide to another one written in the second sample. In order to do that, we wrote waveguides on a region of a sample that was clear of any channel waveguides and wrote as close as possible to the bottom. We then mounted everything in the setup described in figure 3.17, where one can find the output modes observed. We first collected the mode
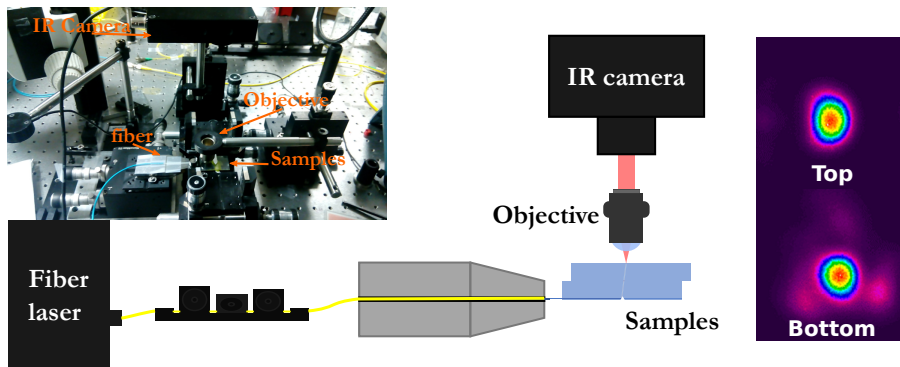


**Figure 3.17:** Scheme of the setup present in the picture on top left. The two samples are mounted each on a micro-metric stage, as well the fiber mount. The output is collected vertically by the objective and projected on the IR camera. Right: modes collected when coupling with 1550 nm wavelength and focusing at the output of the first sample (bottom), and after aligning the second waveguide with the first from that higher output (top).

from the bottom sample, and then slid the second one until coupling. At that point we managed to measure the top mode too. We could only collect $220\mu W$ from 6 mW at the input. The coupling during this experiment was not the best, due to the difficulty in the mounting of the experimental apparatus, particularly adapting the tilt of both samples and bringing the surfaces close together since they are reasonably large (6x2 cm). The other possibility is that the losses come from the sum of the gaps that the two fs waveguides have at the bottom and top, but we have seen that we manage to fabricate within a few microns from each surface and in the previous experiment we did not see this level of coupling losses. A proper bounding of the samples for the project will be done by the Universitat Politecnica De Valencia group that collaborates in this project.

## 3.4   Outlook

In conclusion, we managed to fabricated single mode waveguides with both low loss and with birefringence axis aligned with the main axis of the waveguide. We also managed to integrate successfully the vertical waveguides with the planar channel waveguides, achieving a 1.8 dB insertion loss for the whole system. Finally we made a proof of concept of stacking samples which is crucial for the objective of having higher density of connections in the same area. In the future we will continue to provide vertical waveguides for this project and collaborate in the fabrication of the prototypes needed.

# Chapter 4

# Fabry-Pérot Brewster windows for polarization filtering

In this chapter we will explore the fabrication of embedded polarisers in glass by using the FLICE technique. We will start with a basic motivation for this research, and then some theoretical basis that was used to characterize the behaviour of our windows. We will then present the results we obtained, and make a quick analysis providing suggestions on the way forward. This work was performed in collaboration with the group of Professor Peter Herman at the University of Toronto where I spent 5 months as a visiting student in the last year of my PhD.

## 4.1 Motivation

Polarisers with arbitrarily high polarization rate are easily available in the market. Wire grid polarisers provide extinction ratios of up to 10000 at infra-red, dropping down to 100 at ultra-violet wavelengths. Polarizing beam-splitters have a bandwidth response, but can have 10000 at any specific wavelength from 405-1550 nm. Film polarisers can also provide higher than 10000 polarization ratio within a 10 nm bandwidth.

However, when it comes to embed a polariser inside glass, it is not as easy. All the solutions mentioned before are either bulky or based on deposition which has problems being applied inside glass. There are some solutions in literature, such as creating an opening and attaching close to the core a layer of PMMA and graphene [110], which provides a very high polarization ratio (36 dB) but with some insertion loss (5 dB). Or by using 45° tilted Bragg gratings UV inscribed in hydrogenated Ge-doped fibre [111]. What is common in both these solutions is that they are quite specific in their application.

Most commonly polarization control on a fibre can be achieved by inducing stress birefringence, and this is how in-line polarisers work. But since this control is external, in the case of a multi-core fibre we could not use it to control each single output polarization. The ultimate objective of this project is to embed a polarizing element inside a fibre, in order to possibly have different polarizations at different outputs of the fibre. In order to test these devices we first planned proving their capability inside rectangular fused silica glass samples, since they are easier to characterize.

Direct fabrication in an optical fibre has been already demonstrated before [112] [113], and by using an oil immersion lens we can reduce the lensing effect that is created by the fibre shape. So the possibility to translate these devices to a fibre environment should be relatively easy after proving them in the rectangular samples.

One last example worth mentioning is a work made by M. Haque et al [114], in which micro-resonators were fabricated too with the FLICE technique. In this case the objective was not to have polarization effects, but still the geometry is similar to what we are creating. The chamber dimensions were bigger $(7-10\mu m)$, which means that the bandwidth of the resonance was on the order of tens of microns. Still with only 2 resonators they managed higher than 30 dB contrast in reflection. In our case we are working with few micron sized structures and thus we can potentially have larger bandwidths.

## 4.2 Theoretical Analysis

Let us consider a set of windows in series, that are air holes embedded in glass, and tilted at a fixed angle. In figure 4.1, you can find a scheme of the ray paths that happen inside such system. Depending on the dimensions of the different specifications it can be possible to have interference between the different rays in the system.
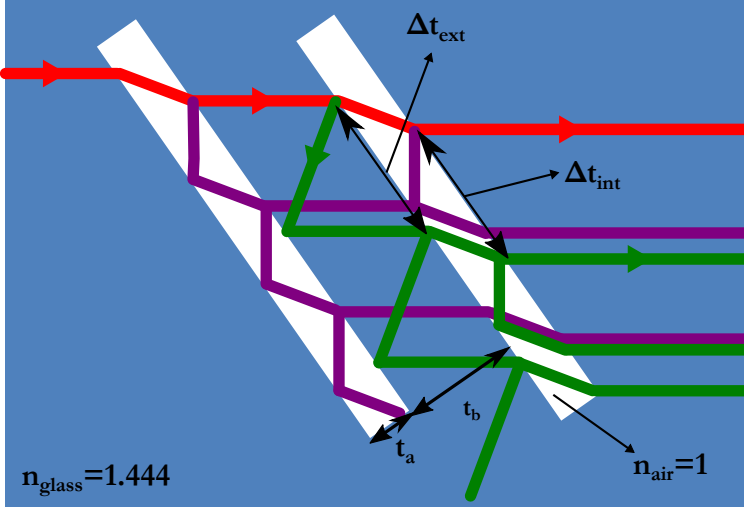


**Figure 4.1:** Scheme of the projected device, with the discrimination of three types of rays generated. In red the simple transmission only ray path. In purple the rays generated in the multiple reflections inside the air gap. In green the reflections generated in the glass gap between windows.

### 4.2.1 Brewster window

The first approach consists in considering each of these windows independent and also neglect any interference effects on the system. In this case, we will have that the transmission of a system of N windows will be equal to $PR_N = PR_1{}^n$. The polarization ratio from each window will be given by $PR_1 = \left(\frac{T_P}{T_S}\right)^2$ with $T_{S/P} = 1 - |r_{S/P}|^2$ and:

$$r_S = \frac{\sin(\theta_i - \theta_t)}{\sin(\theta_i + \theta_t)} \quad ; \quad r_P = \frac{\tan(\theta_i - \theta_t)}{\tan(\theta_i + \theta_t)} \tag{4.1}$$

with the Snell relationship $n_{glass}\sin\theta_i = n_{air}\sin\theta_t$ observed. Considering an air gap, we have that the Brewster angle is $\theta_B = 34.7°$ With this relationship we can calculate the polarization ratio dependence on the angle. In figure 4.2 you can find a plot of this relationship. As expected at Brewster angle we have zero losses on the P component of polarization and 1.3 polarisation ratio per window, and thus theoretically in this condition we can have an arbitrarily high polarization ratio by just adding enough windows. Since the progression is geometric it quickly increases with each window added.
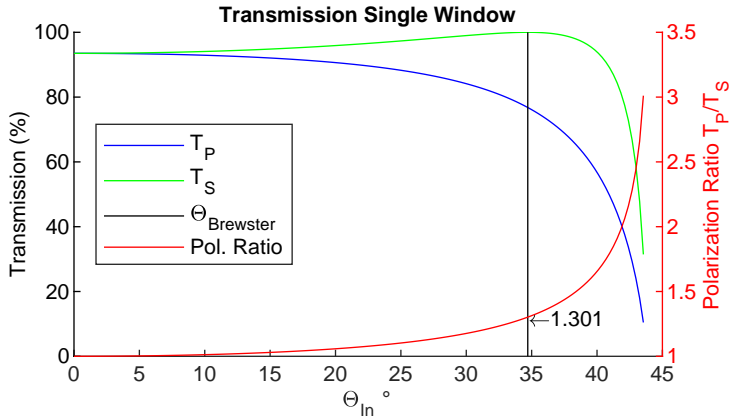
**Figure 4.2:** Transmission dependence on angle for a single window taking only Fresnel reflexions into account. The red line shows the corresponding polarization ratio of such window with a mark at Brewster angle.

In figure 4.3 you can find a graph that portraits what is the expected transmission when we have enough windows to arrive at a given polarization ratio threshold. Again at Brewster angle we should have always 0% losses in the ideal case. One interesting aspect that we can observe, is that if we consider a certain loss per window that is independent from the angle (due to roughness or other sources), we see that the optimal tilting angle of these windows shifts to higher degrees. In this example with 3% losses per window we would have an optimal angle of 36.3°.
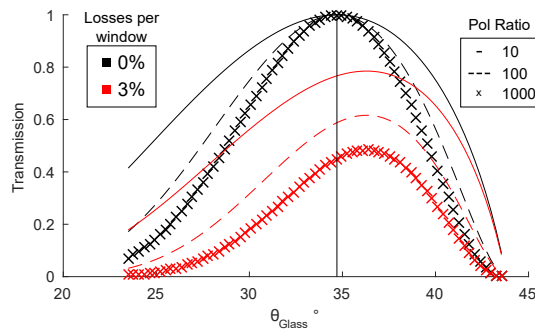


**Figure 4.3:** Calculated transmission of the number of windows necessary for achieving a given polarization ratio (10/100/1000), and plotted vs angle. The same calculations are repeated in red supposing an additional angle independent loss of 3% per window.

### 4.2.2 Fabry-Pérot

After observing that we were obtaining polarization ratios above what is expected by simple Fresnel reflections, we went back to theory and considered the possibility of having Fabry-Pérot interference inside it. Here follows the two main approaches used.

**Independent windows**

The next step is to still consider each window as independent but take into account that there is interference between the rays that reflect inside the air cavity. Thus again the response of the whole system will have the same response $PR_N = PR_1{}^n$, but this time the $PR_1$ will be the response of a Fabry-Pérot at angle $\theta_i$:

$$T = \frac{1}{1 + F \sin^2\left(nk_0 l \cos\theta_t\right)} \tag{4.2}$$

where $k_0 = \frac{2\pi}{\lambda_0}$ and $F = \frac{4R}{(1-R)^2}$ is the finesse of the system. Take into account that both the finesse and the sin factor change with angle. Also, whereas before the response was essentially wavelength independent (apart from a slow change of refractive index with wavelength) now the response is modulated. This modulations period is called the free spectral range (FSR) and is given by $\Delta\lambda = \frac{\lambda_0{}^2}{2nl \cos\theta}$ in wavelength. Note that in wavelength this is not a harmonic modulation, since the period changes with wavelength too. FSR is an important benchmark for knowing if we expect to see interference modulation or not. If we consider a window size of $1\mu m$ the free spectral range is $1.4\mu m @ 1.5\mu m$ so we can expect all sources to show this behaviour. Now if we look at the sample itself (1 mm thickness) as a Fabry-Pérot the FSR is 2.5 nm, which explains why the first tunable laser we tried to measure polarization ratio with had instability on the signal.

In order to have destructive interference the thickness of the chamber needs to be tuned to the resonance condition:

$$t_a \cos\theta_t = i\frac{\lambda_0}{n}, i \in \mathbb{N} \tag{4.3}$$

In figure 4.4 we can find the simulation of this model for realistic values of the air gap thickness. Depending on the window size and the angle we have transmission that oscillates between a minimum that is given by $T_{min} = \frac{1}{1+F}$. Thus it depends only on the finesse of the system, which is only dependent on the input angle. So if we have the right air gap size we can get an enhancement from the previous calculated polarization ratio, from 1.3 up to 1.6 at Brewster angle. The last thing to highlight is that the instability of the polarization ratio to errors of alignment increases with the increase of the thickness. This is related to the FSR, although in this case translated into angle dependence.

**Full resonance**

Finally, we can take into account also the interference between rays that cross back and forth on the multiple windows. In this case we need to use a bit more complex model [115].
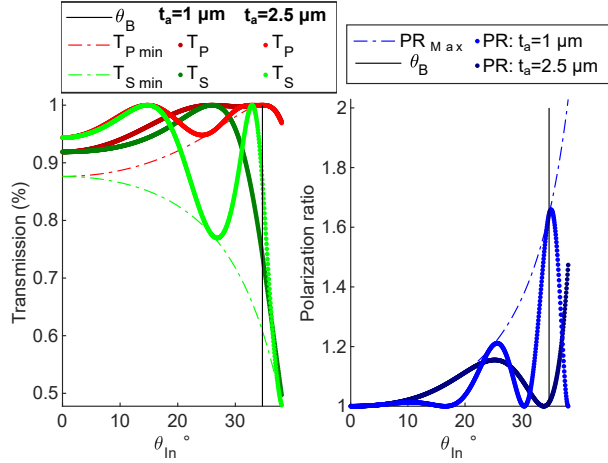
**Figure 4.4:** Modelling of single Fabry Perot windows with air gaps of $1\mu m$ and $2.5\mu m$. Left: Transmission with angle, separated for both P and S pol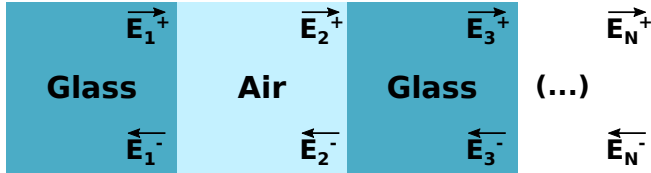arizations. Dashed line corresponds to the minimum that each polarization can arrive to independent on the window size. Right: Polarization ratio calculated from the graph on the left. Again dashed line corresponds to the best polarization ratio that can be achieved at a given angle.



**Figure 4.5:** Full resonance model scheme

We start by using an array notation in which we represent the forward $E^+$ and backward $E^-$ wave as a complex vector. $\vec{E}_i = \begin{bmatrix} E_i^+ E_i^- \end{bmatrix}$. Being a complex number is important here since it means it also carries the phase of the wave and thus interference effects are considered. Using the Fresnel refraction relationship and propagation we can calculate the terms that relate the propagation of the field at each region $\vec{E}_{i+1} = M_{i,i+1}\vec{E}_i$. and calculate the matrix $M = \begin{bmatrix} a & bc & d \end{bmatrix} = \prod_1^{N-1} M_{i,i+1}$ such that:

$$\begin{bmatrix} E_N^+ E_N^- \end{bmatrix} = \begin{bmatrix} a & bc & d \end{bmatrix} \begin{bmatrix} E_1^+ E_1^- \end{bmatrix} \tag{4.4}$$

In order to calculate the output $E_N^+$ with respect to a given input $E_1^+$, using equation 4.4 we can evaluate it under the real constriction $E_N^- = 0$ and we arrive at:

$$E_N^+ = \left( a - \frac{bc}{d} \right) E_1^+ \tag{4.5}$$

The values for $M_{i,i+1}$ matrices are of course dependent on polarization, and thus this means that the we will have $E_N^+$ different depending on polarization.

In this case we have two independent resonance conditions: the same as in the previous analysis for the air gap plus the condition at the glass interface:

$$t_g \cos \theta_i = i\frac{\lambda_0}{n}, i \in \mathbb{N} \tag{4.6}$$

**Limitations**

All this analysis up to now was supposing an ideal case of plane waves that propagate ideally. Actually in our case we have both a laser beam and windows of finite dimensions. Since these are always micrometer sized devices and we are dealing with laser light, coherence is not an issue here. Looking closely to figure 4.1 and with some basic trigonometry we can see that $\Delta t_{int} = \dfrac{2t_a}{\sqrt{\left(\frac{n_2}{n_1 \sin \theta_i}\right)^2 - 1}}$
and $\Delta t_{ext} = 2t_b \tan \theta_i$. So one of the first criteria we can use is counting the number of reflections that happen before the light goes out of the window.
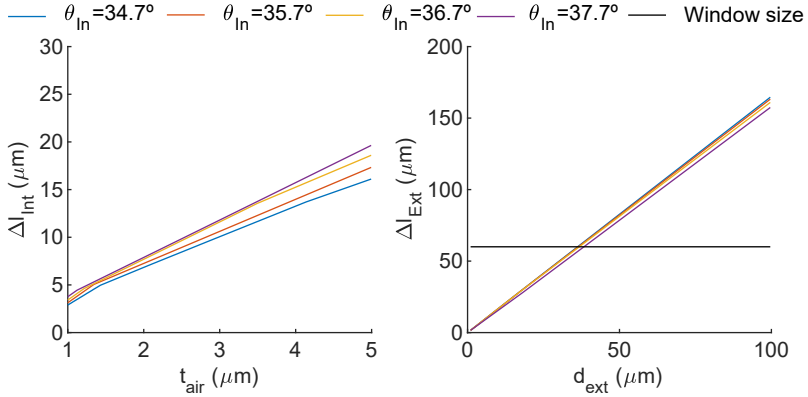


**Figure 4.6:** Lateral shift dependence on the thickness of the air chamber(left) and distance between windows (right)

We can see in figure 4.6 the lateral shift that is accumulated in each round trip. Our windows thickness is between $1 - 5\mu m$, with lateral size fixed at $60\mu m$ and we can see that the lateral shift is enough to have multiple round-trips. Since our windows have low reflectivity, only a few reflections can carry enough power to influence the output. In fact after a single round-trip the power is already below $e^{-2}$. At the glass gap the number of reflections depends on the distance between each window, which can easily be tuned experimentally.

The last comment is that there are also expected distortion effects on the Gaussian shape of the output due to the finite dimension of the laser beam [116], and thus the lower the size and number of interference gaps the better.

**Noise analysis**

In order to simulate the effect of etching uncertainty on the polarization ratio observed, we calculated the polarisation ratio spectra for devices with an uniform

random error in the different dimensions. The effect on the expected spectra of a 5 window tuned for resonance at 1550 nm are plotted in figure 4.7. We can see that we have a very quick change from a negligible effect at 100 nm to a complete erasure of the modulation with a 300 nm error. We did the same for angle errors. Again we found the same dynamic, with the threshold being 0.1°.
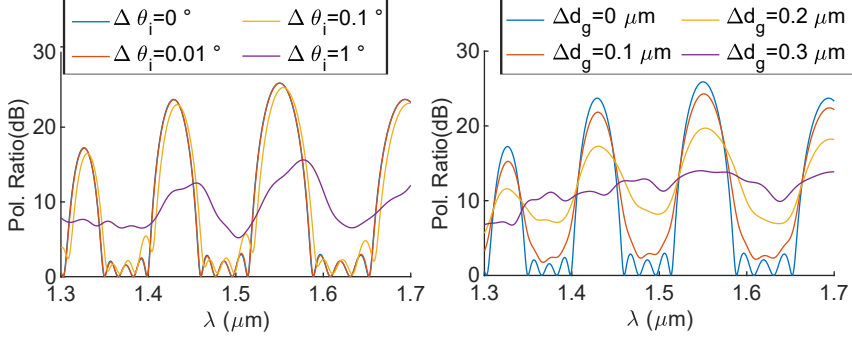


**Figure 4.7:** Simulation of random errors in angle (left) and size of the gaps (right) on a set of 5 windows with base air gaps of $2.0\mu m$ and glass gaps of $6.9\mu m$

### 4.2.3 Final remarks

As can be seen in figure 4.8 there are some promising features in trying to tune this interference mechanism. For the same polarization ratio a reduced number of windows are necessary. For example if we want 100 polarisation ratio we can reduce from 18 windows in the basic model to 10 or 5 if we tune the dimensions of both air and glass gaps. Considering also the limitations from having diverging beam, if we increase the number of windows we are also inevitably increasing the optical path and consequentially the beam size. A nice side effect is the compactness of a lower number of windows that will ease it is fitting in any application.
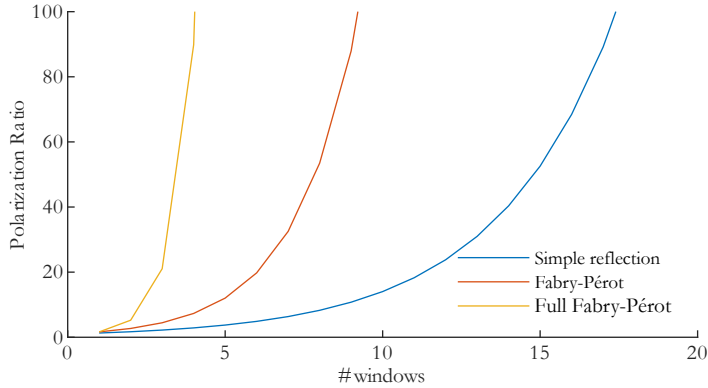
**Figure 4.8:** Comparison of the evolution of maximum polarization ratio for each of the models studied.

## 4.3    Experimental

The fabrication setup used was the fibre laser line described in section 2.1.1. The samples used were pure fused silica with dimensions 0.5"x2"x1mm, from PG&O. Instead of writing through the larger surface, we fixed the sample with magnets on its smaller edge (2mm). We used an oil immersion objective (1.25 NA) that at the same time avoids any possible edge effects, but more importantly is the same focusing conditions that would be used when moving for writing in fibre. Throughout all the experiments we used the green wavelength (515 nm) and 500 kHz repetition rate, and we always tilted the polariser orthogonally to the windows surface, which as seen in the background section provides both faster etching and lower roughness.

In order to achieve an uniform chamber, we scan the wanted area with lines that fill the whole area. In order to avoid any writing errors due to oscillations of the translation stages we start the movement of the stage before the actual writing position, turning the shutter on only when we are in the correct region. The program for writing these windows is done such that all the modifications at the same depth level are done at the same time, in order to avoid any passing of the laser through already modified glass which could increase aberrations and distortions on the pattern fabricated.

After the laser irradiation, the samples were observed under the microscope to check for imperfections or possible errors. Once checked, we start the etching process, in which we used a system similar to the one shown in section 2.2. More specifically we used 5% V/V concentration of HF at room temperature, and we did not do any ultrasound bath since it could create cracks on our windows due to their small size. In this process we typically did many steps of etching interposed with cleaning and observation on the microscope so we could finely control when the etching was completed. Its important not to leave the sample too long in acid since, after etching the modified glass, it also etches the unmodified fused silica, even if at a slower rate, and when this happens the surface roughness increases. Characterization of the windows was done using the setup described in section
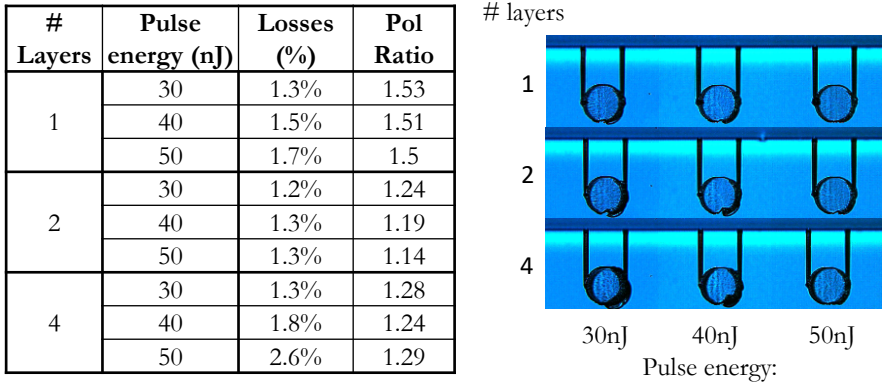
### 4.3.1 Single windows

We started by fabricating single windows with variable laser parameters, in order to optimize the polarization ratio per window. First we tested changing the number of layers that we write on the sample. This will change the thickness of the windows. The results on the polarization ratio can be seen in figure 4.9.

The first conclusion we took from this experiment is that the optimal pulse energy seems to be 30 nJ. Above this value the effect was not dramatic but there was worse performance in all devices. Furthermore, increasing the number of layers only increased the losses and didn't provide any gain in polarization ratio. The increase in losses can be due to increased roughness due to the stacking of modification by the multiple passages.

Focusing now on the single layered device, if we look to the expected polarization ratio from Fresnel equations we actually observed higher than theory polarization ratio. This means that some other mechanism must be at play in this case, and the possibility that we raised was that it is working as a Fabry-Pérot cavity.

| #<br>Layers | Pulse<br>energy (nJ) | Losses<br>(%) | Pol<br>Ratio |
|:---:|:---:|:---:|:---:|
| | 30 | 1.3% | 1.53 |
| 1 | 40 | 1.5% | 1.51 |
| | 50 | 1.7% | 1.5 |
| | 30 | 1.2% | 1.24 |
| 2 | 40 | 1.3% | 1.19 |
| | 50 | 1.3% | 1.14 |
| | 30 | 1.3% | 1.28 |
| 4 | 40 | 1.8% | 1.24 |
| | 50 | 2.6% | 1.29 |



**Figure 4.9:** Left: table with the experimental measurements of polarization ratio and losses for single windows written with different pulse energy and number of layers. Right: Corresponding window profile pictures after being fully etched (97 minutes)

**Changing etching time**

In order to reassure us that the inconsistency we observed before was due to Fabry Perot cavity effects, we fabricated a new sample with single windows written with the optimal parameters from the previous experiment (30 nJ pulse energy and single layer). With the optimal writing parameters established we decided to

explore different window angles above Brewster ($\theta_B + [1, 2, 3, 4]\,°$). As seen in the theoretical analysis this can be promising in the case of angle independent losses.

During the etching process, we stopped at 3 different times, and characterized all the windows polarization ratio, plotting them with angle as can be seen in figure 4.10. For each of the plots (corresponding to different etching times) we used the model of independent Fabry Perot windows to fit as best as possible with the data points. As can be seen we can follow the increase of the air gap size, with an average etching rate of $50\,nm/min$.
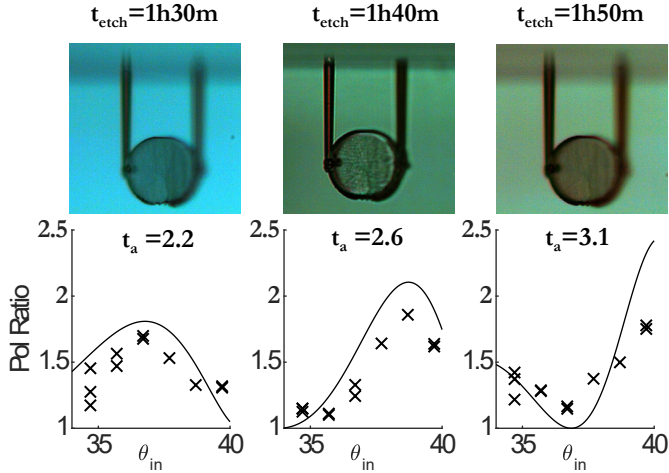


**Figure 4.10:** Windows measured at different points in the etching process. Top images: example of window profile at the corresponding etching time. Bottom: experimental plot of the measured polarization ratio vs tilting angle of the windows. Each cross is a single device. Curve corresponds to the closest fit found to the data by using the simple Fabry Perot model with $t_a$ as the air gap thickness.

## 4.3.2  Double windows

Having proved that we can observe interference in the air gap, this time we added a second window in order to see the glass gap interference. We tested two different distances between windows ($10\mu m$ and $40\mu m$) to check if we could also see this interference "switching off" at higher window separation (which was expected taking into account the analysis done before).

In figure 4.11 we can see the results from the measurement of the spectra of polarization ratio. Comparing the two columns (corresponding to different distances between windows) it is possible to see that there are high frequency oscillations that only appear for the $10\mu m$ distanced windows.

Another trend that we get throughout all the measurements is that for the final step of the etching the overall polarization ratio lowers and also the oscillations themselves lower in amplitude. This could be because at this point the etching is increasing roughness or rounding up the surfaces and thus distorting the interference effect. In the case of the windows on the right we see a slow

oscillation that is associated with the smaller air gap (we have FSR of $> 1\mu m$ for a $1\mu m$ air gap).
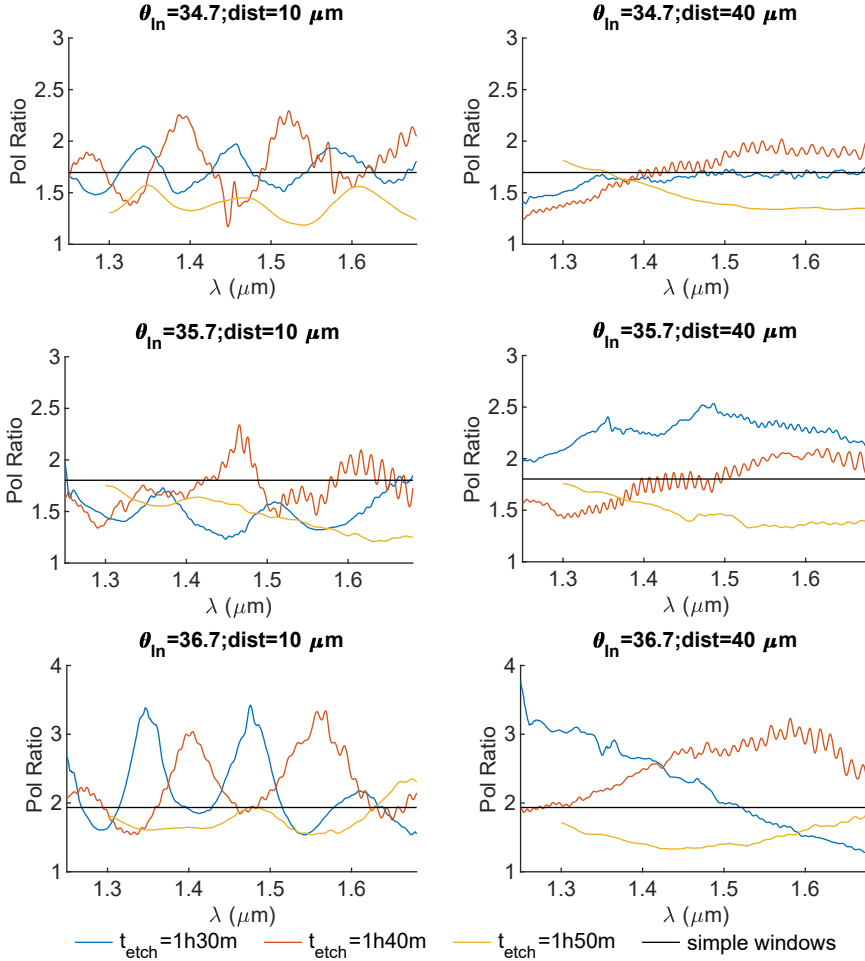


**Figure 4.11:** Polarization ratio for sets of double windows separated by $10\mu m$ (left column) and $40\mu m$ (right column), and at different etching times (different coloured lines) compared with the baseline expected from Fresnel reflections (black lines).

Using the spectra obtained for the 10 $\mu m$ gap windows at 34.7° and 35.7° we tried to fit the spectra using the full resonance model. Since we know the distance between the windows d (established by fabrication) we just have one free parameter, and we use the air gap size (in order to be able to compare the results with the single windows ones). The glass gap size is given by $t_b = dcos(\theta_{in}) - t_a$. The results are shown in figure 4.12.

Again we found that a reasonable fitting could be found for window thickness close to the one found in the single windows. Watching the air gap size progression with time we get a etching rate of 47 nm/min. A maximum polarization ratio of

8.5 dB and 7.1 dB was obtained for 36.7° and 34.7° tilting angle, respectively. Again particularly the last measured etching stage shows low polarization ratio values.
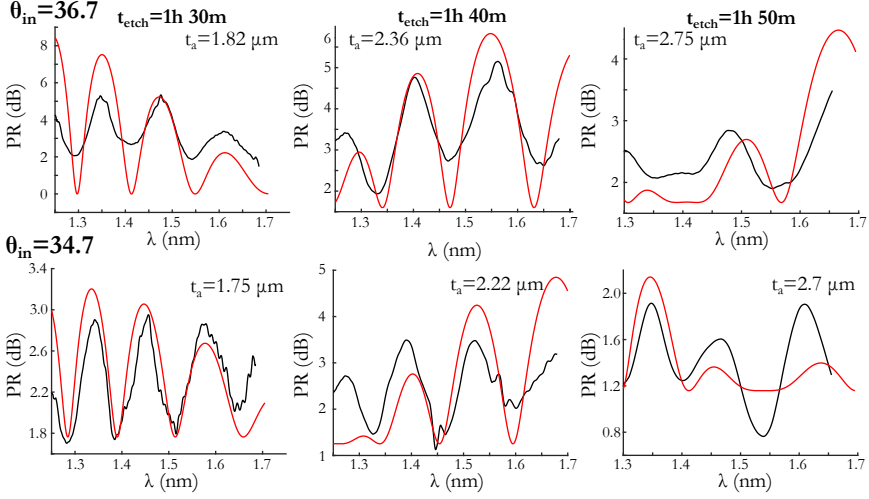


**Figure 4.12:** Fitting of the polarization ratio data (present if figure 4.11) acquired for the pairs of windows written with $10\mu m$ separation.

### 4.3.3   5-windows test

We set out a target polarization ratio for these windows of 100. As seen in the theoretical model, if we can tune the sizes of the air and glass gap we should be able to achieve this ratio with only 5 windows.

We fabricated a sample with several of these sets of 5 windows only slightly tuning the distance between them. This was done in order to have some tolerance on the etching time. Also, by measuring the polarization ratio of each window over time and comparing with the theoretical model we could have a more accurate estimation of the current window thickness and thus control the etching to the point we wanted.

The devices did not perform as we were expecting. We will now explore some of the reasons why this was the case.

**Etching non-uniformity**

A clear non uniformity on the etching rate of each window is evident from the microscope profile pictures in figure 4.13. It looks like the etching rate is lower at the centre than at the border. We had observed a similar effect in previous samples.

Furthermore we noticed that it was more prevalent if the windows were written closer together. Our interpretation was that it had to do with local etchant degradation that would saturate faster on the central region that had lot of material to be etched. It was particularly justified since our etching method did not

involve any stirring. So it could be that the etching concentration would degrade with time faster around the central part of the window stack if diffusion wasn't fast enough. Knowing this we used a stirring magnet at 240 rpm.

We have not yet tried using ultrasonic bath, in order to avoid the possibility of cracking the devices due to their small dimension. This seems like the logical next step to test and see if it improves the uniformity.
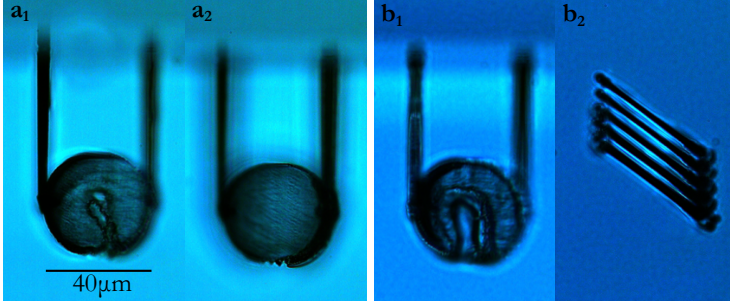


**Figure 4.13:** Display of the etching non uniformities observed: a) On the sets of double windows with $10\mu m$ ($a_1$) and $40\mu m$ ($a_2$), with the same etching time. b) 5 window stack example profile ($b_1$) and top view ($b_2$) after 1h25m etch.

**Beam divergence**

Looking more closely at the system we use for polarization ratio measurement (section 2.4), we notice that we have a diverging beam shinning through the windows. Considering Gaussian propagation after the fibre tip, we have that the Rayleigh length is $z_R = \frac{\pi\omega_0^2}{\lambda} = 80\mu m$. Since the position of the window is $100\mu m$ inside the glass and we need to add the distance from the fibre to the glass side, we are surely in the condition $z > zR$ and thus we can approximate beam divergence to $\theta = \frac{\lambda_0}{\pi n \omega_0} = 3.7°$. This means that as seen in the previous section the polarization ratio spectra would be washed out. This can explain in part some of the previous results in which the devices didn't perform as good as expected theoretically.

In order to improve these results we can add a microscope objective after the fibre tip aligned such that we place the beam waist at the window position. If we choose the right objective we can also have a long Rayleigh length so the diverging angle is small at the window position.

## 4.4 Conclusions

In this chapter we explored the possibility of fabricating air windows inside fused silica for polarization filtering, both from a theoretical and an experimental point of view. It was observed that if we can exploit Fabry Perot cavity effects we can drastically reduce the number of windows necessary for achieving the same polarization ratio. These effects were indeed confirmed both in the air gaps in the

single windows study, and glass gaps in the double windows study. Some challenges need to be tackled, particularly the uniformity of the etching. An analysis on the possible improvements both on the fabrication and characterization sides was provided.

# Chapter 5

# Glasses for attosecond pulse generation fabricated by FLICE technique

In this short chapter I will summarize the work done in collaboration with the group of Francesca Calegari at IFN-CNR and now at DESY Hamburg. Within this research we developed a glass device for delivering gas in a channel that was used for third harmonic generation to the deep UV wavelengths.

## 5.1 Motivation

The generation of attosecond pulses is an important tool that enables nowadays unprecedented experiments in Atomic and Molecular physics. Exploiting either the extreme broad spectrum (hundreds of nm) as a probe for spectroscopic measurements or the short pulse duration for making time-resolved measurements [117]. Pulses of few fs in visible and near infra-red wavelengths are easily created now-a-days thanks to hollow-core fibre technology [118]. There have been already demonstrations of sub-fs pulses on a wide spectrum, for both vacuum ultra violet (VUV-100:200 nm), [119], extreme ultra violet (XUV-10:100 nm) [120] and soft X-rays (0.01:10 nm) [121]. Generating sub-fs pulses in the deep UV (200-300 nm) is still difficult. Among the different techniques explored, third harmonic generation by near infra-red pulses is the most suitable candidate. Although the conversion efficiency is not as good as can be achieved with non-linear crystals, the dispersion induced on the UV pulse is much lower. The shortest pulses reported up till now at deep UV was precisely using third harmonic generation with Ne gas, arriving at 2.8 fs [122].

This gas medium is normally contained in metallic tubes, but these wear off with time and have to be substituted. Fused silica has negligible absorption at near IR wavelength and so can withstand the high pulse energies of these short pulses. Furthermore femtosecond laser micro-machining allows a complete control on both the shape and size of the cell, allowing a fine control on the gas density distribution and thus also control the generation of third harmonic.

## 5.2 Experimental

The fabrication line used for this project was the High Q line (for details check section 2.1). We used the green wavelength, following an already proven recipe that has provided in the past a good compromise between etching rate and surface roughness [123].

We used 2 mm thickness fused silica samples in order to have enough space to fit the vacuum tube. In general the fabrication for FLICE technique is less sensitive to aberrations in depth, so we could use the 50x objective for writing on the whole sample. In order to be able to write so deep we also increased slightly the writing pulse energy from $0.3\mu J$ to $0.325\mu J$. The writing polarization was perpendicular to the channel axis, in order to have maximum etching rate in that direction. The cell consists on a simple channel of 3 millimetres length and has a projected radius of $200\mu m$. It is connected in the centre to a cylindrical opening of 3 mm radius that will fit the metallic tube for the gas input. Since the channel has the same length as the access hole diameter, we had to create a diagonal entrance, with the micro-channel shifted with respect to the access hole (see figure 5.1). This also allowed an easier alignment of the beam with the channel, since it enables a clear view of the micro-channel.

The channel was written by making a series of concentric ellipses, with increasing radius. It starts from the outer edge so the bottom line is well defined, and proceeds to irradiate the inner rings. The programmed ellipticity compensates the effect of refractive mismatch between stage positions and actual focus position inside the glass.

In the first trials we observed some asymmetrical ellipticity, which came due to the elongated shaped modification that is left at the laser focus. In the case of a circle shaped laser path this effect leads to a bulge at the bottom part of the etched shape. In order to compensate this we reduced the bottom semi-ellipse radius by what we expected to be the length of the single point modification ($12.5\mu m$). You can see the resulting pattern in figure 5.1.

In order to reduce the total direct writing time, instead of writing the whole volume of the access hole we only irradiated the outline, and the whole piece would just detach and come out during the etching process. The writing duration of the program is about 3h. if we filled the volume it could easily reach a full day of fabrication depending on the pitch.

After laser irradiation, the sample was first observed under the microscope, and then we proceeded to the etching step. The etching was done at $35°C$ in a 20% concentration of HF in water, with the solution under ultra sound. The etching process lasted typically 7 h in total. After the first three hours the central access hole would detach and so we removed it from the solution. After the whole channel was etched we could finely tune its diameter by leaving it etching in periods of 5-15 minutes. In figure 5.1 you can see the sample after the fabrication. The main channel presents an ellipticity of 0.38. This is similar to the one found on the irradiated pattern before etching 0.42. If we compute the difference between longitudinal aberrations for the minimum and maximum depth of the irradiation pattern using equation 1.9 we get a difference of $23\mu m$ which is strikingly similar to the one we see in the microscope picture. This was
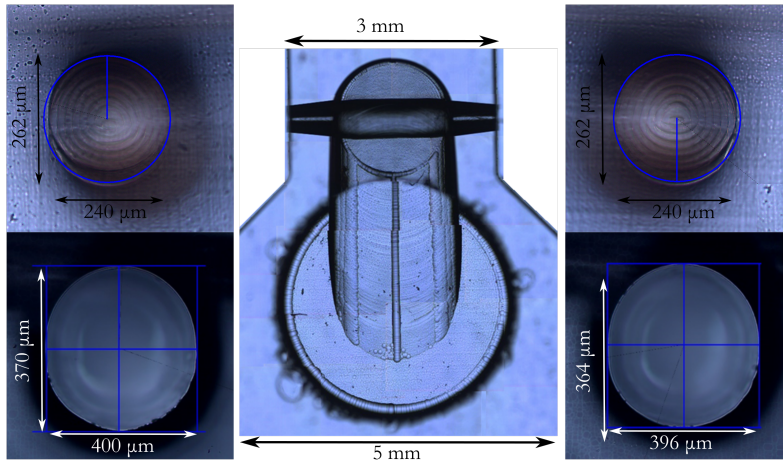
**Figure 5.1:** Composite of microscope images of the sample at the centre, with the respective front-views of the channel sides both before and after etching.

the only effect that was not taken into account at the moment of fabrication (we also corrected the whole fabrication for the paraxial refraction). It would be possible to reduce ellipticity by compensating further the irradiated cylinder based on the experimental results, but the current sample has worked quite well in the required setting so we finished at this point.

### 5.2.1 Final application

You can see in figure 5.2 the final setup where our cell is being used. A metal tube is inserted inside the central chamber, and glued so there is no leakage, and connected to the Ar gas line. The sample is mounted inside a larger chamber with a differential pumping system that pumps the Ar back out creating a constant flow through the central channel. In the scheme you can see two beam lines. At the input we have a 5 fs NIR (770 nm) pulse. The bottom side is used for UV generation. The top pulse side redirects a part of the beam so that it can be brought together again with the generated UV either for temporal characterization or for pump probe experiments. The whole system is kept under vacuum for reducing dispersion of the UV. Using this system a pulse of 1.9 fs was measured, establishing a new record on deep UV.
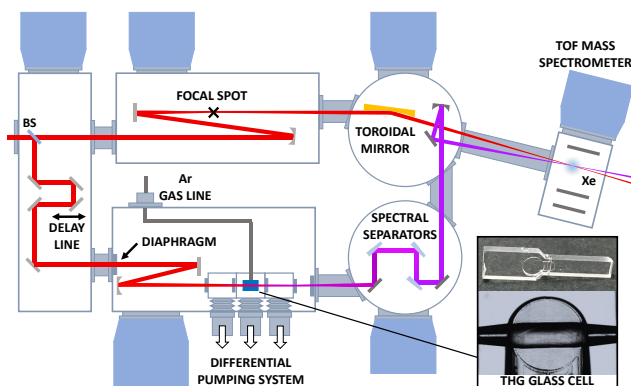


**Figure 5.2:** Scheme of the setup used for generation and characterization of deep UV pulses where our cell is integrated. The inset shows an overview picture and microscope close-up of the sample.

## 5.3 Prospects

In the future, a more complex device will be realized all by FLICE. In order to further increase the compactness and reduce the number of aligning steps the chamber with the differential pumping system in figure 5.2 will be instead integrated in the same glass chip. Having a smaller chamber where the gas is pumped out will also allow us to lower the gas consumption which gives savings on running cost of the experiment. In figure 5.3 you can see our current plant to achieve this integration. Each of the four 6 mm diameter chambers will fit one of the tubes for pumping the gas out. The central chamber will be similar to the previous sample, only without the diagonal access this time.

Some new challenges can be anticipated. The size of the device mean new strategies will need to be followed in order to reduce the fabrication time to reasonable numbers. One of the approaches possible is to use the same method used for the central channel for the larger holes that need to be created in glass. this would leave them open but we could glue a second glass at the bottom. Even with this it is possible that the fabrication time will be too long for a single step. In that case we could make alignment markers on the glass by ablation. It is possible to create ablation tracks at the surface with sizes similar to the ones we used in chapter 3. We already proven that we can get within $1\mu m$ alignment precision, which is more than enough for this application.
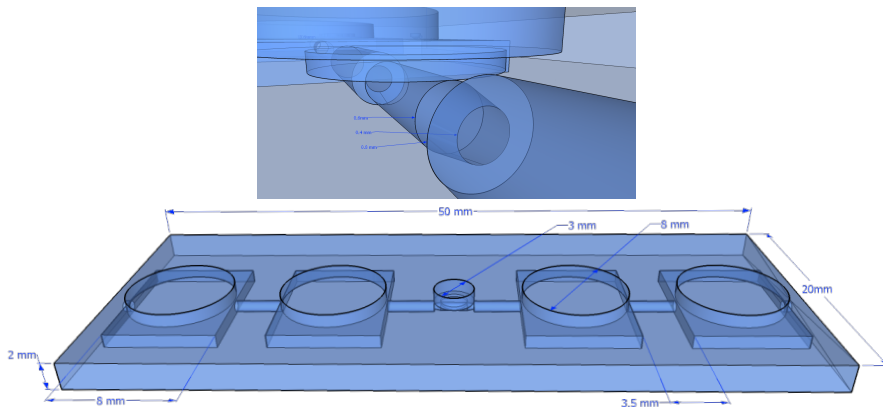


**Figure 5.3:** Scheme of the future atto-second pulse generation chip, with a close up of the central chamber connection shape and dimensions.

# Conclusions

In this work we presented several applications of femtosecond laser micro-machining in fused silica with a diverse range of topics, exploring both its use for the direct writing of waveguides, and the FLICE technique for the etching of structures in fused silica.

The major achievement was the fabrication of a vertical waveguide, that proved to be low loss (<1 dB) and could be bent with 3-6 degrees while keeping losses below 1.5 dB. These waveguides can be useful for opening up new possibilities that traditional lithographic based waveguides cannot provide.

We also explored the possibility of embedding a polarizing element inside glass, by fabricating with the FLICE technique Brewster windows. We demonstrated the possibility to explore interferometric effects in order to reduce the number of windows necessary and increase the compactness of such device.

Finally, we concluded with a simple application of the FLICE technique for the fabrication of a glass chamber for the distribution of gas for third harmonic generation of attosecond pulses in deep UV.

These three applications pay testimony to the versatility of the femtosecond direct writing technique: with the same fabrication setup we demonstrated applications in optical interconnections, polarising elements and channel fabrication.

# Acknowledgements

First of all, a big thanks to the people that made any of this possible. To my tutor Roberta Ramponi, and my supervisor Roberto Osellame, that accepted me in their group. A particular thank you for Roberto, that accompanied more closely my research here and was always helpful in all the discussions with new ideas to contribute. Oh, and without forgetting the help with the correction of this thesis!
Next in line must be Rebeca, for all her support. She was always the first I would resort both for discussing results and any administrative hick-ups. Muchas gracias!

To the whole group osellami. Everyone has been fantastic and helpful. I always heard horror stories from friends about the drama and conflicts within research groups. Here I always found a positive interaction, and a helping hand whenever I needed. Hope I was able to retribute in the same way. A special thanks must go to Giacomo that was from the first day I landed in Italy a very helpful friend, and a great office mate for the whole of my PhD. He and Petra were a great incentive and help in learning more about the Italian language and culture, and many ideas brewed from our discussions.

To Prof Peter Herman, for hosting me in his group, and all the insightful discussions we shared. But also to all my colleagues there, in particular Gligor that I shared the project with and was my go to person for getting around the lab. And to Canada as a whole, that showed some truth in the stereotype of being a welcoming country and was for me a life-changing experience both academically as humanly.

E uma notinha especial para a minha família, que sempre esteve lá para mim mesmo quando não estive para eles. Merecem todos eterna gratidão por isso!

# List of publications and Ph.D. schools attendance

## Peer-reviewed international journals

- D. Pereira Lopes, R. Martinez Vazquez, S. Tirelli, L. Tallone, M. Romagnoli, R. Osellame; "Through-optical-vias for photonic interconnections in glass by femtosecond laser writing", in preparation, *Light: Science & Applications.*

- M.Galli, V. Wanie, E. P. Månsson, A. Trabattoni, D. Pereira Lopes, R. Martínez Vázquez, R. Osellame, S. Stagira, M. Nisoli and F. Calegari; "Generation of deep ultraviolet sub-2fs pulses", under review, *Optics letters.*

## International conferences

- A.G. Ciriolo, R.M.Vázquez, D.Faccialà, M. Negro, M. Devetta, D. Pereira Lopes, A. Pusala, C.Vozzi, R. Osellame, S. Stagira; "High-order harmonic generation in a femtosecond-laser-micromachined chip", in *CLEO: Science and Innovations 2016*, San Jose, CA, US (2018).

- A.G. Ciriolo, R.M.Vázquez, G. Crippa, D.Faccialà, M. Negro, M. Devetta, D. Pereira Lopes, A. Pusala, P.G. Prabhash, C. Vozzi, R. Osellame, S. Stagira "High-order Harmonic Generation in Femtosecond laser-Micromachined Devices", in *High Intensity Lasers and High Field Phenomena*, Strasburg, France (2018).

- D. Pereira Lopes, , R. Martinez Vasquez, S. Tirelli , L. Tallone, M. Romagnoli, R. Osellame, "Longitudinal Writing of Vertical Waveguides in Fused Silica: Toward new Integrated Photonic Technologies", in *Photonics West*, San Francisco, CA, US (2018).

- R. Martínez Vazquez, S. Tirelli, D. Pereira Lopes, F. Agnano,J. Ayucar, L. Tallone, R. Osellame, M. Romagnoli; "Internode interconnection optical platform based on fs-laser written vertical waveguides", in *Photonics West*, San Francisco, CA, US (2018).

- Marco Romagnoli, G. Angelis, L. Tallone, V. Sorianello, S. Tirelli, B. Snyder, P. Heyn, Y. Ban, L. Bogaerts, P. Verheyen, A. Miller, J. Campenhout, M. Pantouvaki, P. Absil, J. Bauwelinck, X. Yin, D. Thourhout, J. Sandez, R. Osellame, R. Vázquez, D. Pereira Lopes, G. Preve, A. Rodrigo, P. Galli, G. Chiaretti, F. Testa, A. Bianchi, A. González; "High-bandwidth density optically interconnected terabit/s boards", in *Photonics West*, San Francisco, CA, US (2018).

## Italian conferences

- D. Pereira Lopes, R. Martínez Vazquez, R. Osellame; "Longitudinal writing of vertical waveguides in fused silica: toward new integrated photonic technologies", in *Fotonica 2017*, Padova, Italy (2017).

## Ph.D. schools

- "Photonic integration: advanced materials, new technologies and applications", Erice, Italy (2016). Poster presented.

# Bibliography

[1] Frank Träger, editor. *Springer Handbook of Lasers and Optics.* Springer Handbooks. Springer-Verlag, Berlin Heidelberg, 2 edition, 2012.

[2] Andrew Weiner. *Ultrafast Optics.* Wiley, Hoboken, N.J, 1 edition edition, June 2009.

[3] S. Butkus, E. Gaižauskas, D. Paipulas, Ž. Viburys, D. Kaškelytė, M. Barkauskas, A. Alesenkov, and V. Sirutkaitis. Rapid microfabrication of transparent materials using filamented femtosecond laser pulses. *Applied Physics A*, 114(1):81–90, January 2014.

[4] N. Huot, R. Stoian, A. Mermillod-Blondin, C. Mauclair, and E. Audouard. Analysis of the effects of spherical aberration on ultrafast laser-induced refractive index variation in glass. *Optics Express*, 15(19):12395–12408, September 2007.

[5] V. Diez-Blanco, Jan Siegel, Andrés Ferrer, A. Ruiz de la Cruz, and J. Solis. Deep subsurface waveguides with circular cross section produced by femtosecond laser writing. *Applied Physics Letters*, 91(5):051104, 2007.

[6] C. Hnatovsky, R. S. Taylor, E. Simova, V. R. Bhardwaj, D. M. Rayner, and P. B. Corkum. High-resolution study of photoinduced modification in fused silica produced by a tightly focused femtosecond laser beam in the presence of aberrations. *Journal of Applied Physics*, 98(1):013517, July 2005.

[7] Erik H. Waller, Michael Renner, and Georg von Freymann. Active aberration-and point-spread-function control in direct laser writing. *Optics express*, 20(22):24949–24956, 2012.

[8] Martynas Beresna, Mindaugas Gecevičius, and Peter G. Kazansky. Ultrafast laser direct writing and nanostructuring in transparent materials. *Advances in Optics and Photonics*, 6(3):293–339, 2014.

[9] Alexander Jesacher and Martin J. Booth. Parallel direct laser writing in three dimensions with spatially dependent aberration correction. *Optics express*, 18(20):21090–21099, 2010.

[10] L. Sudrie, A. Couairon, M. Franco, B. Lamouroux, B. Prade, S. Tzortzakis, and A. Mysyrowicz. Femtosecond Laser-Induced Damage and Filamentary Propagation in Fused Silica. *Physical Review Letters*, 89(18):186601, October 2002.

[11] L. V. Keldysh. Ionization in the field of a strong electromagnetic wave. *Sov. Phys. JETP*, 20(5):1307–1314, 1965.

[12] N. S. Shcheblanov, M. E. Povarnitsyn, P. N. Terekhin, S. Guizard, and A. Couairon. Nonlinear photoionization of transparent solids: A nonperturbative theory obeying selection rules. *Physical Review A*, 96(6):063410, 2017.

[13] Kazuyoshi Itoh, Wataru Watanabe, Stefan Nolte, and Chris B. Schaffer. Ultrafast processes for bulk modification of transparent materials. *MRS bulletin*, 31(8):620–625, 2006.

[14] James W. Chan, Thomas Huser, S. Risbud, and D. M. Krol. Structural changes in fused silica after exposure to focused femtosecond laser pulses. *Optics letters*, 26(21):1726–1728, 2001.

[15] K. Miura Davis, Kiyotaka Miura, Naoki Sugimoto, and Kazuyuki Hirao. Writing waveguides in glass with a femtosecond laser. *Optics letters*, 21(21):1729–1731, 1996.

[16] A. Saliminia, R. Vallee, and S. L. Chin. Waveguide writing in silica glass with femtosecond pulses from an optical parametric amplifier at 1.5 m. *Optics communications*, 256(4-6):422–427, 2005.

[17] Yasuhiko Shimotsuma, Peter G. Kazansky, Jiarong Qiu, and Kazuoki Hirao. Self-organized nanogratings in glass irradiated by ultrashort light pulses. *Physical review letters*, 91(24):247405, 2003.

[18] C. Hnatovsky, R. S. Taylor, P. P. Rajeev, E. Simova, V. R. Bhardwaj, D. M. Rayner, and P. B. Corkum. Pulse duration dependence of femtosecond-laser-fabricated nanogratings in fused silica. *Applied Physics Letters*, 87(1):014104, 2005.

[19] Sören Richter, Matthias Heinrich, Sven Döring, Andreas Tünnermann, Stefan Nolte, and Ulf Peschel. Nanogratings in fused silica: Formation, control, and applications. *Journal of Laser Applications*, 24(4):042008, July 2012.

[20] Rod Taylor, Cyril Hnatovsky, and Eli Simova. Applications of femtosecond laser induced self-organized planar nanocracks inside fused silica glass. *Laser & Photonics Reviews*, 2(1-2):26–46, 2008.

[21] Ye Dai, Aabid Patel, Juan Song, Martynas Beresna, and Peter G. Kazansky. Void-nanograting transition by ultrashort laser pulse irradiation in silica glass. *Optics Express*, 24(17):19344, August 2016.

[22] E. N. Glezer and E. Mazur. Ultrafast-laser driven micro-explosions in transparent materials. *Applied Physics Letters*, 71(7):882–884, August 1997.

[23] Wataru Watanabe, Tadamasa Toma, Kazuhiro Yamada, Junji Nishii, Ken-ichi Hayashi, and Kazuyoshi Itoh. Optical seizing and merging of voids in silica glass with infrared femtosecond laser pulses. *Optics Letters*, 25(22):1669–1671, November 2000.

[24] E. N. Glezer, M. Milosavljevic, L. Huang, R. J. Finlay, T.-H. Her, J. P. Callan, and E. Mazur. Three-dimensional optical storage inside transparent materials. *Optics Letters*, 21(24):2023–2025, December 1996.

[25] Eiji Toratani, Masanao Kamata, and Minoru Obara. Self-fabrication of void array in fused silica by femtosecond laser processing. *Applied Physics Letters*, 87(17):171103, October 2005.

[26] Shingo Kanehira, Jinhai Si, Jianrong Qiu, Koji Fujita, and Kazuyuki Hirao. Periodic nanovoid structures via femtosecond laser irradiation. *Nano Letters*, 5(8):1591–1595, 2005.

[27] Yves Bellouard and Max-Olivier Hongler. Femtosecond-laser generation of self-organized bubble patterns in fused silica. *Optics Express*, 19(7):6807–6821, March 2011.

[28] P. K. Tien. Light Waves in Thin Films and Integrated Optics. *Applied Optics*, 10(11):2395–2413, November 1971.

[29] Takeshi Kitagawa, Kuninori Hattori, Yoshinori Hibino, and Yasuji Ohmori. Neodymium-doped silica-based planar waveguide lasers. *Journal of lightwave technology*, 12(3):436–442, 1994.

[30] M. P. Roe, M. Hempstead, J. L. Archambault, P. St J. Russell, and L. Dong. Strong photo-induced refractive index changes in RF-sputtered tantalum oxide planar waveguides. 1994.

[31] A. Neyer, T. Knoche, and L. Muller. Fabrication of low loss polymer waveguides using injection moulding technology. *Electronics letters*, 29(4):399–401, 1993.

[32] Tatsuo Izawa and Hiroshi Nakagome. Optical waveguide formed by electrically induced migration of ions in glass plates. *Applied Physics Letters*, 21(12):584–586, 1972.

[33] Ruey-Ching Twu, Chia-Chih Huang, and Way-Seen Wang. TE-pass Zn-diffused LiNbO3 waveguide polarizer. *Microwave and Optical Technology Letters*, 48(11):2312–2314, 2006.

[34] John D. Bierlein, August Ferretti, Lothar H. Brixner, and William Y. Hsu. Fabrication and characterization of optical waveguides in KTiOPO4. *Applied Physics Letters*, 50(18):1216–1218, 1987.

[35] J. L. Jackel, V. Ramaswamy, and S. P. Lyman. Elimination of out-diffused surface guiding in titanium-diffused LiNbO3. *Applied Physics Letters*, 38(7):509–511, 1981.

[36] R. D. Standley, W. M. Gibson, and J. W. Rodgers. Properties of ion-bombarded fused quartz for integrated optics. *Applied optics*, 11(6):1313–1316, 1972.

[37] W. T. Tsang. Extremely low threshold (AlGa) As graded-index waveguide separate-confinement heterostructure lasers grown by molecular beam epitaxy. *Applied Physics Letters*, 40(3):217–219, 1982.

[38] V. G. Kozlov, V. Bulović, P. E. Burrows, and S. R. Forrest. Laser action in organic semiconductor waveguide and double-heterostructure devices. *Nature*, 389(6649):362, 1997.

[39] B. Jalali, A. F. J. Levi, F. Ross, and E. A. Fitzgerald. SiGe waveguide photodetectors grown by rapid thermal chemical vapour deposition. *Electronics Letters*, 28(3):269–271, 1992.

[40] Jared F. Bauters, Martijn JR Heck, Demis John, Daoxin Dai, Ming-Chun Tien, Jonathon S. Barton, Arne Leinse, René G. Heideman, Daniel J. Blumenthal, and John E. Bowers. Ultra-low-loss high-aspect-ratio Si 3 N 4 waveguides. *Optics Express*, 19(4):3163–3174, 2011.

[41] R. Adar, Y. Shani, C. H. Henry, R. C. Kistler, G. E. Blonder, and N. A. Olsson. Measurement of very low-loss silica on silicon waveguides with a ring resonator. *Applied physics letters*, 58(5):444–445, 1991.

[42] Douglas J. Little, Martin Ams, Peter Dekker, Graham D. Marshall, Judith M. Dawes, and Michael J. Withford. Femtosecond laser modification of fused silica: the effect of writing polarization on Si-O ring structure. *Optics express*, 16(24):20029–20037, 2008.

[43] Bruce G. Aitken, Nicholas F. Borrelli, David L. Morse, and Alexander Streltsov. Femtosecond laser writing of glass, including borosilicate, sulfide, and lead glasses, June 2003.

[44] James W. Chan, Thomas R. Huser, Subhash H. Risbud, Joseph S. Hayden, and Denise M. Krol. Waveguide fabrication in phosphate glasses using femtosecond laser pulses. *Applied physics letters*, 82(15):2371–2373, 2003.

[45] Arnaud Zoubir, Martin Richardson, Clara Rivero, Alfons Schulte, Cedric Lopez, Kathleen Richardson, Nicolas Hô, and Réal Vallée. Direct femtosecond laser writing of waveguides in As 2 S 3 thin films. *Optics letters*, 29(7):748–750, 2004.

[46] Jens Thomas, Matthias Heinrich, Jonas Burghoff, Stefan Nolte, Antonio Ancona, and Andreas Tünnermann. Femtosecond laser-written quasi-phase-matched waveguides in lithium niobate. *Applied Physics Letters*, 91(15):151108, 2007.

[47] Amir H. Nejadmalayeri, Peter R. Herman, Jonas Burghoff, Matthias Will, Stefan Nolte, and Andreas Tünnermann. Inscription of optical waveguides in crystalline silicon by mid-infrared femtosecond laser pulses. *Optics letters*, 30(9):964–966, 2005.

[48] Seiji Sowa, Wataru Watanabe, Takayuki Tamaki, Junji Nishii, and Kazuyoshi Itoh. Symmetric waveguides in poly (methyl methacrylate) fabricated by femtosecond laser pulses. *Optics Express*, 14(1):291–297, 2006.

[49] G. Cerullo, Roberto Osellame, Stefano Taccheo, M. Marangoni, Dario Polli, Roberta Ramponi, Paolo Laporta, and Sandro De Silvestri. Femtosecond micromachining of symmetric waveguides at 1.5 m by astigmatic beam focusing. *Optics letters*, 27(21):1938–1940, 2002.

[50] Ya Cheng, Koji Sugioka, Katsumi Midorikawa, Masashi Masuda, Koichi Toyoda, Masako Kawachi, and Kazuhiko Shihoyama. Control of the cross-sectional shape of a hollow microchannel embedded in photostructurable glass by use of a femtosecond laser. *Optics letters*, 28(1):55–57, 2003.

[51] Yusuke Nasu, Masaki Kohtoku, and Yoshinori Hibino. Low-loss waveguides written with a femtosecond laser for flexible interconnection in a planar light-wave circuit. *Optics letters*, 30(7):723–725, 2005.

[52] Wataru Watanabe, Yumiko Note, and Kazuyoshi Itoh. Fabrication of multimode interference waveguides in glass by use of a femtosecond laser. *Optics letters*, 30(21):2888–2890, 2005.

[53] Luís A. Fernandes, Jason R. Grenier, Peter R. Herman, J. Stewart Aitchison, and Paulo VS Marques. Femtosecond laser writing of waveguide retarders in fused silica for polarization control in optical circuits. *Optics express*, 19(19):18294–18301, 2011.

[54] Cyril Mauclair, Alexandre Mermillod-Blondin, Nicolas Huot, Eric Audouard, and Razvan Stoian. Ultrafast laser writing of homogeneous longitudinal waveguides in glasses using dynamic wavefront correction. *Optics express*, 16(8):5481–5492, 2008.

[55] Xuewen Long, Jing Bai, Wei Zhao, Razvan Stoian, Rongqing Hui, and Guanghua Cheng. Stressed waveguides with tubular depressed-cladding inscribed in phosphate glasses by femtosecond hollow laser beams. *Optics letters*, 37(15):3138–3140, 2012.

[56] Shane Eaton. *Contrasts in Thermal Dffusion and Heat Accumulation Effects in the Fabrication of Waveguides in Glasses using Variable Repetition Rate Femtosecond Laser*. PhD Thesis, 2008.

[57] M. A. Bukharin, D. V. Khudyakov, and S. K. Vartapetov. Heat accumulation regime of femtosecond laser writing in fused silica and Nd: phosphate glass. *Applied Physics A*, 119(1):397–403, 2015.

[58] Shane M. Eaton, Haibin Zhang, Mi Li Ng, Jianzhao Li, Wei-Jen Chen, Stephen Ho, and Peter R. Herman. Transition from thermal diffusion to heat accumulation in high repetition rate femtosecond laser writing of buried optical waveguides. *Optics express*, 16(13):9443–9458, 2008.

[59] Roberto Osellame, Hugo JWM Hoekstra, Giulio Cerullo, and Markus Pollnau. Femtosecond laser microstructuring: an enabling tool for optofluidic lab-on-chips. *Laser & Photonics Reviews*, 5(3):442–463, 2011.

[60] Lawrence Shah, Alan Y. Arai, Shane M. Eaton, and Peter R. Herman. Waveguide writing in fused silica with a femtosecond fiber laser at 522 nm and 1 MHz repetition rate. *Optics express*, 13(6):1999–2006, 2005.

[61] Takeshi Fukuda, Shimon Ishikawa, Tomoko Fujii, Ken Sakuma, and Hideyuki Hosoya. Low-loss optical waveguides written by femtosecond laser pulses for three-dimensional photonic devices. In *Photon Processing in Microelectronics and Photonics III*, volume 5339, pages 524–539. International Society for Optics and Photonics, 2004.

[62] Roberto Osellame, N. Chiodo, V. Maselli, A. Yin, Margherita Zavelani-Rossi, G. Cerullo, Paolo Laporta, L. Aiello, S. De Nicola, and P. Ferraro. Optical properties of waveguides written by a 26 MHz stretched cavity Ti: sapphire femtosecond oscillator. *Optics Express*, 13(2):612–620, 2005.

[63] Jun Guan, Xiang Liu, Patrick S. Salter, and Martin J. Booth. Hybrid laser written waveguides in fused silica for low loss and polarization independence. *Optics express*, 25(5):4845–4859, 2017.

[64] Jiaren Liu, Zhiyi Zhang, Shoude Chang, Costel Flueraru, and Chander P. Grover. Directly writing of 1-to-N optical waveguide power splitters in fused silica glass using a femtosecond laser. *Optics communications*, 253(4-6):315–319, 2005.

[65] Andrea Crespi, Yu Gu, Bongkot Ngamsom, Hugo JWM Hoekstra, Chaitanya Dongre, Markus Pollnau, Roberta Ramponi, Hans H. van den Vlekkert, Paul Watts, and Giulio Cerullo. Three-dimensional Mach-Zehnder interferometer in a microfluidic chip for spatially-resolved label-free detection. *Lab on a Chip*, 10(9):1167–1173, 2010.

[66] Luís A. Fernandes, Jason R. Grenier, Peter R. Herman, J. Stewart Aitchison, and Paulo VS Marques. Femtosecond laser fabrication of birefringent directional couplers as polarization beam splitters in fused silica. *Optics express*, 19(13):11992–11999, 2011.

[67] Shane M. Eaton, Wei-Jen Chen, Haibin Zhang, Rajiv Iyer, Jianzhao Li, Mi Li Ng, Stephen Ho, J. Stewart Aitchison, and Peter R. Herman. Spectral loss characterization of femtosecond laser written waveguides in glass with application to demultiplexing of 1300 and 1550 nm wavelengths. *Journal of Lightwave Technology*, 27(9):1079–1085, 2009.

[68] Andrius Marcinkevičius, Saulius Juodkazis, Mitsuru Watanabe, Masafumi Miwa, Shigeki Matsuo, Hiroaki Misawa, and Junji Nishii. Femtosecond laser-assisted three-dimensional microfabrication in silica. *Optics letters*, 26(5):277–279, 2001.

[69] Ya Cheng, Hai-Lung Tsai, K. Sugioka, and K. Midorikawa. Fabrication of 3d microoptical lenses in photosensitive glass using femtosecond laser micromachining. *Applied Physics A*, 85(1):11–14, 2006.

[70] Rod S. Taylor, Cyril Hnatovsky, Eli Simova, David M. Rayner, M. Mehandale, V. R. Bhardwaj, and P. B. Corkum. Ultra-high resolution index of refraction profiles of femtosecond laser modified silica structures. *Optics express*, 11(7):775–781, 2003.

[71] Xiaoming Yu, Yang Liao, Fei He, Bin Zeng, Ya Cheng, Zhizhan Xu, Koji Sugioka, and Katsumi Midorikawa. Tuning etch selectivity of fused silica irradiated by femtosecond laser pulses by controlling polarization of the writing pulses. *Journal of Applied Physics*, 109(5):053114, 2011.

[72] Debaditya Choudhury, William T. Ramsay, Robert Kiss, Nicholas A. Willoughby, Lynn Paterson, and Ajoy K. Kar. A 3d mammalian cell separator biochip. *Lab on a Chip*, 12(5):948–953, 2012.

[73] Valeria Maselli, Roberto Osellame, Giulio Cerullo, Roberta Ramponi, Paolo Laporta, Luca Magagnin, and Pietro Luigi Cavallotti. Fabrication of long microchannels with circular cross section using astigmatically shaped femtosecond laser pulses and chemical etching. *Applied physics letters*, 88(19):191107, 2006.

[74] Roberto Osellame, Valeria Maselli, Rebeca Martinez Vazquez, Roberta Ramponi, and Giulio Cerullo. Integration of optical waveguides and microfluidic channels both fabricated by femtosecond laser irradiation. *Applied physics letters*, 90(23):231118, 2007.

[75] Krishna Chaitanya Vishnubhatla, Nicola Bellini, Roberta Ramponi, Giulio Cerullo, and Roberto Osellame. Shape control of microchannels fabricated in fused silica by femtosecond laser irradiation and chemical etching. *Optics express*, 17(10):8685–8695, 2009.

[76] Satoshi Kiyama, Shigeki Matsuo, Shuichi Hashimoto, and Yasushi Morihira. Examination of etching agent and etching mechanism on femotosecond laser microfabrication of channels inside vitreous silica substrates. *The Journal of Physical Chemistry C*, 113(27):11560–11566, 2009.

[77] Yves Bellouard, Ali Said, Mark Dugan, and Philippe Bado. Fabrication of high-aspect ratio, micro-fluidic channels and tunnels using femtosecond laser pulses and chemical etching. *Optics express*, 12(10):2120–2129, 2004.

[78] Yuri Sikorski, Corneliu Rablau, Mark Dugan, Ali A. Said, Philippe Bado, and Lars Guenter Beholz. Fabrication and characterization of microstructures with optical quality surfaces in fused silica glass using femtosecond laser pulses and chemical etching. *Applied optics*, 45(28):7519–7523, 2006.

[79] Fei He, Ya Cheng, Lingling Qiao, Chen Wang, Zhizhan Xu, Koji Sugioka, Katsumi Midorikawa, and Ji Wu. Two-photon fluorescence excitation with a microlens fabricated on the fused silica chip by femtosecond laser micromachining. *Applied Physics Letters*, 96(4):041108, 2010.

[80] Stephen Ho, Peter R. Herman, and J. Stewart Aitchison. Single-and multi-scan femtosecond laser writing for selective chemical etching of cross section patternable glass micro-channels. *Applied Physics A*, 106(1):5–13, 2012.

[81] Lingling Qiao, Fei He, Chen Wang, Yang Liao, Ya Cheng, Koji Sugioka, Katsumi Midorikawa, Change Pan, and Xunbin Wei. Fabrication of a micro-optical lens using femtosecond laser 3d micromachining for two-photon imaging of bio-tissues. *Optics Communications*, 284(12):2988–2991, 2011.

[82] Robert W. Applegate Jr, Jeff Squier, Tor Vestad, John Oakey, David WM Marr, Philippe Bado, Mark A. Dugan, and Ali A. Said. Microfluidic sorting system based on optical waveguide integration and diode laser bar trapping. *Lab on a Chip*, 6(3):422–426, 2006.

[83] I. Mansour and F. Caccavale. An improved procedure to calculate the refractive index profile from the measured near-field intensity. *Journal of lightwave technology*, 14(3):423–428, 1996.

[84] D. Gloge. Bending loss in multimode fibers with graded and ungraded core index. *Applied optics*, 11(11):2506–2513, 1972.

[85] Robert G. Hunsperger. Theory of optical waveguides. In *Integrated Optics*, pages 33–52. Springer, 2009.

[86] David AB Miller. Physical reasons for optical interconnection. *Int. J. Optoelectron*, 11:155–168, 1997.

[87] Wang Miao, Fulong Yan, and Nicola Calabretta. Towards petabit/s all-optical flat data center networks based on WDM optical cross-connect switches with flow control. *Journal of Lightwave Technology*, 34(17):4066–4075, 2016.

[88] Hiren D. Thacker, Roshanak Shafiiha, Jon Lexau, Xuezhe Zheng, Stevan S. Djordjevic, Shiyun Lin, John Simons, Arin Abed, Phil Amberg, and Eric Chang. Hybrid integration and packaging of an energy-efficient WDM silicon photonic chip-to-chip interconnect. In *Electronic Components and Technology Conference (ECTC), 2015 IEEE 65th*, pages 762–767. IEEE, 2015.

[89] Samuel Palermo, Patrick Chiang, Cheng Li, Chin-Hui Chen, Marco Fiorentino, Ray Beausoleil, Hao Li, Kunzhi Yu, Binhao Wang, and Rui Bai. Silicon photonic microring resonator-based transceivers for compact WDM optical interconnects. In *Compound Semiconductor Integrated Circuit Symposium (CSICS), 2015 IEEE*, pages 1–4. IEEE, 2015.

[90] Y. Hsu, C. Chuang, X. Wu, G. Chen, C. Hsu, Y. Chang, C. Chow, J. Chen, Y. Lai, C. Yeh, and H. K. Tsang. 2.6 Tbit/s On-Chip Optical Interconnect Supporting Mode-Division-Multiplexing and PAM-4 Signal. *IEEE Photonics Technology Letters*, 30(11):1052–1055, June 2018.

[91] David AB Miller and Haldun M. Ozaktas. Limit to the bit-rate capacity of electrical interconnects from the aspect ratio of the system architecture. *Journal of parallel and distributed computing*, 41(1):42–52, 1997.

[92] Rami Melhem. Time-Multiplexing Optical Interconnection Networks; Why Does it Pay Off? In *In Proceedings of the 1995 ICPP workshop on Challenges for Parallel Processing*, pages 30–35, 1995.

[93] Haik Mardoyan, Miquel Angel Mestre, Rafael Rios-Müller, Agnieszka Konczykowska, Jeremie Renaudier, Filipe Jorge, Bernadette Duval, Jean-Yves Dupuy, Amirhossein Ghazisaeidi, and Philippe Jennevé. Single carrier 168-Gb/s line-rate PAM direct detection transmission using high-speed selector power DAC for optical interconnects. *Journal of Lightwave Technology*, 34(7):1593–1598, 2016.

[94] P. Yang, S. Nakamura, K. Yashiki, Z. Wang, L. H. K. Duong, Z. Wang, X. Chen, Y. Nakamura, and J. Xu. Inter/intra-chip optical interconnection network: opportunities, challenges, and implementations. In *2016 Tenth IEEE/ACM International Symposium on Networks-on-Chip (NOCS)*, pages 1–8, August 2016.

[95] Qixiang Cheng, Meisam Bahadori, Madeleine Glick, Sébastien Rumley, and Keren Bergman. Recent advances in optical technologies for data centers: a review. *Optica*, 5(11):1354–1370, November 2018.

[96] Xuezhe Zheng, John E. Cunningham, Ivan Shubin, John Simons, Mehdi Asghari, Dazeng Feng, Hongbin Lei, Dawei Zheng, Hong Liang, and Cheng-chih Kung. Optical proximity communication using reflective mirrors. *Optics Express*, 16(19):15052–15058, 2008.

[97] Mehrdad Mirshafiei, Jean-Philippe Bérubé, Stephane Lessard, Réal Vallée, and David V. Plant. Glass interposer for short reach optical connectivity. *Optics express*, 24(11):12375–12384, 2016.

[98] N. Lindenmann, G. Balthasar, D. Hillerkuss, R. Schmogrow, M. Jordan, J. Leuthold, W. Freude, and C. Koos. Photonic wire bonding: a novel concept for chip-scale interconnects. *Optics express*, 20(16):17667–17677, 2012.

[99] Josh A. Conway, Subal Sahni, and Thomas Szkopek. Plasmonic interconnects versus conventional interconnects: a comparison of latency, crosstalk and energy costs. *Optics express*, 15(8):4474–4484, 2007.

[100] Jin Tae Kim, Jung Jin Ju, Suntak Park, Min-su Kim, Seung Koo Park, and Myung-Hyun Lee. Chip-to-chip optical interconnect using gold long-range surface plasmon polariton waveguides. *Optics Express*, 16(17):13133–13138, 2008.

[101] B. J. Nagy, Laurent Gallais, L. Vámos, D. Oszetzky, P. Rácz, and P. Dombi. Direct comparison of kilohertz-and megahertz-repetition-rate femtosecond damage threshold. *Optics letters*, 40(11):2525–2528, 2015.

[102] Ben McMillen and Yves Bellouard. On the anisotropy of stress-distribution induced in glasses and crystals by non-ablative femtosecond laser exposure. *Optics Express*, 23(1):86–100, January 2015.

[103] Siniša Vukelić, Panjawat Kongsuwan, Sunmin Ryu, and Y. Lawrence Yao. Ultrafast Laser Induced Structural Modification of Fused Silica—Part II: Spatially Resolved and Decomposed Raman Spectral Analysis. *Journal of Manufacturing Science and Engineering*, 132(6):061013, 2010.

[104] H. Sugiura and T. Yamadaya. Raman scattering in silica glass in the permanent densification region. *Journal of non-crystalline solids*, 144:151–158, 1992.

[105] Shirley V. King. Ring Configurations in a Random Network Model of Vitreous Silica. *Nature*, 213(5081):1112, March 1967.

[106] Jonathan J. Witcher, Wilbur J. Reichman, Luke B. Fletcher, Neil W. Troy, and Denise M. Krol. Thermal annealing of femtosecond laser written structures in silica glass. *Optical Materials Express*, 3(4):502–510, 2013.

[107] Y. Wang and A. M. Shkel. Study on surface roughness improvement of Fused Quartz after thermal and chemical post-processing. In *2016 IEEE International Symposium on Inertial Sensors and Systems*, pages 101–104, February 2016.

[108] Matthias Will, Stefan Nolte, Boris N. Chichkov, and Andreas Tünnermann. Optical properties of waveguides fabricated in fused silica by femtosecond laser pulses. *Applied Optics*, 41(21):4360–4364, 2002.

[109] Marco Romagnoli, Gabriele De Angelis, Luigi Tallone, Vito Sorianello, Stefano Tirelli, Bradley Snyder, Peter De Heyn, Yoojin Ban, Lieve Bogaerts, and Peter Verheyen. High-bandwidth density optically interconnected terabit/s boards. In *Metro and Data Center Optical Networks and Short-Reach Links*, volume 10560, page 105600E. International Society for Optics and Photonics, 2018.

[110] Rang Chu, Chunying Guan, Jing Yang, Zheng Zhu, Ping Li, Jinhui Shi, Peixuan Tian, Libo Yuan, and Gilberto Brambilla. High extinction ratio D-shaped fiber polarizers coated by a double graphene/PMMA stack. *Optics Express*, 25(12):13278–13285, 2017.

[111] Kaiming Zhou, George Simpson, Xianfeng Chen, Lin Zhang, and Ian Bennion. High extinction ratio in-fiber polarizers based on 45° tilted fiber Bragg gratings. *Optics letters*, 30(11):1285–1287, 2005.

[112] Kenneth KC Lee, Adrian Mariampillai, Moez Haque, Beau A. Standish, Victor XD Yang, and Peter R. Herman. Temperature-compensated fiber-optic 3d shape sensor based on femtosecond laser direct-written Bragg grating waveguides. *Optics express*, 21(20):24076–24086, 2013.

[113] Lei Yuan, Jie Huang, Xinwei Lan, Hanzheng Wang, Lan Jiang, and Hai Xiao. All-in-fiber optofluidic sensor fabricated by femtosecond laser assisted chemical etching. *Optics letters*, 39(8):2358–2361, 2014.

[114] Moez Haque and Peter R. Herman. Chemical-assisted femtosecond laser writing of optical resonator arrays. *Laser & Photonics Reviews*, 9(6):656–665, 2015.

[115] Edl Schamiloglu, Kevin J. Malloy, Kamil Agi, and Mohammed Mojahedi. Photonic Crystal Flat Panel Radiators for Wideband High Power Antennas. Technical report, NEW MEXICO UNIV ALBUQUERQUE CENTER FORHIGH TECHNOLOGY MATERIALS, 1999.

[116] H. Abu-Safia, R. Al-Tahtamouni, I. Abu-Aljarayesh, and N. A. Yusuf. Transmission of a Gaussian beam through a Fabry–Perot interferometer. *Applied optics*, 33(18):3805–3811, 1994.

[117] Ferenc Krausz and Misha Ivanov. Attosecond physics. *Reviews of Modern Physics*, 81(1):163–234, February 2009.

[118] Mauro Nisoli, Sandro De Silvestri, and Orazio Svelto. Generation of high energy 10 fs pulses by a new pulse compression technique. *Applied Physics Letters*, 68(20):2793–2795, 1996.

[119] D. Fabris, T. Witting, W. A. Okell, D. J. Walke, P. Matia-Hernando, J. Henkel, T. R. Barillot, M. Lein, J. P. Marangos, and J. W. G. Tisch. Synchronized pulses generated at 20 eV and 90 eV for attosecond pump–probe experiments. *Nature Photonics*, 9(6):383, 2015.

[120] Giuseppe Sansone, Enrico Benedetti, Francesca Calegari, Caterina Vozzi, Lorenzo Avaldi, Roberto Flammini, Luca Poletto, P. Villoresi, C. Altucci, and R. Velotta. Isolated single-cycle attosecond pulses. *Science*, 314(5798):443–446, 2006.

[121] Seth L. Cousin, Nicola Di Palo, Bárbara Buades, Stephan M. Teichmann, M. Reduzzi, M. Devetta, A. Kheifets, G. Sansone, and Jens Biegert. Attosecond streaking in the water window: A new regime of attosecond pulse characterization. *Physical Review X*, 7(4):041030, 2017.

[122] Florentin Reiter, Ulrich Graf, Martin Schultze, Wolfgang Schweinberger, Hartmut Schröder, Nicholas Karpowicz, Abdallah Mohammed Azzeer, Reinhard Kienberger, Ferenc Krausz, and Eleftherios Goulielmakis. Generation of sub-3 fs pulses in the deep ultraviolet. *Optics letters*, 35(13):2248–2250, 2010.

[123] Petra Paiè, Francesca Bragheri, Rebeca Martinez Vazquez, and Roberto Osellame. Straightforward 3d hydrodynamic focusing in femtosecond laser fabricated microfluidic channels. *Lab on a Chip*, 14(11):1826–1833, 2014.